1-1-2018

Ab-Initio and Molecular Dynamics Simulations Capturing the Thermodynamic, Kinetics, and Thermomechanical Behavior of Galvanized Low-Alloy Steel

Imran Aslam

Ab-initio and molecular dynamics simulations capturing the thermodynamic, kinetics, and thermomechanical behavior of galvanized low-alloy steel

By

Imran Aslam

A Dissertation
Submitted to the Faculty of
Mississippi State University
in Partial Fulfillment of the Requirements
for the Degree of Doctor of Philosophy
in Mechanical Engineering
in the Bagley College of Engineering

Mississippi State, Mississippi

December 2018

Ab-initio and molecular dynamics simulations capturing the thermodynamic, kinetics, and thermomechanical behavior of galvanized low-alloy steel

By

Imran Aslam

Approved:

_____

Mark F. Horstemeyer
(Major Professor)

_____

Hongjoo Rhee
(Co-Major Professor)

_____

Michael I. Baskes
(Committee Member)

_____

Bin Li
(Committee Member)

_____

Yucheng Liu
(Graduate Coordinator)

_____

Jason M. Keith
Dean
Bagley College of Engineering

Name: Imran Aslam

Date of Degree: December 14, 2018

Institution: Mississippi State University

Major Field: Mechanical Engineering

Major Professor: Mark F. Horstemeyer

Title of Study: Ab-initio and molecular dynamics simulations capturing the thermodynamic, kinetics, and thermomechanical behavior of galvanized low-alloy steel

Pages in Study 133

Candidate for Degree of Doctor of Philosophy

A seven-element Modified Embedded Atom Method (MEAM) potential comprising Fe, Mn, Si, C, Al, Zn, and O is developed by employing a hierarchical multiscale modeling paradigm to simulate low-alloy steels, inhibition layer, and galvanized coatings. Experimental information alongside first-principles calculations based on Density Functional Theory served as calibration data to upscale and develop the MEAM potential. For calibrating the single element potentials, the cohesive energy, lattice parameters, elastic constants, and vacancy and interstitial formation energies are used as target data. The heat of formation and elastic constants of binary compounds along with substitutional and interstitial formation energies serve as binary potential calibration data, while substitutional and interstitial pair binding energies aid in developing the ternary potential. Molecular dynamics simulations employing the developed potentials predict the thermal expansion coefficient, heat capacity, self-diffusion coefficients, thermomechanical stress-strain behavior, and solid-solution strengthening mechanisms for steel alloys comparable to those reported in the literature.

Interfacial energies between the steel substrate and inhibition layer shed light on the interfacial nanostructures observed in the galvanizing process.

DEDICATION

First and foremost, I dedicate this work (in memoriam) to my dad, Muhammad Aslam. As a 16-year-old graduating high-school, I expressed a desire to pursue a college degree in the United States, and my Dad was the first one to support me, both emotionally and financially. Because of him, I was able to pursue my dream of obtaining a bachelor's degree that ultimately paved way for me to receive a doctorate.

Second, to my mom, who has played a central and vital role while I was pursuing my Ph.D. by providing me an incredible amount of support. For the past three years, I did not get an opportunity to visit my mom back home and even though we dearly and painfully missed each other, she would always tell me to focus on my studies instead of worrying about her and ensure I graduated with the highest honors. That, for me, was the greatest sacrifice any parent can make, and I am and will always be immensely grateful to her for the monumental patience she exhibited.

Third, to my parents-in-law, who supported me throughout the Ph.D. journey. They always made me feel comfortable and instilled positivity at some of the most critical moments of my life. Thank you for your patience and unwavering faith in me.

Lastly, I would dedicate this work to my wife, Mahnoor. She is the rock in my life and provided me an unyielding support throughout my Ph.D. I cannot thank her enough for being with me through thick and thin during these past years. She always knew how to calm and relax me whenever I would feel stressed, which is the primary reason that I

came out with my sanity intact. I also acknowledge that this time and process was at least as hard and tough on her as it was on me, and I appreciate all her sacrifices. She truly is my better half and continuously helps me grow as a better man and husband every day.

ACKNOWLEDGEMENTS

I would like to begin by thanking all the professors who have taught me during my graduate degree. A special thanks to Dr. Judy Schneider who bestowed a wealth of knowledge related to material science and engineering that ultimately became the bedrock and epicenter of my dissertation.

To Dr. Bin Li and Dr. Hongjoo Rhee, my committee members, who provided me the opportunity and funding to start as a graduate research assistant at CAVS. Thank you so much for guiding me throughout the Ph.D. process and helping me evolve as a graduate student.

To Dr. Mike Baskes, my committee member and mentor, who has been the most instrumental for my graduate research. Thank you for being overwhelmingly patient and providing an in-depth knowledge of the subject matter. It is truly my life's honor to have been under your tutelage.

To Dr. Mark Horstemeyer, my advisor, mentor, and most importantly, a father-figure. You have helped me and my wife at the most critical moments of my life, and I will be forever thankful and grateful to you. You are a source of inspiration for me and someone I will try to model myself after for the rest of my life. I can only hope to reach up to your potential but, more importantly, attain the potential you have envisioned for me. Thank you for granting me with incredible wisdom, knowledge, and skillset to succeed in the real world.

I would also like to recognize and thank Dr. Doyl Dickel for helping me out throughout the dissertation research. He exhibited tremendous amount of patience and always welcomed me with an open-door policy. In addition, sincere thanks to Dr. Sungkwang Mun also helped improve the theoretical understanding during my research.

To Stephen Horstemeyer, Melissa Mott, and Robert Malley, thank you for mentoring and supporting me throughout my undergraduate and graduate career. It was because of the passion instilled in me for metallurgy that I decided to pursue a degree in mechanical engineering and materials science.

To Rose Mary Dill, who has been a mom to not just me, but all the graduate students at CAVS. Words cannot express how much she prioritizes and works for everyone, and we cannot thank her enough for it.

To my fellow graduate students, friends, and colleagues, I cherish each and every interaction I have had with everyone, and I would like to acknowledge that my work is a culmination of hard work and contribution from everyone. To Dr. Shane Brauer, the time we spent as Ph.D. students at CAVS is among my most treasured memories. Thank you so much for being my best friend and for always being there for me. To Karen Persons, our end of the day chats recapping the day's work served as a vent that helped me reset. Thank you for being such a great friend. To Shiraz Mujahid, you have been more than a brother to me and have been there for me through all the highs and lows. Thank you for lending me your intellectual support through our many conversations. To Dr. Muhammad Nadeem, thank you for the selfless sacrifices and care you showed to me. You are truly an inspiration for me.

TABLE OF CONTENTS

APPENDIX

LIST OF TABLES

LIST OF FIGURES

CHAPTER I

INTRODUCTION

1.1 Motivation

Galvanized steel is extensively used in the automotive industry, the largest business market in the world, and the initiative to reduce vehicular weight comes at a cost of reducing steel sheet thickness. The steel industry is developing the third generation (3G) of advanced high strength steels (AHSSs) which are vitally important for better fuel efficiency and is directly associated with the weight of vehicles. Weight reduction can be achieved by employing steel components with improved strength and good ductility [1,2]. New generation AHSSs contain higher concentration of alloying elements, for example, silicon (Si) and manganese (Mn) to increase AHSS's strength. However, the addition of Si and Mn in the steel introduces oxides that reduce corrosion resistance [3]. One of the primary concerns for continuous galvanizing lines (CGLs) is the selective oxidation of Si and Mn on steel surfaces during annealing prior to zinc dipping. Oxidation may occur both at the external surface and internal subsurface depending upon partial pressure of oxygen in the annealing furnace [4–7]. How these oxides affect galvanizing of AHSSs has been the subject of extensive discussions [4–11]. By electronics principle and atomistic modeling, coupled with nanoscale materials characterization, we will determine the thermodynamics, kinetics, and thermomechanical

behavior for steel, along with atomistically model the interfacial features of selective oxides and inhibition layer formation during galvanization.

1.2 Multiscale Experiments

The properties observed at the structural length scale are governed by phenomenon occurring at the lower length scales. Therefore, exploring the lower length scale is a necessity to fully comprehend the structure-property relationships of a material, as depicted in Figure 1.1. As such, understanding the physics behind any unknown phenomenon requires exploratory experiments to be conducted. Using these experiments, we not only investigate the phenomenon but acquire pertinent information that can serve as a blueprint to setup a computational, physics-based model. Once the model has been developed, calibration experiments are conducted where we tune our model to realistic results. Once we are confident about the model calibration, we can make predictions and experimentally validate our model.

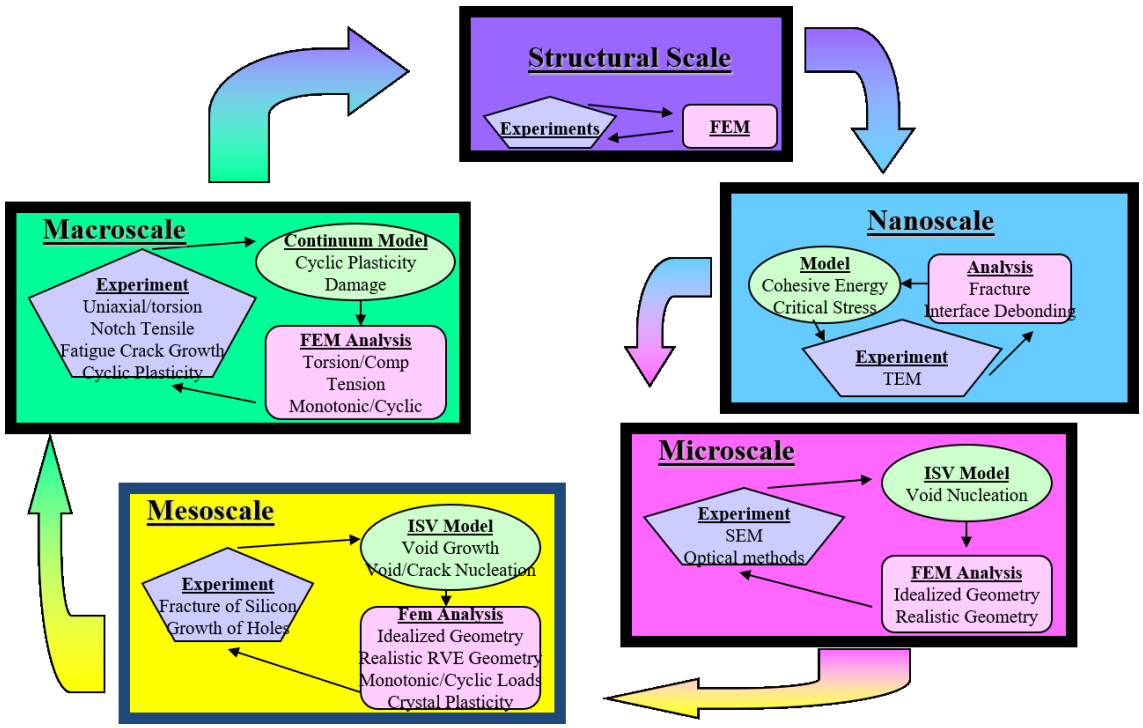

Figure 1.1 Multiscale experiment design concept employed to explore, calibrate, and validate physically observed phenomenon at each length scale.

Exploratory experiments are conducted to garner information on the nature of the phenomenon being captured. Calibration experiments are conducted to provide modeling data. Validation experiments are conducted to ensure the calibrated model can make a prediction.

1.3 Hierarchical Multiscale Modeling

Integrated Computational Materials Engineering (ICME) is a computational-based design paradigm that employs hierarchical multiscale modeling to capture continuum scale phenomenon. Therefore, ICME was invoked to study the meso to macro length scale phenomena and determine the structure-property relationships in galvanized steels. In particular, a 'vertical' ICME methodology was used, which provided a unique opportunity to ascertain the material behavior at different length scales.

The first step in employing ICME entails downscaling the engineering problem, followed by upscaling the pertinent information at each length scale to resolve the

engineering problem. Capturing the interfacial structures observed at the micro/meso-scale in galvanized steels serves as our downscaling driver, as illustrated in Figure 1.2. The interfacial structures can be modeled as a continuum using phase-field modeling, which requires thermodynamic and kinetics information as calibration inputs. In order to obtain the thermodynamic and kinetics information, we downscale to the atomistic length scale to garner interfacial energies and diffusion coefficients. However, accurate representation of atomistic behavior can only be acquired by a force-field that has been specifically calibrated to capture the nanoscale features of galvanized steels. The atomistic calibration data can be obtained by further downscaling to the quantum length scale.

Once the downscaling requirements are clarified, the upscaling parameters are setup to lay the foundation of a path to follow. At the lowest length scale, Density Functional Theory (DFT) will be employed to garner energy-volume curves, heat of formation, elastic constants, vacancy formation and dilute solution energies to upscale as calibration data for the atomistic potential. In addition, heat of formation and dilute solution energies will also be upscaled to the mesoscale phase-field model. The Modified Embedded Atom Method (MEAM) will be the force-field calibrated at the atomistic length scale using experimental and DFT data. Once the MEAM potential is fully calibrated, thermodynamic and kinetics data of interfacial energies, grain boundary energies, and diffusion coefficients will be evaluated and upscaled to the mesoscale phase-field model.

Employing the ICME methodology entailed in this section will ensure that the model developed is rooted in physics, rather than an empirical-based model. Therefore,

developing robust computational models can lead to a diminished dependence on experiments that are traditionally expensive to conduct. Consequently, this work will lead to designing new coatings for advanced high strength steels for automotive industry, and conversely, designing steel alloys that are compatible with standard Zn coatings.

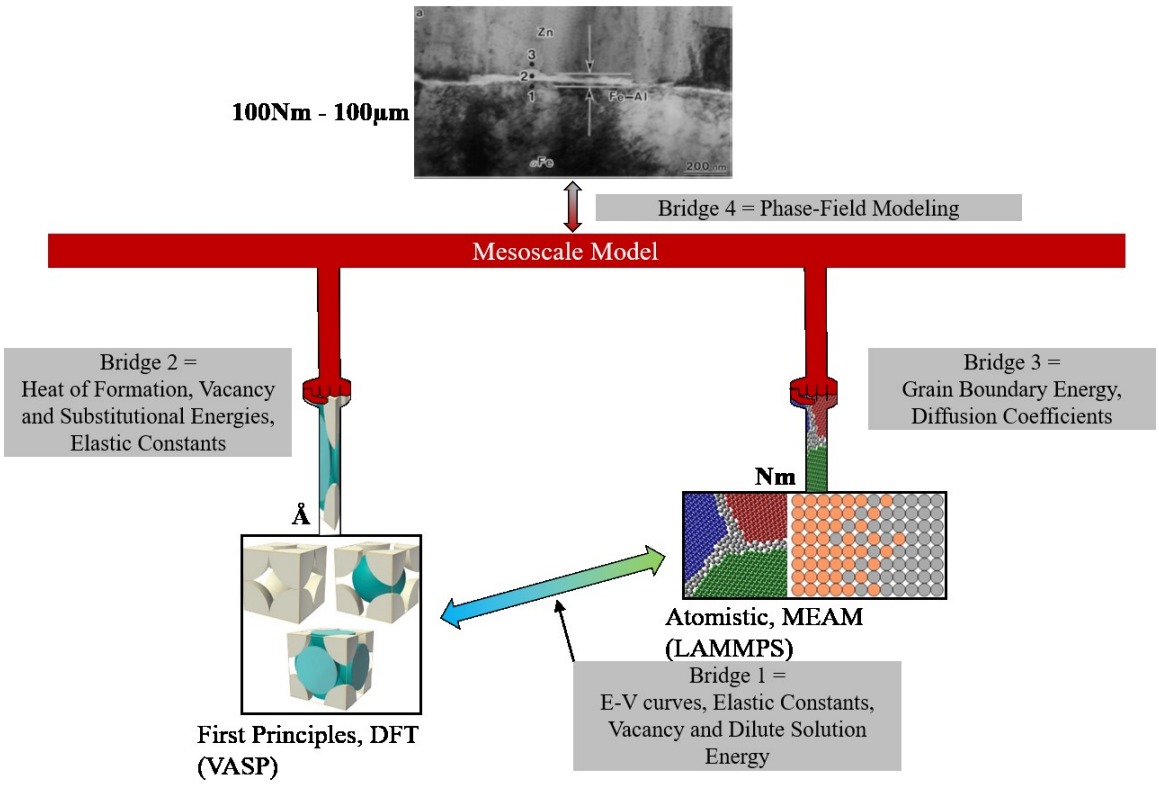

Figure 1.2 A hierarchical multiscale modeling schematic to design new coatings for advanced high-strength steels for automotive applications.

Calculations will be performed from the electronics scale using DFT to determine interatomic potentials. The information will be upscaled to the atomistics length scale where MEAM will be used to develop potentials for Fe-Mn-Si-Al-Zn-C-O system. The results will then be upscaled to the microscale where phase-field modeling will be used to capture oxidation and formation of intermetallics.

1.4 Dissertation Structure

Chapter I initiates the motivation behind the study conducted in this dissertation, along with defining the multiscale aspect of experiments, and providing a detailed understanding of ICME paradigm that has been invoked in the forthcoming modeling efforts. Chapter II details the exploratory experiments conducted to examine the interfacial structures at high resolution and delineate the modeling requirements. Chapter III presents the MEAM potential for Fe, Mn, Si, and C. The single element, binary, and ternary interactions of the four elements, along with validation testing was used to garner thermodynamics, kinetics, and thermomechanical data of low-alloy steels. Chapter IV develops a MEAM potential for Fe, Mn, Si, C, Al, Zn, and O to fully capture the elements involved in the interfacial structures observed in galvanized steels. Preliminary validation testing is conducted to ensure the applicability of the developed MEAM potentials. Chapter V discusses the sensitivity and uncertainty associated with calibrated properties of the iron – silicon binary pair. The methodology used to determine sensitivity and uncertainty is a one-factor-at-a-time perturbation method. Finally, Chapters VI and VII will conclude the dissertation with a summary of results in this study and recommendations for future works.

CHAPTER II

TRANSMISSION ELECTRON MICROSCOPE CHARACTERIZATION ON THE INTERFACIAL STRUCTURE OF GALVANIZED DUAL-PHASE STEEL[1]

2.1 Introduction

In continuous hot-dip galvanizing of automotive steels, a strip is submerged into a molten zinc (Zn) bath which contains a small amount of aluminum (Al) (<0.2% depending upon the nature of processing). Metallurgical reactions occur instantly at the solid-liquid interface. Because the affinity between iron (Fe) and Al is much higher than that between Zn and Fe, a thin layer of Fe-Al intermetallic (Fe_2Al_5 or $Fe_2Al_{5-x}Zn_x$) [13] is developed on the steel substrate surface. The thickness of this interface region falls in the range of ~100 nm [14]. The formation of the Fe-Al intermetallic delays or inhibits the formation of brittle Fe-Zn intermetallics and enables good adhesion between the Zn-coating and the steel [15].

The interest in improved fuel efficiency of vehicles has stimulated the development of the third generation (3G) of advanced high strength steels (AHSSs) which are vital for weight reduction. Mass reduction and the resultant better fuel efficiency can be achieved when the strength of steels is increased [1,2]. New generation

[1] Previously published by Imran *et al*. [12]

AHSSs contain higher concentration of alloying elements, for example, silicon (Si) and manganese (Mn) that are key players for higher strength. However, the addition of these alloying elements with higher concentrations poses a challenge to the galvanizability that is crucial for enhanced corrosion resistance of the AHSSs [3]. One of the primary concerns for continuous galvanizing lines (CGLs) is selective oxidation of Si and Mn on steel surfaces during annealing. The Si and Mn oxides are difficult to be reduced by hydrogen [8–11] and these oxides remain on the surfaces before hot dipping. Oxidation may occur both externally and internally depending upon the oxidizing potential inside the annealing furnace [4–7]. Thus, understanding the structure of the interface of galvanized high strength steels is crucially important. How these oxides affect galvanizing of AHSSs has been the subject of extensive discussions [4–11] most recently.

Due to the complexity and the fine scale of the metallurgical reactions at the interface, characterizing the interfacial structure with clarity is rather challenging. The interface of galvanized steels has been studied extensively and primarily by scanning electron microscopy (SEM), glow discharge optical emission spectroscopy (GDEOS) which allows characterization across the Fe-Zn interface by sputtering through its thickness [16], energy dispersive spectroscopy (EDS) or x-ray photoelectron spectroscopy (XPS) [6,17]. A number of transmission electron microscopy (TEM) studies have been conducted on the interface of galvanized steels only after focused ion beam (FIB) was available [14,18–26] since conventional TEM specimen preparation approaches are unable to locate the interface. These previous studies have shown very promising results in resolving the fine interface.

As part of the ongoing research on how processing parameters such as dew point affect oxidation and the subsequent coating processes of high strength steels, in this work, we employed TEM, high resolution TEM (HRTEM) and scanning TEM (STEM) and performed bright field (BF) and dark field (DF) imaging to characterize the interfacial structures of a galvanized dual phase (DP) steel. The results shed new insight on the galvanizing of high strength steels and the growth of the inhibition layer.

2.2 Experimental Method

The material used in this work is a galvanized dual phase (DP) steel supplied by POSCO. The chemical composition of such DP steel is shown in Table 1. The composition of Mn and Si are 1.75 wt% and 0.19 wt%, respectively. The steel strip was annealed at a well-controlled dew point. The peak annealing temperature before the Zn bath was 780 °C and the composition of the annealing gas was 95% N_2 and 5% H_2 with a dewpoint of −40 °C. The bath temperature of the Zn bath was 460 °C. The 1.0 mm thick steel strip was hot-dipped with a galvanizing bath with a dissolved Al concentration between 0.14 – 0.2% so that a full inhibition layer can be expected.

Table 2.1 Chemical composition of the DP steel

C	Mn	Si	Al	Nb	Cr	Ca
0.0971	1.7500	0.1923	0.0408	0.0164	0.3304	0.0008

To prepare TEM specimens, first, the galvanized specimen was mechanically polished on the cross-section through the thickness. The polishing was carefully performed to minimize the mechanical damage to the interface region between the steel

substrate and the coating. After polishing, the Zn coating was well revealed. Afterwards, focus ion beam was used on a TESCAN Lyra to fabricate specimens for TEM analysis. A thin slice approximately 1.0 μm thick was first fabricated by digging trenches around the slice (Figure 1a). During milling, EDS mapping was performed on the slice to ensure that the slice contains both the substrate and the coating. Before the FIB fabrication, a 1.0 μm thin layer of platinum was deposited on the area of interest such that the area of interest was protected from rapid sputtering and gallium implantation by the ion beam. The regions adjacent to the area of interest were sputtered away (Figures 1a and 1b). Once these trenches were created, the specimen was severed off from the bottom such that the specimen was only connected with the bulk at one side, i.e., the specimen was a dangling cantilever. A tungsten needle was then carefully inserted to make a gentle contact with the thin specimen. Then platinum was deposited to weld the needle to the specimen. This was followed by severing the last connection between the thin specimen and the steel substrate. The thin slice was then transferred and welded onto the top of a TEM copper grid via platinum deposition on the points of contact, as illustrated in Figure 1c. The tungsten needle was then cut off from the specimen and retracted. A final thinning of the specimen was performed to reduce the thickness to the level of electron transparency. A FEI TECNAI F-20 transmission electron microscope (TEM), with an operating voltage of 200 keV, was used to examine the sample at higher resolution. The final specimen was also characterized for elemental mapping using a JEOL 7000 FE scanning electron microscope (SEM) in STEM mode. The SEM-STEM scanning yields higher X-Ray intensities, enabling shorter scanning times and large scanned areas.

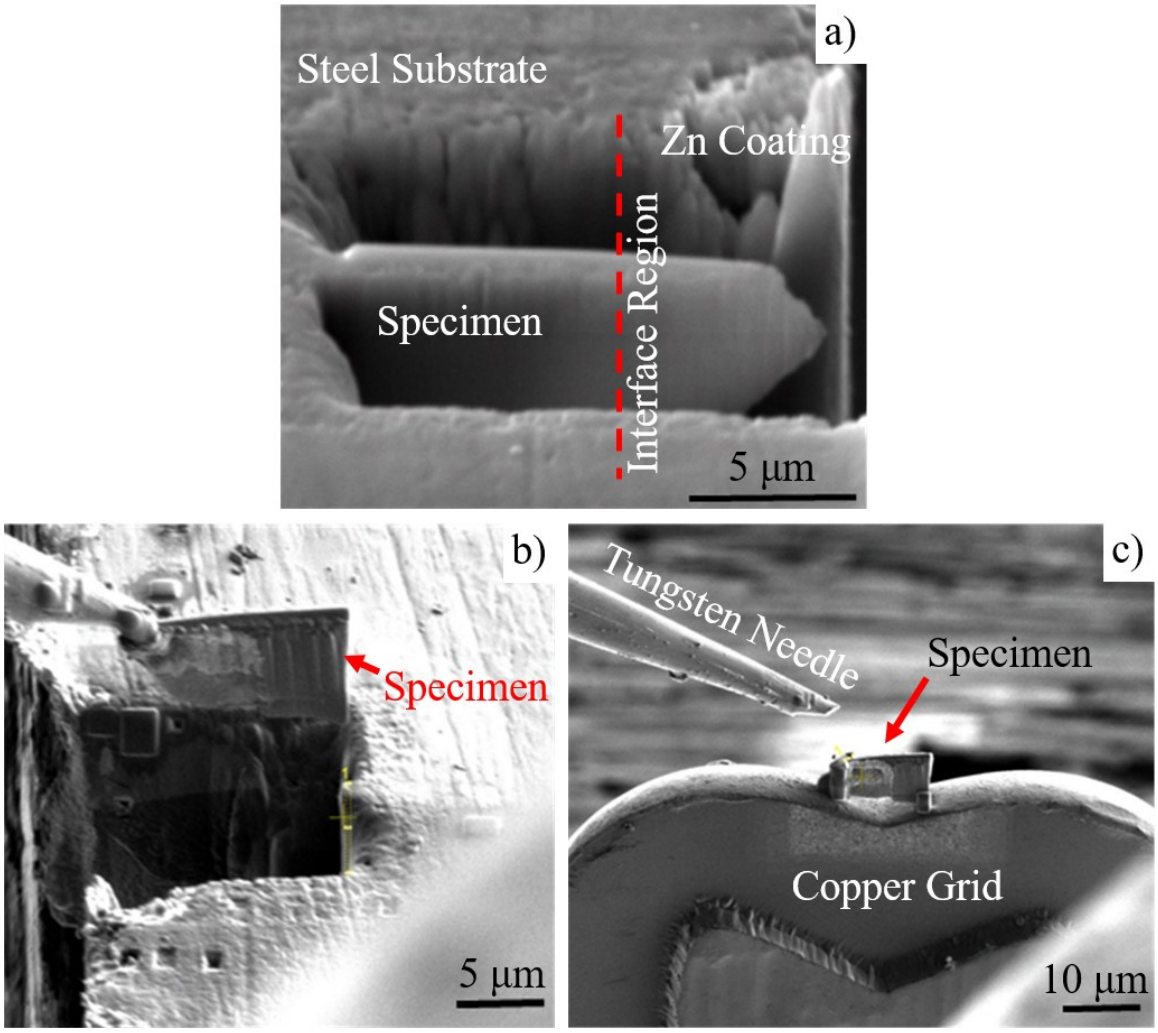

Figure 2.1 Fabrication of a galvanized dual-phase sample using focused ion beam (FIB).

a) Digging trenches around the specimen. During sputtering, EDS was performed to ensure that the interface region (indicated by the dashed line) was contained in the specimen. b) Lift-out of a 1µm thin specimen by welding it to the tip of a tungsten needle. c) Cold welding the thin specimen to a copper grid by depositing platinum.

2.3 Results

The results from the SEM-STEM mapping are presented in Figure 2. A rectangular area that contains the Zn coating, interfacial layer, and the substrate was scanned (Figure 2a). In the mapped area, Zn is shown in blue and iron in red. In between,

an Al-rich region can be observed, which is shown in green. The color codes of individual elements were superimposed in Figure 2a to show the structure of the interface at a relatively low magnification. The Al-rich layer, commonly referred to as the inhibition layer, has a stoichiometry of Fe_2Al_5 or $Fe_2Al_{5-x}Zn_x$ when some Al atoms are replaced by Zn. The inhibition layer appears to be continuous in nature over the interface. Another elemental mapping was performed in a thin section that encompasses the interface region to determine the distribution of alloying elements, e.g. Mn and Si. Figure 2b shows the distribution of Mn near the interface. A bright line along the interface can be resolved, indicating that the intensity of Mn is much higher at the interface than in other regions. Figure 2c shows the distribution of Si near the interface. In contrast to Mn, no observable intensity peak of Si can be seen.

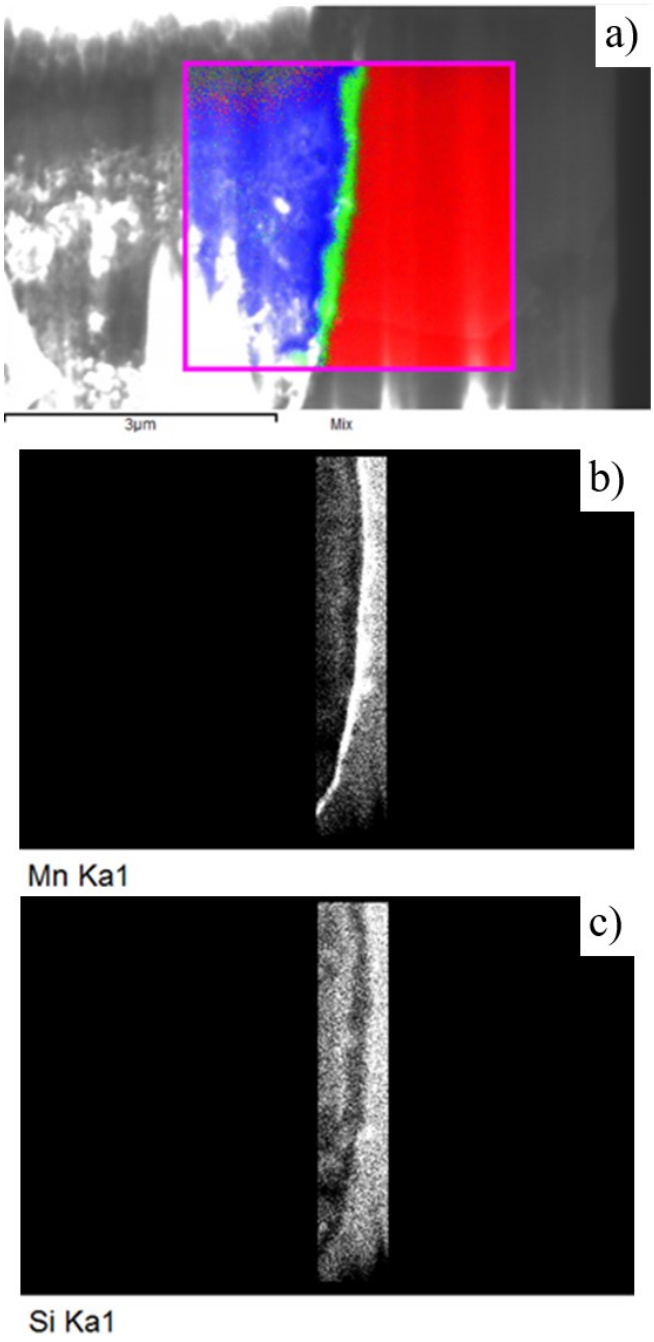

Figure 2.2 SEM EDS (Energy Dispersive Spectroscopy) elemental map across the interface of the Dual-Phase Galvanized steel.

a) Red corresponds to iron, blue to zinc and green to aluminum. b) A segregation of manganese can be found at the surface of the steel substrate. c) No segregation of silicon was found at the steel surface.

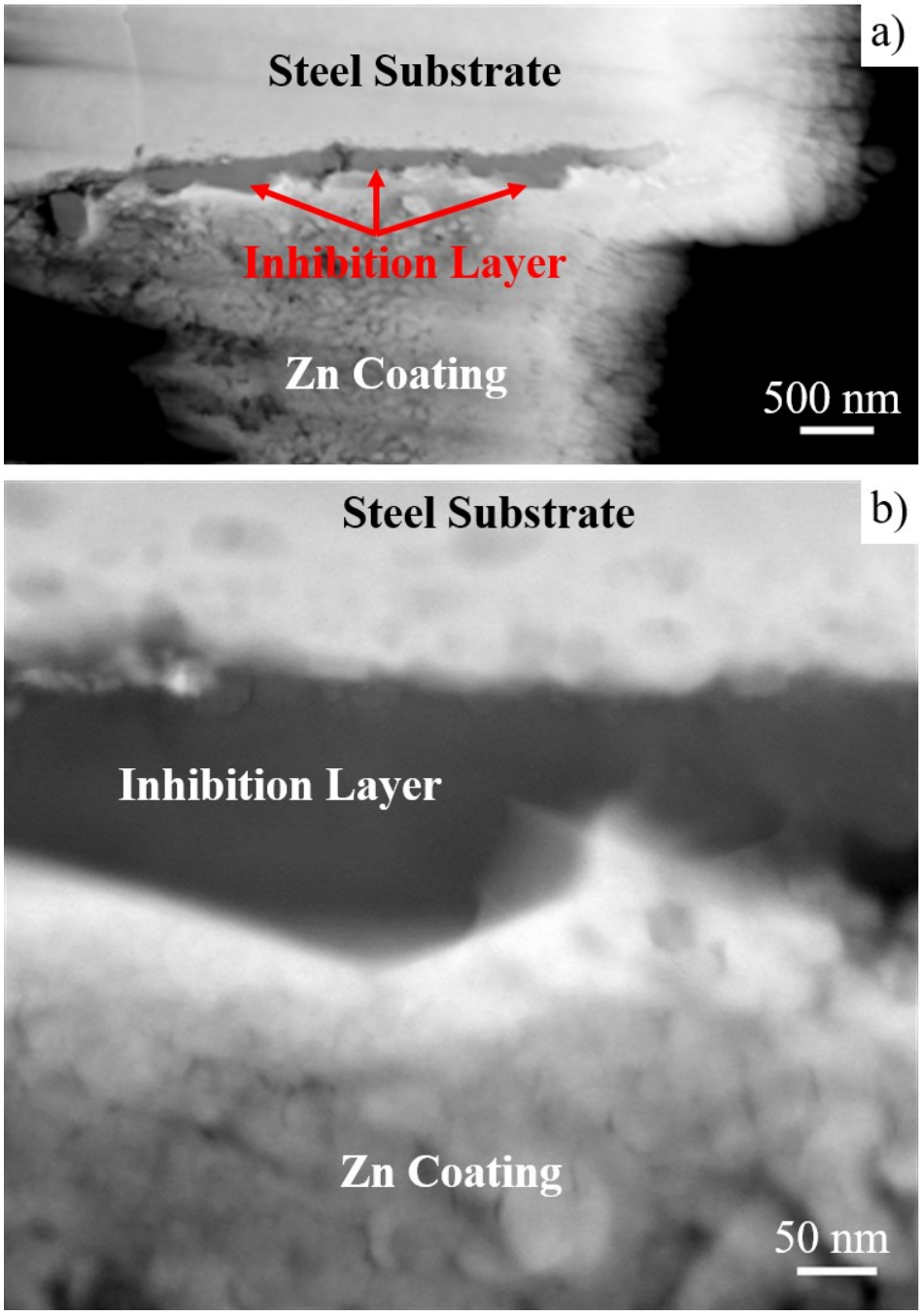

Figure 2.3 The inhibition layer is captured in TEM using STEM mode with a High Angle Annular Dark Field (HAADF) detector.

a) A low magnification image that encompasses the entire inhibition layer present in the fabricated specimen. b) A higher resolution image detailing the morphology of the inhibition layer, present in between the steel substrate and the zinc coating. The inhibition layer is approximately 93 nm in thickness.

The specimen was then examined under TEM at higher magnifications and resolution. High angle annular dark field (HAADF) imaging was performed at STEM mode to achieve better image contrast from the compositional difference of the phases (Figure 3a). In between the zinc coating and the steel substrate is the interface region which comprises the continuous inhibition layer (the dark region indicated by the arrows). Figure 3b shows the image of the inhibition layer at a higher magnification. The thickness of the inhibition layer was measured at ten different locations by averaging the variation in the gray scale of the image. The average thickness of the inhibition layer is about 93±26 nm.

In the sub-surface region of the steel substrate adjacent to the inhibition layer, fine particles with sizes about a few tens of nanometers can be observed (Figure 4a). These particles are internal oxides. The internal oxide particles are distributed in a region about 150 nm below the surface. The internal oxides were observed previously in high strength steels [4–8]. At a higher magnification, right between the inhibition layer and the surface of the steel substrate is another thin layer, which is evident by the different contrast, as shown in Figure 4b (indicated by the pairs of arrows). This thin layer is the external oxide layer. In the HAADF imaging, the external oxides layer appears to be continuous in nature. This is consistent with the EDS mapping shown in Figure 2b.

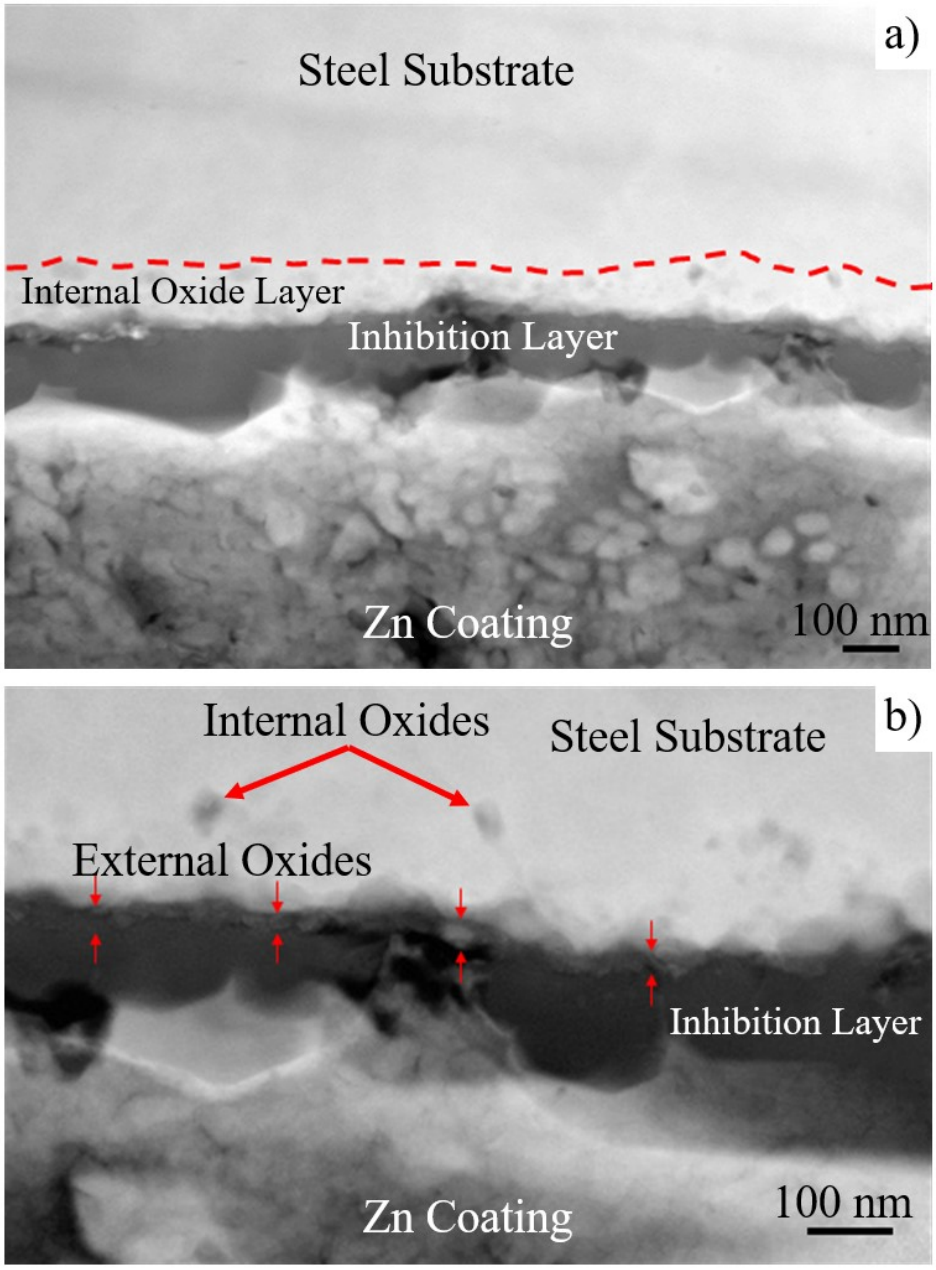

Figure 2.4 TEM images in Scanning TEM (STEM) mode.

a) Internal oxides, indicated by the region in between the red dashed line and the external oxide layer, are present at the subsurface of the steel substrate. b) External oxides, pointed out by the red arrow markers, are present in between the steel substrate and the inhibition layer.

The phases that are present at the interface region and the structure of the interface in the galvanized DP steel are schematically summarized in Figure 5.

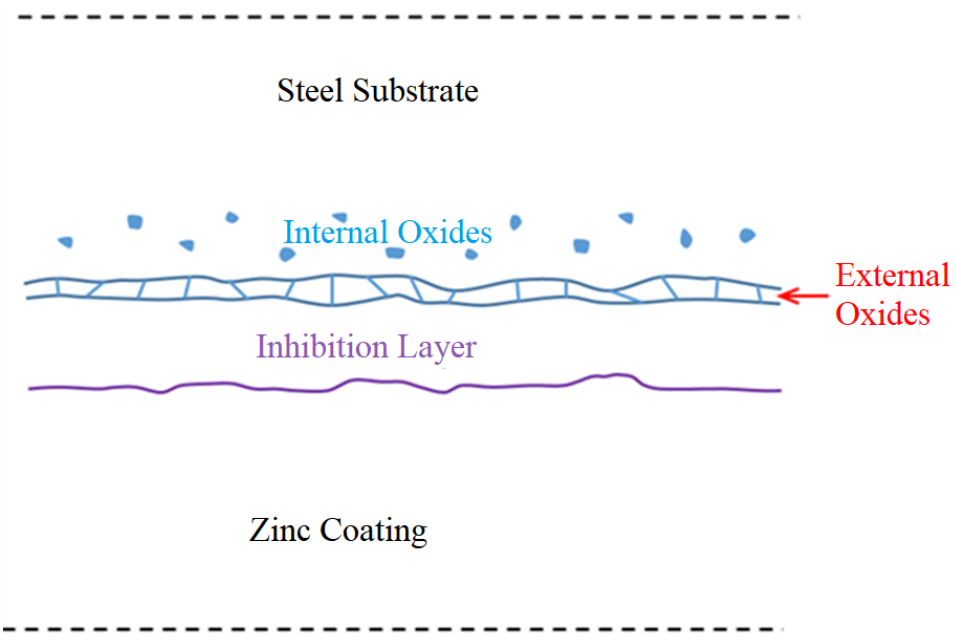

Figure 2.5 A schematic of the phases and the structure of the interfacial region of the galvanized DP steel.

To determine the chemical composition of this thin layer, an EDS line scan was performed starting from the zinc coating to the steel substrate. Figure 6 shows the result of the scan. The intensity of Zn is high at the start but it begins to decrease as the scan progresses into the inhibition layer, whereas the intensity of Al and Fe increases and levels out inside the inhibition layer. A certain amount of Zn was detected in the inhibition layer as well. This could be an indication of solid solution of Zn in Fe_2Al_5, or the detection of Zn in the coating due to the large excitation volume of the nano electron beam. Notably, following the sharp decrease of both Al and Fe as the scanning

approaches the substrate, an increase in Mn and O is registered between the inhibition layer and the substrate. Clearly, the presence of the intensity peaks of Mn and O indicates that Mn oxides was formed on the surface of the substrate during processing. Using the similar measuring technique, the thickness of the Mn oxides layer was determined to be about 20±6 nm.

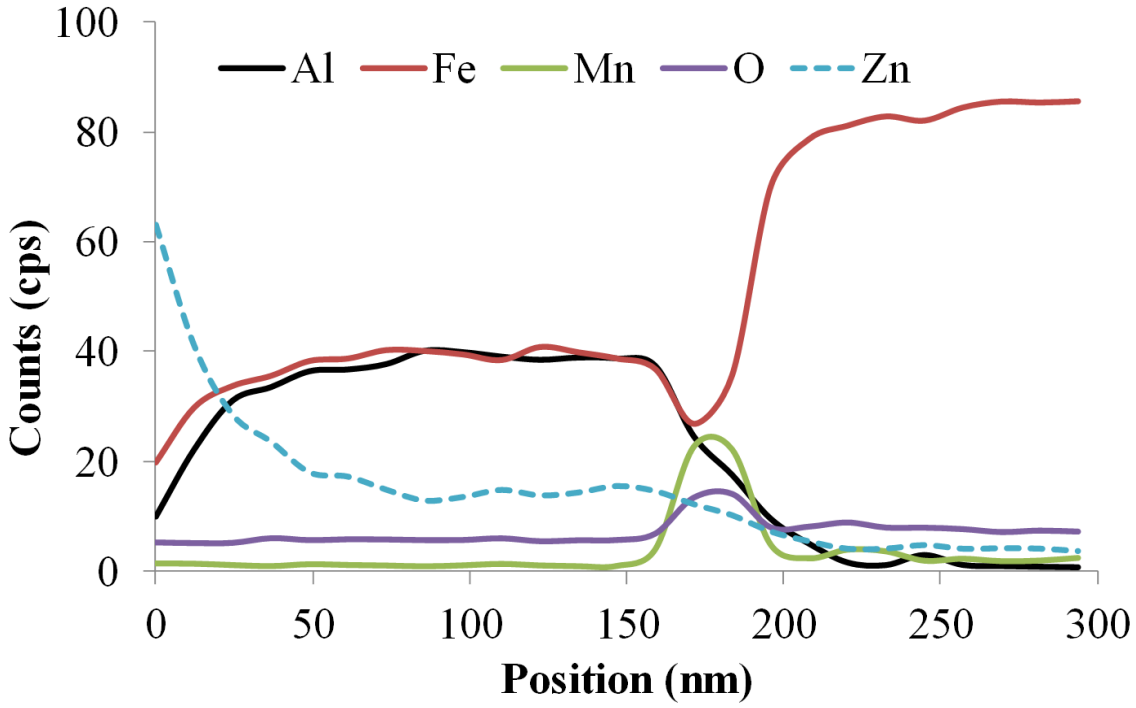

Figure 2.6 EDS Line Scan result across the interface of Dual-Phase Galvanized Steel in STEM mode.

Scan starts at the zinc coating and ends at the steel substrate region. The intensity for iron and aluminum stay constant across the inhibition layer. A spike in manganese and oxygen is observed as the inhibition layer ends, as evident by a drop in the intensity of aluminum.

To further resolve the structure of the interface, bright field imaging was also performed. Figure 7a shows both the internal oxide particles and the continuous external

oxide film on the surface of the steel substrate. At a higher magnification (Figure 7b), grain boundaries can be observed inside the inhibition layer. These grains (or sub-grains) have an average grain size of approximately 5-10 nm. HRTEM was also performed and the lattice fringes observed are shown figure 7c. Clearly, grain boundaries or sub-grain boundaries can be seen and the lattice fringes present different orientations.

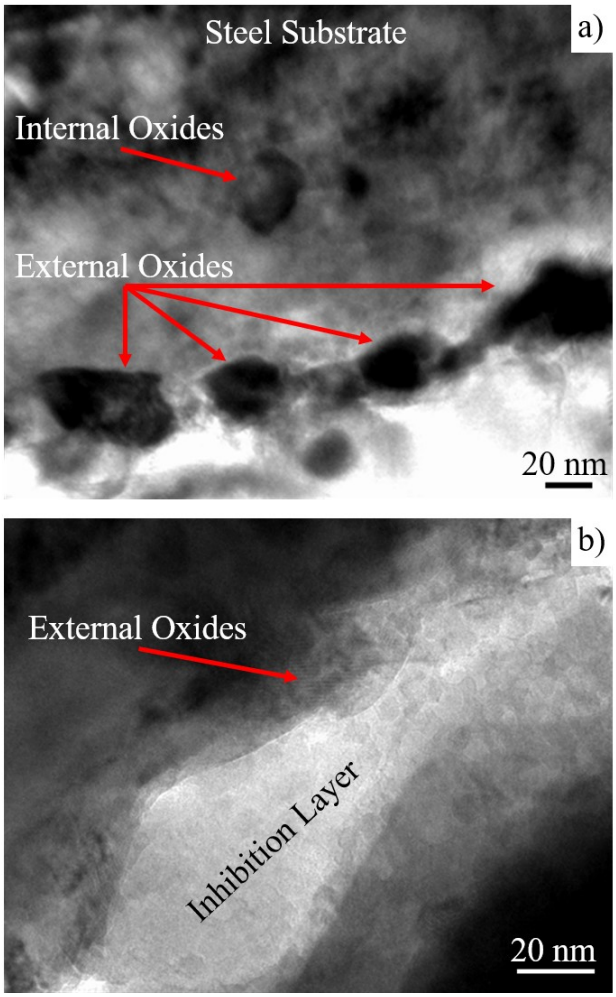

Figure 2.7 High resolution bright field (BF) TEM images of the interface between internal oxides, external oxides, and the inhibition layer.

a) An interface illustrating the external and internal oxides. The external oxides are interconnected. b) An interface of the inhibition layer and the external oxides. The inhibition layer comprises nanocrystalline grains.

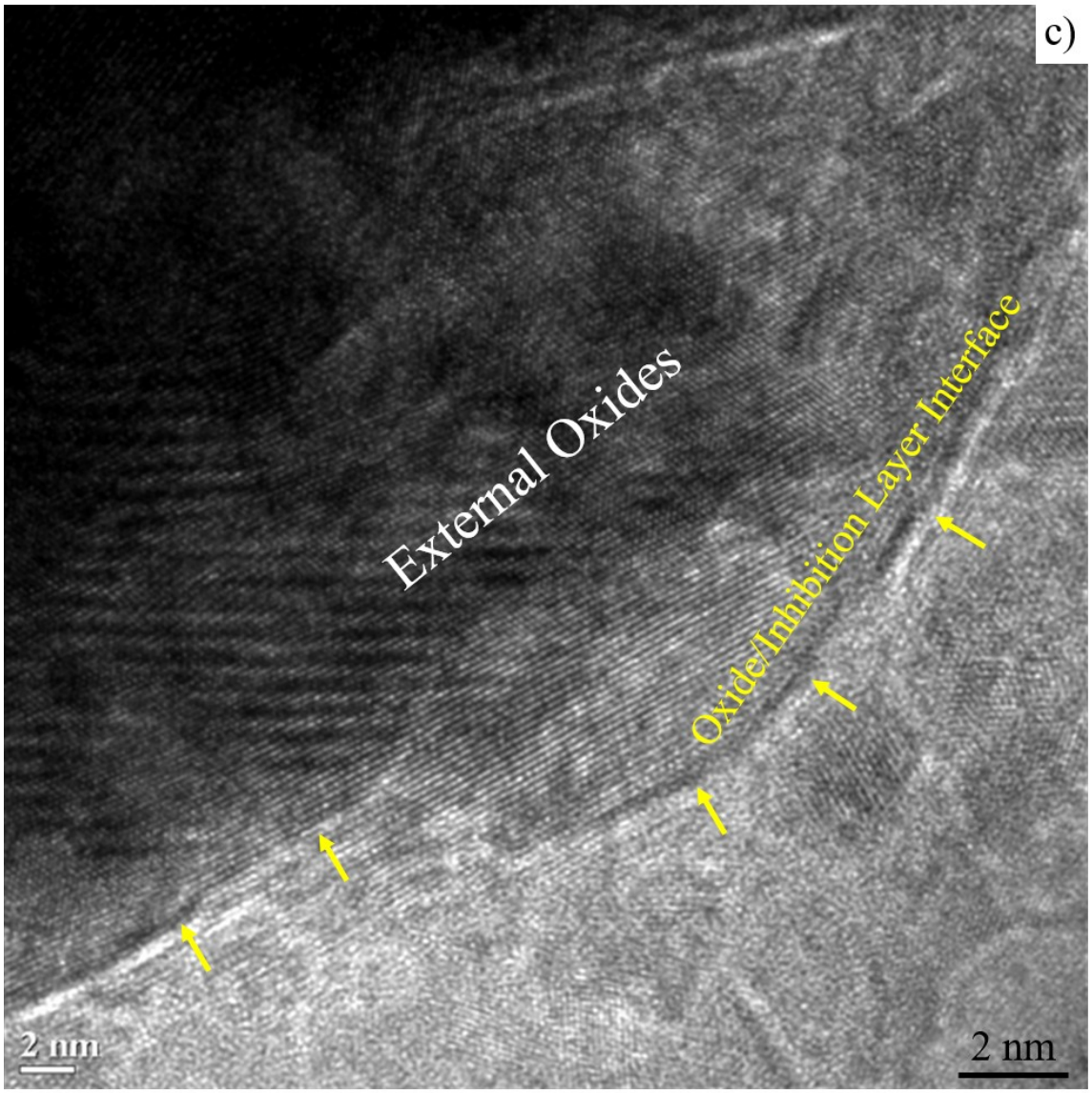

Figure 2.7 (continued)

c) A high resolution Bright Field (BF) TEM image illustrating the nanocrystalline inhibition layer, external oxides and the oxide/inhibition layer boundary. The inhibition layer contains multiple lattice fringes at different orientation that represents a nanocrystalline structure. The interface between the oxides and inhibition layer is pointed out by the arrows.

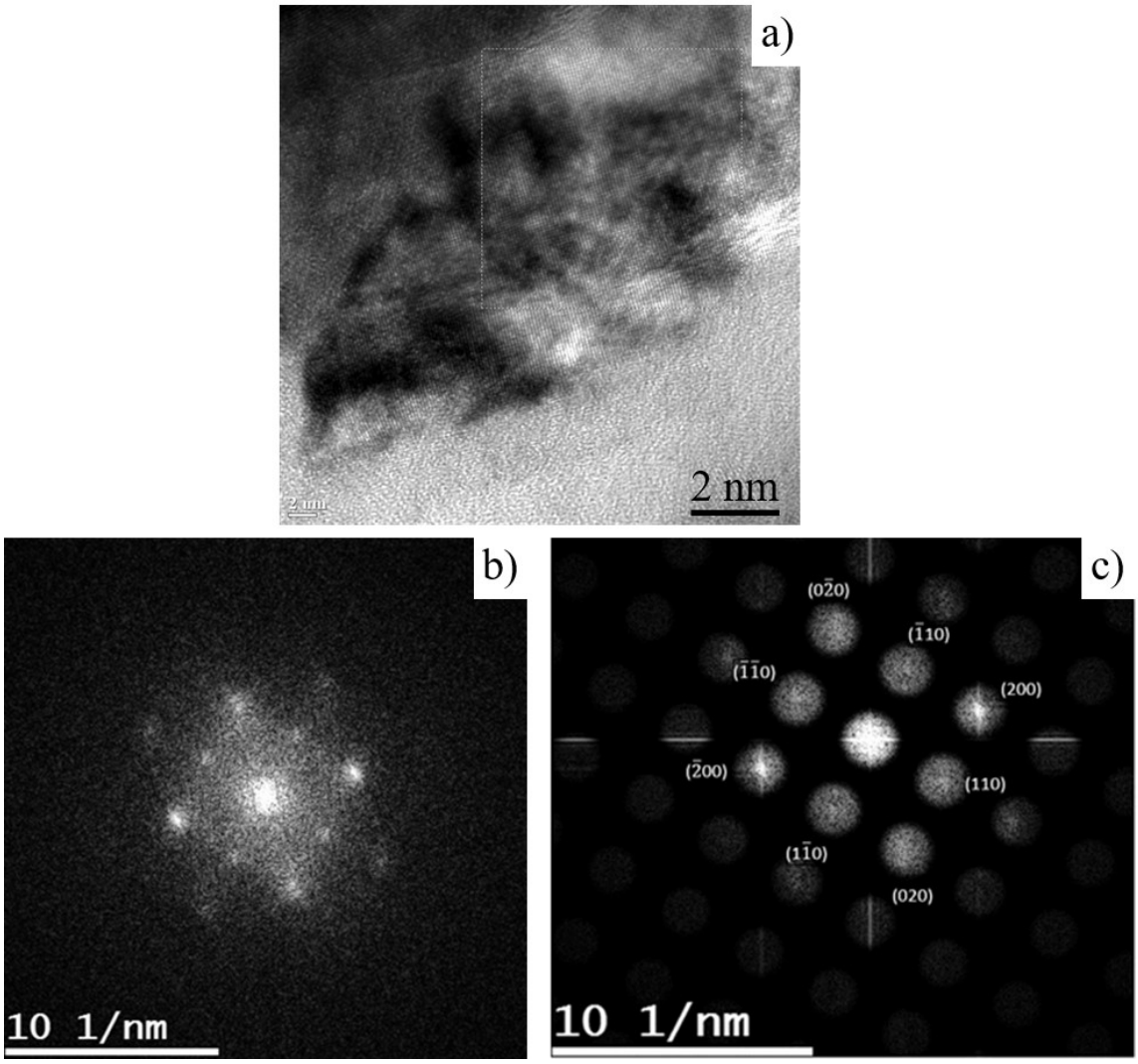

Figure 2.8 a) A high resolution TEM image; b) A diffraction pattern obtained by using FFT; c) An indexed diffraction pattern for manganese (II) oxides.

a) A high resolution TEM image which includes a manganese oxide particle present adjacent to the $Fe_2Al_5Zn_x$ inhibition layer. A square box is drawn on the oxide which contains lattice fringes to create a diffraction pattern using Fast Fourier Transform (FFT) algorithm b) A diffraction pattern obtained by using FFT of the manganese oxide region. Due to poor clarity of spots, further processing was performed. c) An indexed diffraction pattern providing evidence of manganese (II) oxides present at the surface of the steel substrate as external oxides.

Furthermore, the external manganese oxide is also crystalline as seen from the lattice fringes across the oxides. In order to determine the structure of the manganese oxide, diffraction patterns were obtained and indexed. A high resolution image is selected such that the lattice fringes across the manganese oxide layer are clearly visible, as illustrated in Figure 8a. A square box is drawn over our region of interest to create a diffraction pattern using Fast Fourier Transform (FFT) algorithm. The diffraction pattern obtained from FFT is shown in Figure 8b. The diffraction pattern was further processed in Digital Micrograph. The processed image, displayed in Figure 8c, is then indexed to reveal that the oxide is indeed manganese (II) oxide, which has a cubic structure. Similar observations were reported by Gong *et al*. [27,28]. In transformation induced plasticity (TRIP) steels, oxides at the surface of the substrate were reported to be rich in MnO and crystalline in nature.

2.4 Discussion

Our TEM work clearly revealed an almost continuous external MnO oxide film (~20 nm thick) on the surface of the DP steel, a layer of internal MnO oxide particles located about 100 nm below the surface, and a fully developed inhibition layer right on top of the external oxide film. The transition from external to internal oxidation is dependent upon the dew point which is a function of the partial pressure of water vapor in the H_2+N_2 mixture, i.e. the annealing atmosphere. Increase in dew point results in an increased diffusion of oxygen into steel, causing the formation of internal oxides [6,7]. On the other hand, lower hydrogen content in the annealing atmosphere leads to a higher oxidation potential due to an increase in pH_2O/pH_2 (i.e. partial pressure of water vapor to

partial pressure of hydrogen) ratio, thus yielding a transition of oxidation from external to internal [8,9].

Although the presence of oxides on the steel surface could be detrimental to reactive wetting [13,29,30], the TEM micrographs (Figures 3,4, and 6) indicate that a fully developed inhibition layer can still grow on the oxide film. Prabhudev *et al*. [4] reported that nano-islands of oxides present on the surface of the steel do not hinder the formation of the inhibition layer due to the ability of Fe-Al interface layer to grow over the oxides. Parazanovic and Spiegel [11] suggested that, oxides nucleate and grow as islands, instead of continuous layers, and do not deplete away completely in the reducing annealing atmosphere. If the oxides nucleate as nano-islands on the substrate grains that have different orientations, it is conceivable that the crystalline oxide grains will have different orientations as well. Hence, when the oxide grains grow and meet, grain boundaries or sub-grain boundaries will be produced. These grain boundaries act as short-circuit paths for Fe to diffuse through the oxide film. Also, Mn oxides such as MnO and Mn_2SiO_4 have been reported to be porous and have globular morphology [16,18] and this nature may not significantly degrade the wettability of Zn. However, the phenomenon of overgrowth of the inhibition layer over the oxide islands results in slowing down the reaction process. The study by Frenznick *et al*. [31] reported that at same coverage of oxides over the substrate, the smaller oxide islands had less detrimental effect to the reaction kinetics than the larger oxide islands. This is because the inhibition layer grows over the smaller islands faster than the larger ones.

Another possibility is that the seemingly continuous oxide film is actually discontinuous, as suggested by Sagl *et al*. [32]. As a result, surface areas free of oxides

may be in direct contact with the liquid Zn, leading to the localized nucleation of the inhibition layer in these areas. The inhibition layer continue to grow over the oxide film. This seems against the TEM observations in this work. The growth of the inhibition layer appears to be rather uniform and local penetration of the inhibition layer through the oxide-free areas were hardly observed.

Aluminothermic reduction of Mn oxides by Al, proposed by Khondker *et al*. [8], is considered as the major reason for the formation of well-developed inhibition layer ($Fe_2Al_{5-x}Zn_x$) over MnO film [8,11,13,32]. Aluminothermic reduction helps the formation of inhibition layer. The Al in Zn bath attacks the oxides and dissolves some of the Mn into the zinc bath. The reduction of Mn oxides expose a larger surface area for Al to react with Fe [16,32,33]. Then the Fe in the substrate diffuses outwardly to come into reaction with the Al. A favorable location for the outwards diffusion of Fe could be the regions where the external oxide grains meet, i.e. grain boundaries of the oxide film.

2.5 Conclusions

FIB was used to prepare site-specific TEM specimens that contains the interface between the steel substrate and the Zn coating of a galvanized DP steel. TEM, STEM, and HRTEM were performed to characterize the interfacial structure. The morphology of the oxides and the inhibition layer were very well resolved. The following conclusions can be reached:

1. External MnO oxide film was captured on the surface of the steel substrate. The oxide film appears to be continuous, and has a thickness about 20 nm. Internal oxide particles were observed as well, and the particles are about few tens of nanometers and are located in a sub-surface layer about 100 nm thick. However, no Si oxides were observed in this region. HRTEM results shows that the oxide grains are crystalline.

2. The Fe_2Al_5 or $Fe_2Al_{5-x}Zn_x$ inhibition layer was observed right on top of the external oxide film. The inhibition layer appears to be continuous in nature. Sub-structures inside the inhibition layer were resolved by HRTEM, which shows that grain boundaries or sub-grain boundaries were present.

3. The fully developed inhibition layer, despite the presence of a continuous Mn oxide film on the surface of the steel substrate, may be attributed to diffusion of Fe through the porous MnO film, the short-circuit diffusion paths between the oxide grains, or the aluminothermic reduction of Mn oxides.

2.6 Acknowledgments

IA, BL, and HJR gratefully thank the support from the International Zinc Association under the contract ZCO-64, Center for Advanced Vehicular Systems, Mississippi State University, U.S. National Science Foundation under the grants (#1506944 and #1506878) and Central Analytical Facility at University of Alabama. The authors also thank POSCO for supplying steel specimens for this research.

CHAPTER III

THERMODYNAMICS, KINETICS, AND THERMO-MECHANICAL BEHAVIOR OF LOW-ALLOY STEELS: AN ATOMIC LEVEL STUDY USING AN FE-MN-SI-C MODIFIED EMBEDDED ATOM METHOD (MEAM) POTENTIAL

3.1 Introduction

The desire for increased fuel efficiency and reduced emissions without sacrificing safety is as much of a concern with automotive industries as it ever has been [34–36]. One of the approaches to achieving these goals is to improve the strengths of materials while reducing their weight, especially in steel alloys, so that lightweighting could be attained. Despite desirable material characteristics, high strength steels have limited fabrication capability due to deformation resistance that causes tooling wear [37]. Therefore, the challenge lies to perform compositional design of high strength alloys in a manner that decreases the weight, retains workability, but generates the required strength after fabrication [38]. Recently, the concept of third generation high strength steels, also known as 3G advanced high strength steels or 3G AHSSs, has attracted a lot of attention [39–42]. The 3G AHSSs possess greater strengths than the first generation high strength steels, but avoid the high costs of second generation high strength steels [43]. Thus, superior properties combined with affordability in the automotive industry has been the primary consideration of developing 3G AHSSs. One of the promising strategies to

design and make 3G AHSSs is a quenching and partitioning method [44] in which austenite is stabilized through diffusion of carbon from supersaturated martensite to austenite, and thus formation of brittle carbides is suppressed.

To facilitate the development of 3G AHSSs, multiscale hierarchical simulation and modeling has been used to investigate the processing-microstructure-property relationship of these materials [45], which is critical to enable progress in the design of new AHSSs. One of the key challenges in multiscale modeling is to bridge individual length scales through proper transfer of information between electronic, atomistic, microscale, mesoscale, and macroscales. Most AHSSs are multicomponent systems. It is necessary then to develop interatomic potentials that allow experimentally-tethered computer simulations to capture the time-scale and length-scale physics of 3GAHSS such that the lower length-scale mechanisms can be better understood and their influence in higher length scale models can be incorporated to design fast, inexpensive processing routes resulting in the desired microstructure [46].

Atomistic simulations at the lower length scales can bridge the gap in comprehending and quantifying the structure-property relationships. Accurate representation of atoms at the lower length scales can be provided by first-principle calculations but at the cost of either large simulation times or requiring extensive computational resources. In order to conduct any realistic simulation of alloy systems, a large number of atoms are imperative to consider and therefore, leave quantum methods impractical to use. However, semi-empirical interatomic potentials enabling accurate atomistic simulations present themselves as an alternative solution that can handle large alloy systems within a reasonable computational expense.

Daw and Baskes [47] developed the Embedded Atom Method (EAM), which has been used extensively as a semi-empirical atomistic potential for studying metals, covalent materials, and impurities [48–50]. The EAM formulation was later modified (MEAM) [51] to integrate angular dependencies of electron density and a number of single element and alloy potentials were generated using the updated formalism. Exploring the silicon-nickel alloys and interfaces [52], and tensile debonding of an aluminum-silicon interface [53] are among the few examples of the updated potentials applicability. Later, Lee and Baskes [54] improved the MEAM potential to account for the second nearest-neighbor (2NN MEAM) interactions. The 2NN MEAM formalism has been applied to capture Body Centered Cubic (BCC) metals (Fe, Cr, Mo, W, V, Nb, Ta) [55–57], Face Centered Cubic (FCC) metals (Cu, Ag, Au, Ni, Pd, Pt, Al, Pb) [58,59], Hexagonal Close Packed (HCP) metals (Mg, Ti, Zr, Zn) [60–64], metals with complex structures (Mn) [65], and covalently bonded elements (H, C, Si, Ge, N) [66–70]. In addition, binary systems have been used to study lattice defects (Fe-H) [69], structure-property relationships [71], interstitial interactions with vacancies and dislocations (Fe-C, Fe-N) [70,72], and mechanical and deformation properties (Fe-Mn) [65].

Ternary potentials pose a much greater challenge than binary potentials simply due to a lack of robust experimental data and fewer calibration parameters. Some of the recent examples of ternary applications include garnering average diffusivities of ternary alloys (Fe-Cr-Ni) [73], atomistic mechanisms for tensile fracture (Ti-Al-N) [74], nucleation kinetics of carbides and nitride (Fe-Ti-C, Fe-Ti-N) [75], modeling of a wide class of Mg alloys containing Zn (Mg-Al-Zn) [62], and structural properties of gold-silica interfaces (Au-Si-O) [76]. The greatest challenge for any interatomic potential is the

multi-component system containing more than three elements. Of the two reported higher order potentials in the NIST repository [77], only the one by Jelinek *et al.* [78] has been generated using the MEAM potential.

The current study will focus on developing a quaternary element MEAM potential for low-alloy steels with constituent elements of Fe, Mn, Si, and C. The calibration will be performed to produce single, binary, and ternary element data garnered from first-principles calculations and experiments. For binary calibrations, all possible binary interactions will be considered whereas only the imperative ternary interactions will be evaluated. Validation testing to elucidate the applicability of the potential to capture thermodynamic, kinetic, thermomechanical, and strengthening mechanisms of low-alloy steels will conclude the present study.

3.2 Single Element Interatomic Potential Development

The atomistic potential development for Fe alloys will follow a multiscale hierarchical modeling paradigm defined by Integrated Computational Materials Engineering (ICME) [79]. Since an accurate representation of the kinetics, thermodynamics, and thermomechanical response is required to capture the low-alloy steels, we calibrate the MEAM potential that can reproduce the fundamental properties of the elements. The calibration data for the interatomic potential will first rely on experimentally observed values and additional information will be collected from the lower length scale *ab-initio* calculations that can provide reliable measure of the forces on individual atoms.

3.2.1 First-Principle Calculations

The ground state energies for Fe, Mn, Si, and C are evaluated using first-principle calculations based on the Density Functional Theory (DFT). Vienna *Ab-initio* Simulation Package (VASP) code is employed to perform the calculations using the Projector Augmented-Wave (PAW) pseudo-potential and the exchange-correlation effects are treated by the Generalized Gradient Approximation (GGA) as parameterized by Perdew *et al.* [80]. To ensure energy convergence, the cut-off energy for the planewave basis of 500 eV and the gamma centered Monkhorst-Pack [81] k-point grid of 16 × 16 × 16 are used. In addition, all calculations consider spin polarization to account for magnetism. For each element, the energy-volume curves of the most stable (lowest energy) structure is determined, and in addition, at least two more crystal structures are probed.

3.2.2 MEAM Potential Parameters (Energy Versus Lattice Spacing)

In order to simulate the dynamics of a large number of atoms and molecules within a reasonable timeframe to reveal macroscopic material properties, we need a transition from the quantum to the atomic length scale. As such, a 2NN MEAM [54] potential that incorporates angular dependence of the electron density into the EAM potential and considers second nearest-neighbor interactions is used for the present study, and the full-description of the formulation can be found in the appendix [78]. Finally, the Large-scale Atomic/Molecular Massively Parallel Simulator (LAMMPS) is employed for the atomistic simulations, which is used with the MEAM parameter calibration tool [82,83] for parameter calibration.

The MEAM potential parameters for Fe, Mn, Si, and C are listed in Table 3.1 with BCC, FCC, Diamond Cubic (DC), and DC as the reference structures, respectively.

These parameters are also available in the NIST interatomic potentials repository [77]. The first step towards the parameter calibration is to compare the relative stability of the energy-volume curves produced by the MEAM potential with the DFT results. Figure 3.1 illustrates the energy versus lattice spacing of at least three crystal structures for Fe, Mn, Si, and C. The new MEAM potential parameters correctly capture the most stable structures for Fe (BCC), Mn (α-Mn), Si (DC), and C (DC), and the relative stability of supplemental structures. The c/a ratio used in hcp packing is 1.633 for secondary or tertiary HCP structures of Fe and Mn. As recorded in Table 3.2, the cohesive energies and lattice parameters of the lowest energy structures are very similar to the experimental results. Since MEAM potential requires a reference structure to describe the pair-potential, the lowest energy crystalline structures for Fe, Si, and C are also used to prescribe their reference structures. The stable, low temperature structure for Mn (α-Mn) is described by a 58 atom complex configuration that cannot easily specify the pair interaction for Mn. Therefore, FCC is chosen as the reference structure for Mn, and the MEAM parameters are adjusted such that α-Mn is the most stable structure.

Table 3.1 MEAM potential parameters for Fe, Mn, Si, and C. E_c and a_{lat} have units of eV and Å.

	E_c	a_{lat}	α	A_{sub}	$\beta^{(0)}$	$\beta^{(1)}$	$\beta^{(2)}$	$\beta^{(3)}$	$t^{(1)}$	$t^{(2)}$	$t^{(3)}$	C_{min}	C_{max}	Attrac	Repuls
Fe	4.28	2.867	5.1	0.41	3.8	1.45	1.29	2.85	-5.118	9.12	-4	0.483	2.203	0	0.012
Mn	2.855	3.693	6.154	0.92	4.3	2.227	4.155	7.452	24	29.36	-4.897	2.4	0.19	0	0.032
Si	4.63	5.43	4.882	1	3.9	7	8.78	4.8	3.01	5.61	-0.6	2	2.8	0.12	0
C	7.346	3.567	4.382	1.2	2.55	2.2	1.0	3	3.246	7.496	-2.8	2	2.8	0.12	0

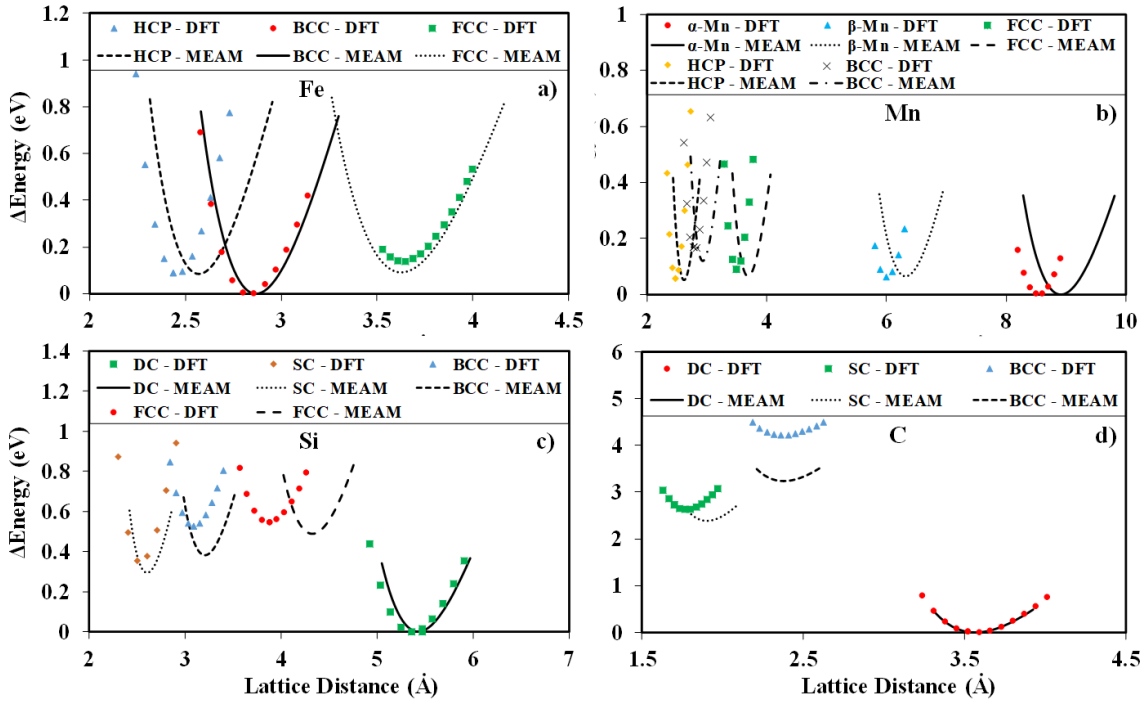

Figure 3.1 Relative energy versus lattice distance curves for a) Fe, b) Mn, c) Si, d) C. At least two crystalline structures are probed in addition to the ground states of body centered cubic (Fe), α-Mn (Mn), and diamond cubic (Si and C) for each element using DFT and captured by the present MEAM potential.

Table 3.2 Lattice parameter and cohesive energy of stable crystal structures of Fe, Mn, Si, and C. Results produced by the MEAM potential match the experimental observations by construction.

Elements	Crystal Structure	Lattice Parameters (Å)			Cohesive Energy (eV/atom)		
		MEAM	Exp.	DFT	MEAM	Exp.	DFT
Fe	BCC	2.867	2.867[a]	2.835	4.28	4.28[a]	4.98
Mn	α	8.911	8.914[b]	8.54	2.92	2.92[a]	3.876
	β	6.32	6.315[b]	6.3	0.065*	-	0.062*
Si	DC	5.43	5.43[a]	5.473	4.63	4.63[a]	4.605
C	DC	3.567	3.567[c]	3.573	7.346	7.346[d]	7.85

* Energy relative to cohesive energy of α-Mn.
[a] [84]
[b] [85]
[c] Reference 21 as reported by [86]
[d] [87]

3.2.3 Vacancy Formation Energy

The energy cost required for the formation of a single vacancy (E_f^{Vac}) in the bulk of the lowest energy structure of each element is defined using the following equation:

$$E_f^{Vac} = E_{Total} - E_{Bulk}\left(\frac{N-1}{N}\right) \tag{3.1}$$

where N is defined as the total number of atoms comprising the perfect bulk, E_{Total} is the total relaxed energy of the bulk with a single vacancy (containing $N-1$ total number of atoms), and E_{Bulk} is the total relaxed energy of a perfect bulk system. The box dimensions are identical for the bulk with and without the defect. For the *ab-initio* calculations, the bulk dimensions used for the BCC and DC systems is a 4 × 4 × 4 primitive cell, 3 × 3 × 3 for the FCC system, but 1 × 1 × 1 for α-Mn due to the fact that

the primitive cell contains 58 atoms and is fairly representative of the bulk. The bulk size incorporated in MEAM is a 5 × 5 × 5 primitive cell for BCC and DC, 4 × 4 × 4 for FCC, and 2 × 2 × 2 for α-Mn.

Table 3.3 compares the formation energies of a single vacancy using the MEAM potential for Fe (BCC), Mn (α-Mn), Si (DC), and C (DC) with experiment and DFT calculations. The interatomic potentials for Fe, Si, and C accurately reflect experimental observed energies and DFT results. A maximum deviation of 43% from the DFT results is observed for vacancy formation in Mn but is lower for the other elements (Note that there is a difference between the DFT results and experiments as well!). Vacancy formation for α-Mn was calculated using DFT and the MEAM potential by creating a vacancy in each one of the four crystallographically inequivalent sites and averaging the results. Since the t_1 MEAM parameter directly controls vacancy formation energy, a compromise was achieved where the MEAM parameter was not abnormally large (>50), and the formation energy was positive for all four sites.

Table 3.3 Formation energy of a single vacancy predicted by MEAM parameters for Fe, Mn, Si, and C compared to experiment, DFT, and literature values. Difference is between MEAM and experiment (when known) or DFT.

Elements		Vacancy Formation Energy (eV)				
		MEAM	Experimental	DFT	Literature	% Diff.
Fe		1.53	1.53[a]	2.2	1.65[c]	0
Si		3.62	3.6[b]	3.63	3.56[d], 3.67[e]	0.6
C		6.63	-	6.63	3.35[f]	0
Mn	FCC	2.88	-	2.38	-	21
	α-Mn	1.34	-	2.33	0.9 – 1.2[g]	43

[a] [88]
[b] [89]
[c] MEAM value by Jelinek *et al.* [78]
[d] MEAM results by Timonova *et al.* [90]
[e] MEAM results by Ryu *et al.* [91]
[f] MEAM value by Lee *et al.* [66]
[g] MEAM results by Kim *et al.* [65], Semi-empirical model [92,93]

3.2.4 Self-Interstitial Formation Energy

The self-interstitial is another type of point defect and the formation energy for a single self-interstitial defect, E_f^{Int}, is evaluated by the following equation:

$$E_f^{Int} = E_{Total} - E_{Bulk}\left(\frac{N+1}{N}\right) \tag{3.2}$$

where N represents the total number of atoms in a defect-free bulk, E_{Total} is the total relaxed energy of the bulk with an extra atom of the same element placed at an interstitial location, and E_{Bulk} is the total relaxed energy of the bulk with a perfect crystalline lattice structure. Because we are most interested in Fe-based alloys, five distinct interstitial positions are investigated for BCC Fe: tetrahedral, octahedral, [100] split, [110] split, and the [111] split. Only the [110] split is evaluated for the diamond cubic structures of Si

and C. Since α-Mn has a complex crystal structure, simulating an interstitial in the stable bulk is more complicated and is not presented here. The bulk structures' dimensions for BCC and DC are the same as in the previous section.

The results for the self-interstitial formation energy captured by the MEAM potential in comparison to DFT are listed in Table 3.4. DFT results indicate that the [110] split is the most stable interstitial configuration for BCC Fe, and the potential accurately captures the relative stability of the five interstitials considered. In general, the MEAM potential results are within 10% of the DFT or literature results. The MEAM parameters are specifically adjusted to ensure that of the two types of point defects, vacancies have a lower formation energy than interstitials in the bulk of the element.

Table 3.4 Interstitial formation energy for Fe, Si, and C determined by MEAM potential in comparison with DFT and literature values. Various interstitial positions are inspected for Fe, and the MEAM potential accurately predicts [110] split as the most stable interstitial.

Elements	Interstitial Positions	Interstitial Formation Energy (eV)			% Diff.*
		MEAM	DFT	Literature	
Fe	Octahedral	4.94	4.9	5.0[a]	0.8
	Tetrahedral	4.35	4.0	4.2[a]	8.8
	[100] Split	4.91	-	4.8[a]	2.3
	[111] Split	4.37	-	4.9[a]	10.8
	[110] Split	3.61	3.6	3.9[a]	0.3
Si	[110] Split	3.88	3.65	3.7[a]	6.3
C	[110] Split	14.1	13.6	12.7[b]	3.7

* Percent difference calculated w.r.t. DFT (when known) or literature results.
[a] MEAM values obtained from Jelinek *et al.* [78]
[b] MEAM results by Lee [66]

3.2.5 Elastic Constants

By independently distorting the lattice in six different directions and using the force response, a stress-strain relationship is evaluated to provide the elastic constants of the material. Table 3.5 details the results of the MEAM calibration in comparison to the experimental and DFT values. For Fe, Si, and C, the MEAM potential and experimental elastic constants agree exactly by construction. However, due to a lack of robust experimental data available for Mn, certain assumptions were made. Initially, the MEAM potential elastic constants for FCC Mn were calibrated to replicate the DFT results but the resultant elastic constants for α-Mn, especially the bulk modulus, was twice as high as the experimental observations. To rectify the situation, we employed a technique similar to Kim *et al.* [65] where the calibration target was set to half the FCC elastic constants. Consequently, the bulk modulus of α-Mn was captured to be within the experimental range and specifically, the more recent observations.

Table 3.5 Elastic constants calculated for Fe, Mn, Si, and C. Difference between MEAM potential and experimental observations are given except when otherwise noted.

Elements	Elastic Constants	MEAM	Experimental	DFT	Literature	% Diff.
Fe	B (GPa)	168	168[a]	161	166[e]	0
	C′ (GPa)	48	48[a]	56.5	43.5[e]	0
	C_{44} (GPa)	117	117[a]	68	125[e]	0
α-Mn	B (GPa)	150	60 – 158[b]	-	134[f]	0
	C′ (GPa)	86	-	-	68.5[f]	25*
	C_{44} (GPa)	45	-	-	44[f]	2.3*
Mn (FCC)	B (GPa)	202	-	277	-	27[ɥ]
	C′ (GPa)	128	-	79	-	62[ɥ]
	C_{44} (GPa)	123	-	158	-	22[ɥ]
Si	B (GPa)	98	98[c]	100	98[e]	0
	C′ (GPa)	51	51[c]	49	49[e]	0
	C_{44} (GPa)	79	79[c]	77	76[e]	0
C	B (GPa)	442	442[d]	490	422[g]	0
	C′ (GPa)	476	476[d]	485	296[g]	0
	C_{44} (GPa)	577	577[d]	619	489[g]	0

$B = (C_{11} + 2C_{12})/3$; $C' = (C_{11} - C_{12})/2$

* Percent difference calculated w.r.t. literature results.

[ɥ] Percent different calculated w.r.t. DFT results divided by half (see text for more information)

[a] [84]

[b] [94–97]

[c] [98]

[d] [99]

[e] Calculated using parameters by Jelinek *et al.* [78]

[f] MEAM results from Kim *et al.* [65]

[g] Values reported using MEAM-BO calibration by Mun *et al.* [100]

3.3 Binary and Ternary Element Interatomic Potential Development

Similar to single element potential development, a binary and ternary interatomic potential will use DFT results to garner pertinent information that can be upscaled to the atomistic length scale as calibration data for the MEAM potentials. Experimental values will take precedence as the calibration targets while *ab-initio* results will provide information that is not found from experiments. The final MEAM parameters obtained for the binary pairs, X – Y, are listed in Table 3.6. For the ternary potentials, the screening parameters involving all three atoms are the only six parameters available for calibration and are recorded in Table 3.7. The notation used to describe the screening parameters, C_{X-Y-Z}^{max} and C_{X-Y-Z}^{min}, is consistent with LAMMPS where X-Y-Z denotes atom Z screening atoms X and Y.

Table 3.6 MEAM potential parameters for the binary pair (X – Y).

	Element Pair (X – Y)					
Parameters	Fe – Mn	Fe – Si	Fe – C	Mn – Si	Mn – C	Si – C
lattice (X,Y)	L12(X_3Y)	B1	B1	L12(X_3Y)	L12(X_3Y)	dia(B3)
R_e (X,Y)	2.79	2.37	1.995	4.654	2.393	1.888
E_c (X,Y)	3.002	4.22	5.285	0.34	3.382	0.34
Alpha (X,Y)	9.33	5.7	5.45	6.8	7.2	4.54
C^{max}_{X-X-Y}	2.82	1.98	2.7	2.8	2.5	2.8
C^{min}_{X-X-Y}	2.05	1	1.6	2	1	2
C^{max}_{Y-Y-X}	2.8	2.8	2.8	2.8	2.8	2.8
C^{min}_{Y-Y-X}	2	2	0.7	2	0	2
C^{max}_{X-Y-X}	2.8	2.8	2.8	2.8	2.8	2.8
C^{min}_{X-Y-X}	2	2	2	2	2	2
C^{max}_{X-Y-Y}	2.8	2.8	2.8	2.8	2.8	2.8
C^{min}_{X-Y-Y}	2	2	2	2	2	2
attrac (X,Y)	0	0	0	0	0	0
repuls (X,Y)	0	0.5	0.008	0	0.04	0
rho0 (X)	1	1	1	0.6	0.6	1.4
rho0 (Y)	0.6	1.4	4.4	1.4	4.4	4.4

Table 3.7 MEAM potential parameters for the X – Y – Z ternary element interactions.

	Ternary Interactions (X – Y – Z)		
Parameters	Fe – Mn – Si	Fe – Mn – C	Fe – Si – C
C^{max}_{X-Y-Z}	2.8	1.2	2.8
C^{min}_{X-Y-Z}	2.0	0.29	2.0
C^{max}_{X-Z-Y}	2.8	2.8	2.8
C^{min}_{X-Z-Y}	2.0	2.0	2.0
C^{max}_{Y-Z-X}	2.8	2.8	2.8
C^{min}_{Y-Z-X}	2.0	2.0	2.0

3.3.1 Heat (Enthalpy) of Formation

The first step towards binary potential development entails obtaining the energy-volume curve for all the binary combinations using at least four crystalline structures: B_1 (rock salt), B_2 (BCC equivalent), B_3 (DC equivalent), and L_{12} (FCC equivalent). The importance of evaluating the aforementioned structures stems from the fact that any of the four can be used as a reference structure to describe the pair potential, $\phi(R_{ij})$, during binary potential development and thereby, provide a robust calibration. In addition, the equilibrium energy and lattice parameters of experimentally observed binary phases are simulated using DFT.

Once the equilibrium energy for the various crystal structures are calculated, we evaluated the likelihood of the formation of each phase at 0K using the following formula for heat of formation:

$$\Delta H = \frac{E_{Equil} - N_X E_X^{Coh} - N_Y E_Y^{Coh}}{N_X + N_Y} \tag{3.3}$$

where E_{Equil} represents the total equilibrium energy of a binary compound with elements X and Y, E_X^{Coh} and E_Y^{Coh} are the cohesive energies of elements X and Y, respectively, in their stable bulk structures, and N_X and N_Y denotes the number of atoms of element X and Y in a binary structure. For a particular stochiometric ratio, the formation of the most stable phase is associated with the lowest heat of formation. A positive value for enthalpy of formation indicates that the reaction is endothermic while a negative value exhibits an exothermic reaction.

Table 3.8 and Table 3.9 detail the results of the heat of formation and equilibrium volume, respectively, evaluated by the binary MEAM potentials. Figure A.1 and Figure

A.2 in Appendix A can help visualize the relative order of the heats of formation for the element pair X – Y as a function of atomic percentage of element Y. Priority is given to accurately capture the heat of formation and equilibrium volume of the experimentally observed structures. The next step is to ensure, where applicable, that the experimentally observed structures are the most stable structures for their specific stochiometric ratio. Finally, effort is expended to maintain the relative order of formation of the hypothetical structures. As illustrated in Table 3.8, the maximum deviation of the heat of formation for the majority of experimentally observed structures is below 40%. The $D0_3$ structure of Fe – Si system is an exception, but the experimental compounds exhibit the correct order of formation. In addition, Table 3.9 indicates that most of the equilibrium volumes calculated by the MEAM potential are within 25% of the experimental or DFT observed values, with the exception of a Fe – Mn binary and a few other outliers. Since Mn does not form any experimental structures with Fe but rather tends to mix in the Fe bulk as a solid solution, the accuracy to capture the heat of formation and equilibrium volume was leveraged for substitutional formation energies. The heat of formation and equilibrium volume of the Mn – Si and Si – C binary compounds were not calibration objectives, and therefore, the Mn – Si and Si – C binary parameters are used as variables for calibrating the ternary.

Table 3.8 Heat of formation for binary compounds evaluated by MEAM potential in comparison to experimental and DFT results. The difference is w.r.t. experiment when available, otherwise DFT.

Binary System	Alloy Phase	Heat of Formation, ΔH (eV/atom)			
		MEAM	Exp.	DFT	% Diff.*
Fe – Mn	B1	1.8	-	0.88	105
	B2	1.6	-	0.36	344
	B3	3.1	-	1.26	146
	L12 (Fe_3Mn)	0.94	-	0.12	683
Fe – Si	B1	0.24	-	0.25	4
	B2	-0.16	-	-0.48	67
	B3	-0.31	-	0.71	143
	B20	-0.40	-0.41[a]	-0.50	2.4
	L12 (Fe_3Si)	0.47	-	-0.27	274
	$D0_3$ (Fe_3Si)	0.06	-0.21[a]	-0.32	129
Fe – C	B1	0.53	-	0.53	0
	B2	1.53	-	0.83	84
	B3	0.37	-	0.42	12
	Cementite	0.0485	0.0489[b]	0.01	0.8
	L12 (Fe_3C)	1.25	-	0.72	74
Mn – C	B1	0.51	-	0.36	42
	B2	0.83	-	0.68	22
	B3	3.95	-	0.38	939
	$Mn_{12}C_4$	-0.079	-0.103[c]	-0.107	22
	$Mn_{23}C_6$	-0.11	-0.111[c]	-0.11	0.9
	Mn_7C_3	-0.07	-0.111[c]	-0.107	38
	L12 (Mn_3C)	0.70	-	0.64	9.4

* Absolute value listed for % Difference

[a] Reference 41 as cited by [101]

[b] [102]

[c] Reference 10 as reported by [103]

Table 3.9 Equilibrium volume for binary compounds calculated using MEAM parameters in comparison to experimental and DFT values. The difference is w.r.t. experiment when available, otherwise DFT.

Binary System	Alloy Phase	Equilibrium Volume, V ($Å^3$)			
		MEAM	Exp.	DFT	% Diff.
Fe – Mn	B1	172	-	93.5	84
	B2	33.8	-	21.2	59
	B3	223.6	-	116.2	92
	L12 (Fe_3Mn)	61.4	-	41.4	48
Fe – Si	B1	106.5	-	104.5	1.9
	B2	22.8	-	21.1	8
	B3	137.4	-	140.6	2.3
	B20	90.1	89.9[a]	88.3	0.2
	L12 (Fe_3Si)	47	-	45.9	2.4
	$D0_3$ (Fe_3Si)	183.2	180.3[a]	182.2	1.6
Fe – C	B1	63.5	-	63.6	0.2
	B2	14.9	-	14.9	0
	B3	78.1	-	77.1	1.3
	Cementite	154	154.3[b]	151.6	0.2
	L12 (Fe_3C)	37.5	-	39.2	4.3
Mn – C	B1	79.1	-	65.0	22
	B2	16.9	-	15.2	11
	B3	144.9	-	82.3	76
	$Mn_{12}C_4$	162.2	157.4[c]	148.9	3.1
	$Mn_{23}C_6$	1272	1189[d]	1118	7.0
	Mn_7C_3	418.8	378.3[d]	354.7	11
	L12 (Mn_3C)	39.1	-	38.8	0.8

[a] [104]
[b] [105]
[c] [106]
[d] [107]

3.3.2 Elastic Constants for the Binary Structures

The MEAM potential parameters are adjusted to ensure that the binary compounds, especially those experimentally observed, are mechanically stable using the elastic moduli. The alpha (X,Y) MEAM parameter was primarily used to calibrate the

bulk modulus. For non-cubic orthogonal structures such as cementite, $Mn_{12}C_4$, and Mn_7C_3, the bulk (B) and shear moduli (C' and C_{44}^*) are evaluated as following:

$$B = \frac{C_{11}+C_{22}+C_{33}+2(C_{12}+C_{13}+C_{23})}{9} \tag{3.4}$$

$$C' = \frac{C_{11}+C_{22}+C_{33}-C_{12}-C_{13}-C_{23}}{6} \tag{3.5}$$

$$C_{44}^* = \frac{C_{44}+C_{55}+C_{66}}{3} \tag{3.6}$$

where C_{44}^* is the average of the three shear components C_{44}, C_{55}, and C_{66}.

Table 3.10 lists the results of the elastic constants obtained for experimental and hypothetical phases. As indicated, the maximum deviation of the elastic moduli predicted by MEAM potential is within 80% of the experimental or DFT results.

Table 3.10 Elastic constants for binary compounds. Results calculated using MEAM potential are compared to experimental or literature results.

		Elastic Constants (GPa)						
		B		C′		C_{44}^*		
Binary System	Alloy Phase	MEAM	Exp. (DFT)	MEAM	Exp. (DFT)	MEAM	Exp. (DFT)	% Diff.
Fe – Mn	B2	289.8	(271)	24.6	(63)	269.9	(174)	41
Fe – Si	B20	78.7	110[a] (210)[b]	22.3	(150)[b]	57.7	(180)[b]	60
	$D0_3$	266	168[c]	103	38[c]	124.7	137[c]	79
Fe – C	Cementite	201.7	(351)[d]	99.4	(161)[d]	76	(94)[d]	33
Mn – C	$Mn_{12}C_4$	369.6	(311)[e]	202.5	(138)[e]	247.1	(132)[e]	51
	$Mn_{23}C_6$	334.9	(314)[e]	306.7	(133)[e]	233	(139)[e]	68
	Mn_7C_3	324.4	(323)[e]	314.7	(116)[e]	112.1	(105)[e]	59

% Difference calculated by averaging the percentage difference of B, C′, and C_{44} w.r.t. experimental or literature results.
[a] [108] as cited by [101]
[b] [109]
[c] Kötter *et al.* as cited by [110]
[d] DFT results by Jiang *et al.* [111]
[e] First-principles evaluation by Chong *et al.* [112]

3.3.3 Substitutional and Interstitial Formation Energy

The formation energy of a substitutional point defect, E_f^{Sub}, of type-Y atom in the bulk of type-X atoms is defined using the following formula:

$$E_f^{Sub} = E_{Total} - E_{Bulk}\left(\frac{N-1}{N}\right) - E_Y^{Coh} \tag{3.7}$$

where *N* is the total number of atoms in the bulk of type-X atoms, E_{Bulk} is the total bulk energy for the most stable structure of type-X atom with N number of atoms, E_{Total} is the total energy evaluated of one type-Y atom substituted in the bulk of type-X atoms, and E_y^{Coh} is the cohesive energy of the most stable structure for element Y. The bulk dimensions the of 5 × 5 × 5 and 3 × 3 × 3 primitive cells of BCC Fe are used in MEAM and DFT, respectively. Table 3.11 details the substitutional formation energies comparing the MEAM potential calibration to DFT results that are depicted within parentheses. Since the MEAM potential for low-alloy steels is being developed, replicating the substitutional point defect energies of the alloying elements Mn and Si in the Fe bulk is imperative. Additionally, the results indicate that a majority of the substitutional energies are in good agreement and reproduced the same sign as the DFT results. The Mn – Si and Si – C MEAM parameters were used for ternary calibration and consequently resulted in large substitutional energies. Fe in Mn bulk was also at least an order of magnitude larger than the DFT results.

Table 3.11 The formation energies of substitutional point defects for Fe, Mn, Si and C. Results obtained using DFT are presented in parenthesis while the MEAM potential values are reported without parenthesis.

	Substitutional 'Atom' Energy (eV)			
Host Atom	Fe	Mn	Si	C
Fe		0.057[a] (0.057)[b]	-1.286 (-1.28)	1.02 (2.95)
Mn*	10.4 (0.25)		22.6 (-0.98)	2.03 (2.54)
Si	2.80 (1.92)	10.8 (2.67)		12.7 (1.4)
C	8.64 (6.03)	5.25 (7.26)	17.1 (4.0)	

[a] Results produced by MEAM potential.
[b] DFT results in parenthesis.
* FCC used as bulk crystalline structure.

Having a much smaller atomic radius, carbon tends to alloy as an interstitial in Fe. Therefore, the formation energy of a carbon interstitial in an Fe bulk, E_f^{Int}, is evaluated using the following equation:

$$E_f^{Int} = E_{Total} - E_{Bulk} - E_C^{Coh} \tag{3.8}$$

where E_{Bulk} is the total bulk energy for BCC Fe atoms, E_{Total} is the total energy evaluated of one carbon atom located at an octahedral interstitial location in the bulk of Fe atoms, and E_C^{Coh} is the cohesive energy of the most stable structure for carbon. VASP calculations, employing the same aforementioned bulk dimensions, predict the interstitial formation energy to be 0.36 eV versus the substitutional formation energy of 2.95 eV. The lower formation energy indicates that carbon is more stable as an interstitial than a substitution in Fe. The MEAM parameters also demonstrate the correct order of

formation with the dilute interstitial solution energy as -1.62 eV whereas the dilute substitutional formation energy is 1.02 eV. Although MEAM potential predicted a negative interstitial formation energy for carbon in Fe, the difference of each type of point defect calculated by the MEAM potential with respect to VASP calculations remained consistent. The behavior that needs to be captured correctly, however, is the interaction of C with Mn and Si in the Fe bulk.

3.3.4 Ternary Substitutional and Interstitial Binding Energy

To calibrate the ternary potentials, the energy difference between having atoms of element Y and Z close together in the bulk of the most stable structure of element X versus having them far away is defined as the binding energy, E_{sub}^{BE}, and is evaluated as the following:

$$E_{sub}^{BE} = E_{Total}^{Y} + E_{Total}^{Z} - E_{Bulk}^{X} - E_{Total}^{Y-Z} \tag{3.9}$$

where E_{Total}^{Y-Z}, E_{Total}^{Y}, and E_{Total}^{Z} denote the total relaxed energy of Y and Z atoms, single Y atom, and single Z atom, respectively, in the bulk of element X. E_{Bulk}^{X} represents the total energy of a defect free element-X bulk. The binding energy will only be evaluated for Fe as the host atom while the pairs, Y – Z, will be located at the first (1NN) and second (2NN) nearest neighbor distances. Similar to the previous section, the bulk dimensions used for MEAM potential and DFT are consistent. Additionally, the binding energy of a substitutional pair will only be presented for Mn – Si whereas the energy of a substitution-interstitial pairs will be evaluated for Mn – C and Si – C. A schematic of the 1NN and 2NN substitutional only and substitutional-interstitial pair is depicted in Figure 3.2. A substituted atom represented with a red (dotted outline) and blue (dashed outline)

are located at the 1NN and 2NN locations with respect to the substitutional (gray) atom or the smaller (green) interstitial atom at the octahedral location.

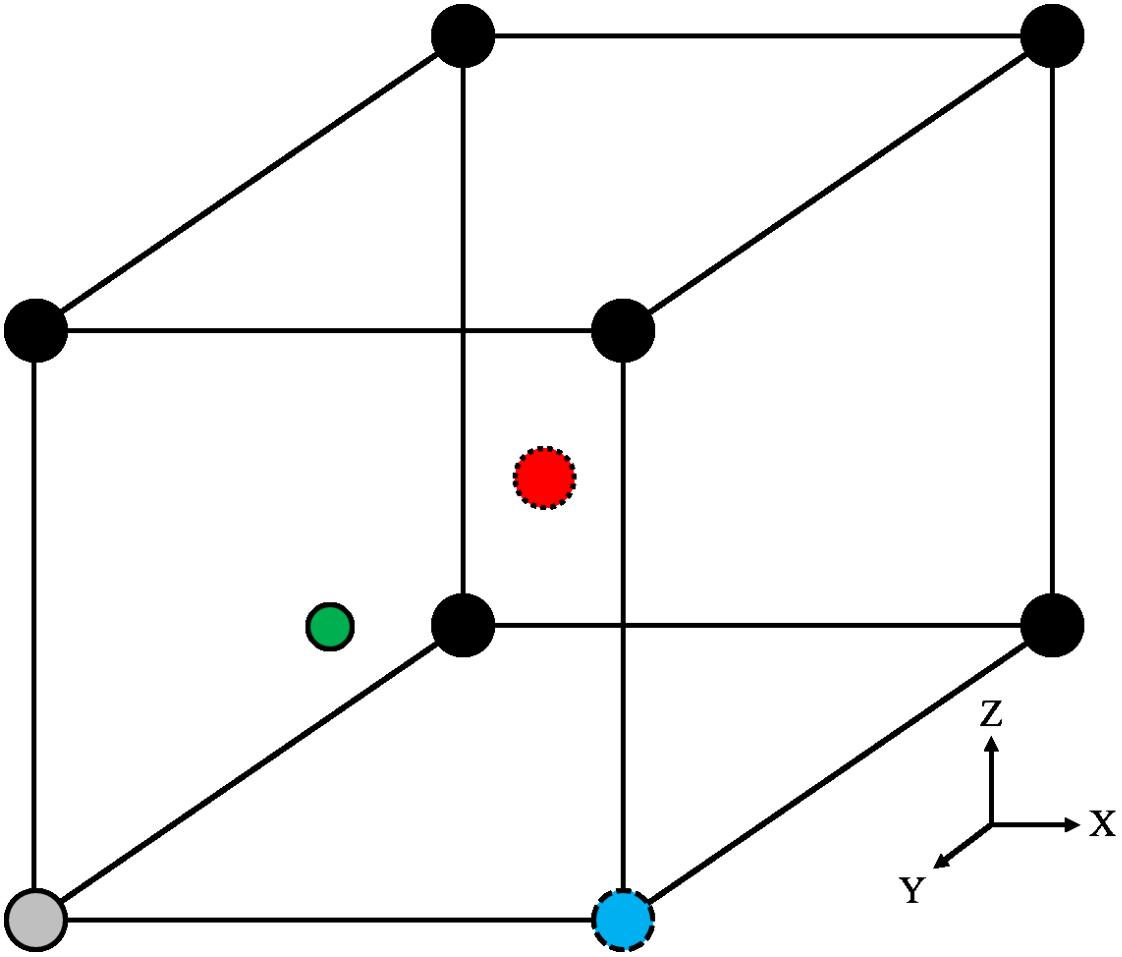

Figure 3.2 A schematic of the substituted atoms located 1NN (red, dotted) and 2NN (dashed, blue) with respect to another substituted atom (gray) or octahedral interstitial atom (blue).

Table 3.12 lists the binding energies predicted by the MEAM parameters in comparison to the DFT values for the host Fe. Positive values of the binding energy denote a 'binding' or 'attractive' behavior whereas a negative number represents a 'repulsive' trend. Results indicate that the MEAM potential values are in good agreement

with the DFT values. Accurately capturing the interaction of the multicomponent system is a primary objective. We achieve this objective by constraining the formation of Mn – Si and Si – C binary compounds, and instead use the Mn – Si and Si – C binary interaction as an input variable to calibrate the ternary interaction. Furthermore, since Fe – Mn do not form any experimentally observed binary compounds, the pair potential is also calibrated such that it can capture both the binary substitutional formation energy and ternary binding energies.

Table 3.12 Ternary binding energies for substitutional pair of Mn-Si and substitution-interstitial pairs of Mn-C and Si-C in Fe bulk. The interaction of impurity pairs are evaluated at 1NN and 2NN. Results evaluated using DFT are represented in parenthesis whereas MEAM potential values are listed without parenthesis.

		Binding Energy (eV)		
		Substitutional Pair	Substitution – Interstitial Pair	
Host Atom	Pair Location	Mn – Si	Mn – C	Si – C
Fe	1NN	-0.14[a] (-0.14)[b]	-2.55 (-0.47)	-0.37 (-1.01)
	2NN	-0.67 (-0.17)	-0.17 (-0.60)	-0.88 (-1.25)

[a] Results produced by MEAM potential.
[b] DFT results in parenthesis.

3.4 Potential Validation Testing

The final step is to determine the applicability of the MEAM potential. A number of simulations were performed at finite temperatures to encapsulate the thermodynamic and kinetic properties of Fe and low-alloy steels. First, the coefficient of linear thermal

expansion is evaluated for pure Fe using a 2000 atom system with periodic boundaries. The box was initially equilibrated using an NPT ensemble for 0.1 ns to achieve the correct zero pressure volume at a given temperature. A final equilibration was conducted for an interval of 1 ns, and the lattice dimensions were averaged over the time interval to calculate the linear thermal expansion coefficient. The same set of simulations was also used to evaluate the heat capacity of pure and alloyed iron. Table 3.13 and Table 3.14 compares the results of the coefficient of linear thermal expansion and heat capacity of iron of the MEAM potential results to the experimental results. At 300K, the linear thermal expansion and heat capacity for pure iron were within 4% of the experimentally observed values. Both the physical properties of the Fe alloys increased when doped with Mn and Si, demonstrating that the trend moved in the right direction but not as large as measured. Finally, the specific heat capacity and thermal expansion of a multicomponent low-alloy steel was evaluated, and the results indicated that the MEAM potential results were within 2.3% of experimental observations.

Table 3.13 Coefficient of linear thermal expansion evaluated for Fe at 300K using present MEAM potential and compared to experimental results.

	α_l at 300K (10^{-6} K^{-1})		
	MEAM	Experiment	% Difference
Fe	11.15	11.6[a]	3.9
Fe – 2% Mn	11.73	12.7[a,b]	7.6
Fe – 1% Si	11.48	12.2[a]	5.9
Fe – 1.25% Mn, 0.6% Si, 0.25% C	11.83	12.0[c]	1.4

[a] [113]
[b] Experimental value for Fe – 2.8% Mn.
[c] 1522 low-alloy steel [114]

Table 3.14 Heat capacity calculated for pure Fe and alloys at 300K. Results calculated using MEAM potential are compared to experimental observations.

	C_p at 300K (J g^{-1} K^{-1})		
	MEAM	Experiment	% Difference
Fe	0.467	0.4676[a]	0.12
Fe – 2% Mn	0.4709	0.5016[a]	6.12
Fe – 1% Si	0.4732	-	-
Fe – 1.25% Mn, 0.6% Si, 0.25% C	0.475	0.486[b]	2.3

[a] [115]
[b] 1522 low-alloy steel [114]

In addition, the self-diffusion coefficients were also evaluated for Fe using a single crystal comprising 16,000 atoms. The system was equilibrated using the NPT ensemble for 0.2 ns followed by an introduction of a small number of random vacancies. Finally, a canonical (NVT) ensemble was simulated for 1 ns where the atom positions were recorded every 500 fs. The atom position vectors are used to calculate the self-

diffusion coefficients using Einstein's formulation [116] relating mean square displacement as a function of observed time with the following equation:

$$D = \frac{1}{2d} \lim_{t \to \infty} \frac{\langle [r(t_0+t) - r(t_0)]^2 \rangle}{t} \tag{3.10}$$

where *d* is the dimensionality of the system and the angled brackets signify that an ensemble average over all molecules and time origins must be considered. In order to observe diffusivity of atoms within a reasonable timeframe, an excess number of vacancy concentrations, C_v^{ex}, are introduced in the simulation environment. This requires the simulated diffusivity, D_{sim}, to be adjusted for the equilibrium vacancy concentration, C_v^{eq}. The actual diffusivity, D_{real}, of the system is then evaluated using the following equation:

$$D_{real} = \frac{C_v^{eq}}{C_v^{ex}} D_{sim} \tag{3.11}$$

where the equilibrium vacancy concentration, C_v^{eq}, is obtained using:

$$C_v^{eq} = \exp\left[-\frac{H_f^v - TS_f^v}{k_B T}\right] \tag{3.12}$$

where H_f^v is the vacancy formation enthalpy, S_f^v is the vacancy formation entropy, and k_B is the Boltzmann constant. The vacancy formation entropy was taken from literature [117] as $2.20k_B$.

To evaluate uncertainty, each simulation is conducted three times with different seed numbers for the porosity and temperature, and 95 percent confidence intervals were employed for both temperature and the self-diffusion coefficients. Figure 3.3 shows that the MEAM potential calculated self-diffusion coefficients for pure Fe compared well with the experimental results [118].

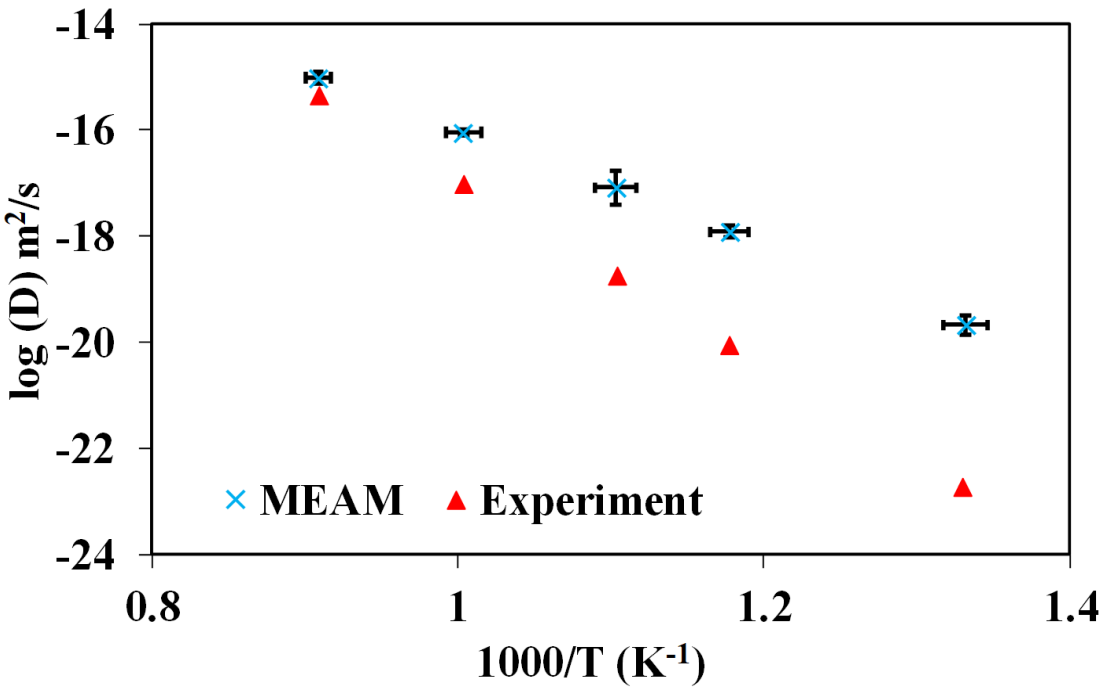

Figure 3.3 An Arrhenius plot of self-diffusion coefficients as a function of temperature. Results obtained by MEAM potential are in overall agreement with experimental values.

Since dislocation motion across a slip plane and in the slip direction is one of the possible mechanisms of plasticity in BCC Fe, we evaluate the change in energy as the stacking sequence of a perfect bulk single crystal is changed at 0K. Figure 3.4a details the Generalized Stacking Fault Energy (GSFE) as a function of the normalized displacement in the [111] slip direction. A comparison of the GSFE curve evaluated using the present MEAM potential against DFT data produced by Jelinek *et al*. [78] indicates similar behavior. In fact, the present MEAM potential predicts a higher peak stacking fault energy than the MEAM potential in [78]. Additionally, the effect of alloying elements on the stacking fault energy is evaluated for Mn, Si, C, and a multicomponent system, as depicted in Figure 3.4b. The addition of Mn and C increased the stacking fault energy

with respect to pure Fe while the addition of Si caused the stacking fault energy to remain approximately the same as pure Fe. A multicomponent system exhibited a decrease in peak stacking fault energy as well.

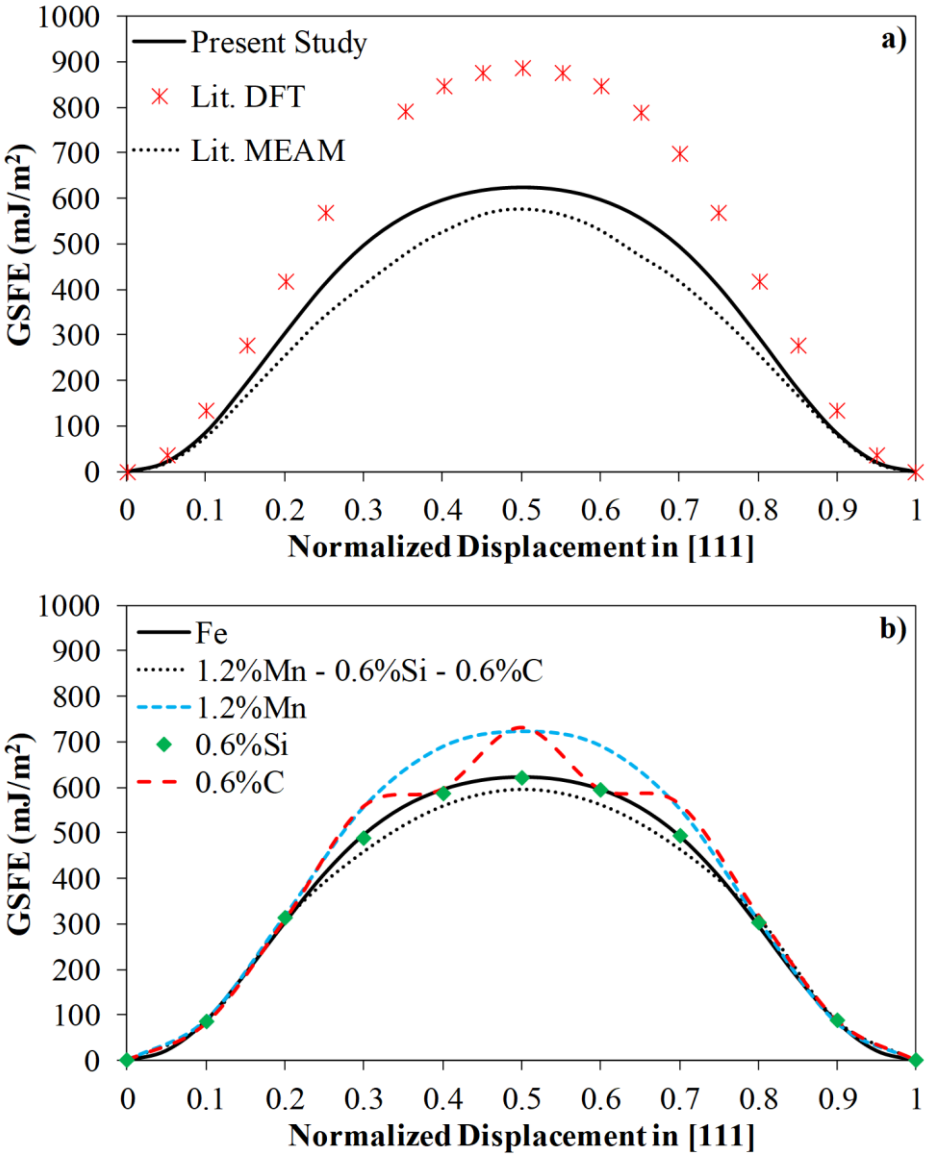

Figure 3.4 Generalized Stacking Fault Energy (GSFE) evaluated as a function of normalized displacement in the slip direction of [111]. a) GSFE obtained from the present MEAM potential is compared against DFT and literature MEAM calibration of Fe. b) Effect of alloying element on the GSFE is evaluated and compared against the GSFE of pure Fe.

The potentials are also tested to observe the thermomechanical response of bulk single crystal bulk Fe under a tensile loading condition. A 62,500 atom system with lattice dimensions of 50 × 25 × 25 is used for the bulk mesh with a free surface only in the z-direction. An initial equilibration at temperature using a NPT ensemble was conducted for 50 ps, which was followed by box deformation in the x-direction at a strain rate of 10^8/s in tandem with an NPT zero-pressure barostat in the y-direction. To ascertain the temperature dependence on the mechanical response, simulations were conducted over a temperature range from 100K to 600K. Figure 3.5 illustrates the true stress-true strain behavior for Fe where the failure criterion is defined as reduction from peak stress by 20%. Three simulations were conducted at each temperature that yielded error bars for failure elongation with a 95% confidence interval. Table 3.15 provides the modulus, tensile strength, and failure elongation garnered from the stress-strain curves as a function of temperature. The mechanical response follows an Arrhenius trend dictated for general materials whereby an increase in temperature results in strength reduction and improved ductility.

Table 3.15 Variation in modulus, tensile strength, and failure elongation of Fe bulk as temperature increases.

Temperature (K)	Modulus (GPa)	Tensile Strength (GPa)	Failure Elongation (%)
100	134.8	8.66	9.58 ± 0.13
300	123.4	7.49	10.46 ± 0.30
450	108.9	6.65	11.03 ± 0.23
600	101.8	5.94	11.62 ± 0.13

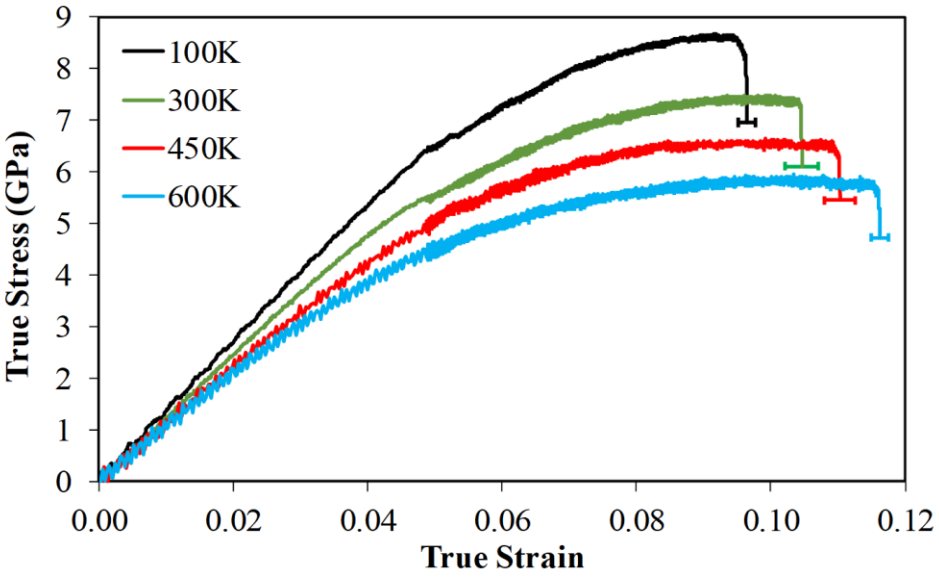

Figure 3.5 The mechanical response of Fe bulk under uniaxial tensile loading conditions illustrating the experimental expected trend that as the temperature increases the work hardening rate decreases. We also note that as the temperature increases, the elongation to failure increases.

Finally, the solid solution strengthening effect of alloying elements in iron is explored. A solute atom, depending upon the substitutional or interstitial nature, imposes a tensile or compressive strain on the host atoms. Similarly, an extra half-plane of atoms in an edge dislocation results in a compressive and tensile lattice strain on the atoms surrounding the dislocation line. During mechanical loading, the solute atoms diffuse around a dislocation core and tend to position themselves at locations such that the overall strain is reduced, thereby requiring a greater stress, in comparison to the pure element, to initiate dislocation mobility and cause plastic deformation. A simulation box with cell dimensions of 69.5 × 100 × 6, with all periodic boundaries, is setup and contains 62,250 atoms. An edge dislocation having line direction perpendicular to the z-direction situated in the center of the simulation box is used to determine the relaxed binding

energy of alloying elements as a function of atom position in the vicinity of the dislocation core. A positive binding energy indicates a thermodynamically favorable location in comparison to an impurity-free dislocation, and a negative binding energy indicates a thermodynamically unfavorable location in comparison to an impurity-free dislocation. For ease of obtaining results, the simulations were conducted at 0K.

Figure 3.6a, Figure 3.6b, and Figure 3.6c depicts the binding energy plot of Mn, Si, and C atoms, respectively, near an edge dislocation core. Mn, having a larger atomic radius than Fe, will introduce a compressive lattice strain on the host atom as a substitutional point defect. Therefore, Mn will ideally be situated on the tensile side of an edge dislocation in BCC Fe. Figure 3.6a for Mn indicates that the binding energy is lower on the tensile side of the dislocation, which is below the horizontal dashed black line. Conversely, Figure 3.6b depicts that Si is favored to be located on the compressive side of the dislocation core since Si has a smaller atomic radius than Fe. Finally, C atoms, being much smaller than Fe, are thermodynamically favorable to be alloyed as interstitial point defects than as a substitution. However, a carbon atom is still larger than the space available at the octahedral interstitial position and, therefore, imposes compressive lattice strains on the surrounding Fe atoms. Consequently, C atoms will ideally be located at the tensile side of the dislocation line as portrayed in Figure 3.6c.

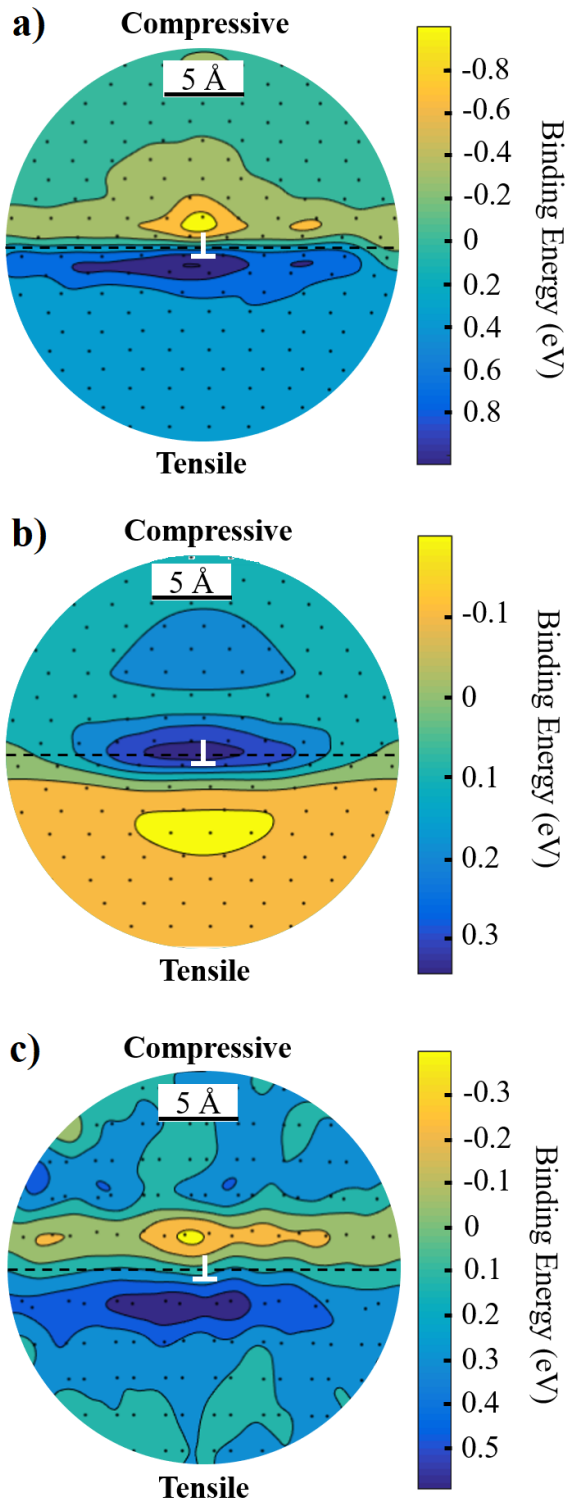

Figure 3.6 Binding energy of one substitutional atom: a) Mn, b) Si, and c) interstitial carbon in Fe as a function of position in the vicinity of a dislocation core.

We also examined the effect of alloying elements on the dislocation velocity as a function of applied shear stress. The simulation box size is identical as before except for periodic boundaries in both x and z to allow for an infinitely long dislocation that can move across the boundary in the x-direction. An initial equilibration at 300K using NVE ensemble for 10 ps is conducted. Application of a shear stress is achieved by applying an instantaneous force in the x-direction to approximately 10% of rigid atoms from the bottom schematically illustrated in Figure 3.7.

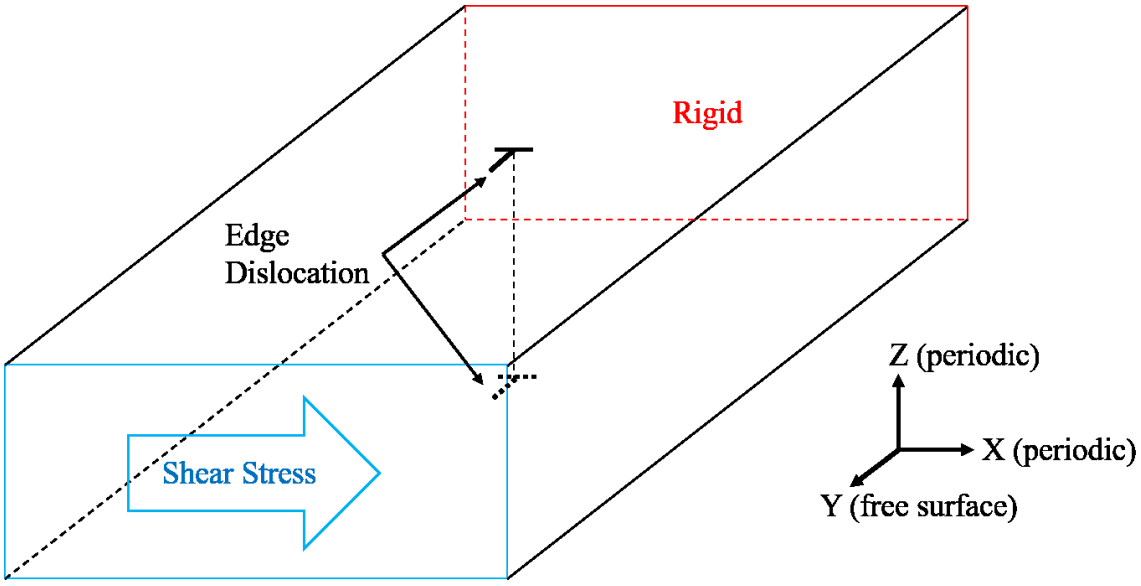

Figure 3.7 Schematic of an edge dislocation in BCC Fe. Periodic boundary conditions are applied in the x and z-direction.

Initially, the critical shear stress for a dislocation to move in pure Fe was evaluated, and the results indicated that an approximate shear stress of 10 MPa was required to mobilize the dislocation continuously through the periodic boundary in the x direction. To assess the impact of individual alloying elements on the critical shear stress

required for a dislocation to move, two atoms of an alloying element were placed randomly around the preferred location of the dislocation core. The applied shear stress increased until the dislocation moved through the periodic boundary in the x-direction. For Mn, Si, and C, the critical shear stresses were 95 MPa, 98 MPa, and 92 MPa, respectively. As predicted, the doping pure Fe with alloying elements in small quantities adds resistance to slip, which results in pinning the dislocation core. Consequently, a higher global stress is required to initiate plastic deformation via dislocation motion.

3.5 Conclusions

A quaternary element MEAM potential involving Fe, Mn, Si, and C was developed to simulate low-alloy steels using a hierarchical multiscale modeling paradigm. First, single element interatomic potentials were calibrated using experimental observations and first-principle calculations of the cohesive energy, lattice parameters, elastic constants, and point defect formation energies of vacancies and interstitials. Then, the calibration of binary element pairs was performed. This calibration entailed using the heat of formation, equilibrium volume, and elastic constants of binary compounds along with substitutional and interstitial formation energies as calibration targets. Finally, ternary interactions of Mn, Si, and C in Fe bulk were considered using substitutional and interstitial binding energies that were compared to *ab-initio* calculations.

A vital aspect of this atomistic study was to discern if the newly developed interatomic potentials could be applied to garner thermodynamic, kinetic, and mechanical data. Simulation results of the linear thermal expansion, heat capacity, and self-diffusion coefficients showed a great comparison to the experimental data found in the literature for Fe and its alloys. In addition, solid-solution strengthening mechanisms due to Mn, Si,

and C in Fe were successfully verified by this potential, thereby extending confidence in the current MEAM potential to capture a wide array of atomistic phenomenon in a low-alloy steel.

3.6 Acknowledgements

This work was funded by the National Science Foundation (NSF) under contract number 1506878**.** The authors would also like to thank the Center for Advanced Vehicular Systems (CAVS) at Mississippi State University for supporting this work.

CHAPTER IV

AN FE-MN-SI-C-AL-ZN-O MODIFIED EMBEDDED ATOM METHOD (MEAM) POTENTIAL TO STUDY THE INTERFACIAL STRUCTURES OF THE INHIBITION LAYER, STEEL SUBSTRATE, AND OXIDES IN GALVANIZING STEEL ALLOYS

4.1 Introduction

New generation advanced high strength steels (AHSSs) are the most affordable mass reduction solution for lightweight vehicles, according to the National Highway Traffic Safety Administration (NHTSA) report, "Mass Reduction for Light-Duty Vehicles for Model Years 2017-2025" published in December 2012, and are key enablers in allowing such vehicles to achieve US Environmental Protection Agency fuel economy and emissions goals for 2025. AHSSs are the fastest-growing structural materials in US-produced vehicles on a mass fraction basis, because of their ability to satisfy weight reduction and safety demands, while offering low cost and recyclability. As the thickness of these high strength steels is reduced to less than 1.0 mm, the provision of corrosion protection for the expected life of the vehicle is becoming increasingly critical. Metallic zinc (Zn) protective coatings are able to provide the required barrier and galvanic corrosion protection [15,119].

For automotive applications, hot-dip galvanizing and galvannealing are the most common industrial practices. In galvanizing, a pre-heated steel strip is submerged into a Zn bath. A series of complex reactions take place at the interface between the steel substrate and the liquid Zn, including wetting of liquid Zn on the solid substrate, dissolution of iron (Fe) in the bath liquid, formation of intermetallic compounds by solidification, diffusion-controlled phase transformations, and solidification of Zn [15,119]. These interface reactions take place rapidly, and the interface structures determine the success or failure of forming, welding and corrosion protection capabilities of the steels and, therefore, the use of steels in vehicles. Kinetics dominates these reactions and thermodynamic equilibrium may not be reached.

To prevent formation of brittle Fe-Zn intermetallic compounds, a small amount of aluminum (Al) is usually added to the Zn bath [15,119,120]. Because Al has a much greater affinity for Fe than Zn, a thin film or discontinuous inhibition layer (Fe_2Al_5 or $Fe_2Al_{5-x}Zn_x$) forms first (with a thickness typically less than 100 nm), and subsequent growth of intermetallic phases and Zn overlay follows. The interfaces between the steel substrate, the inhibition layer, and the intermetallic phases are crucially important in determining the structure and properties of the coating. Galvanizing process strongly depends on the chemistry of the Zn bath (i.e., the effective Al concentration), the chemistry of subsurface alloying elements, microsegregation at grain boundaries, and the characteristics of oxides [15,119,120]. Previous studies have shown that the morphology of the interfacial layers and the type of the inhibition layer changes with variations in Al concentration in the Zn bath [121–123].

Higher concentrations of the alloying elements are needed to improve the ductility and strength of new AHSSs. Particularly, manganese (Mn) and silicon (Si) concentrations are increased. However, as these multiphase, highly alloyed steels enter the market, the ability to predict and, therefore, control the interfaces formed between the Zn coating and steel becomes increasingly complex. For instance, selective high-temperature oxidation of Mn and Si takes place on the surface of these steel grades when they are prepared for Zn coating. The type and morphology of these oxides, i.e. granular or film-like, binary, ternary or higher order, change with processing conditions. Mn and Si oxides cannot easily be reduced by hydrogen and these oxides remain on the surfaces. Not only external oxidation, but also internal oxidation occurs in the subsurface regions of the steel strip. Recent studies have shown that the type and morphology of the oxides on the strip surface change as the dew point decreases [22]. Specifically, the morphology of the oxides changes from relatively loose granules to dense and smooth films with a decrease in the dew point. How these oxides affect the subsequent galvanizing process remains a concern. The dew point also affects the formation of the inhibition layer. As the dew point decreases, the morphology of the inhibition layer becomes increasingly discontinuous [22]. These changes may affect subsequent coating development in terms of the formation of inhibition layer and coating growth. Moreover, the nature of the underlying multiphase steel substrate changes with processing, including phase (austenite, ferrite, and martensite), grain size, and grain orientation variations as well as surface composition changes, such as local decarburization. These changes affect the reaction of the Zn coating, which always contains a dilute amount of Al, and the interface layer that is produced. The initially formed Fe_2Al_5 interface layer is confined in a

boundary with a thickness of a few tens of nanometers, whereas the subsequent Zn coating is on the order of 10 microns [120]. Such a fine scale morphology poses a challenge to experimental studies of interface reactivity. Previous studies have employed scanning electron microscopy (SEM) and/or energy-dispersive X-ray spectroscopy (EDS), among other techniques, to investigate the morphology and chemical composition of the oxides and the inhibition layer [5].

On the other hand, physics-based, multiscale modeling of galvanizing of AHSSs has not been attempted, despite the long history of experimental studies on the same subject. We propose to combine the cutting-edge analytical techniques and multiscale modeling to study oxidation and interface reactivity of galvanizing and galvannealing of AHSSs. The length scales span from electronic up to meso-scale. The physical properties of interfacial phases and structures will be calculated and simulated at the electronic and atomic scale. The data obtained from these lower length scale simulations will be used as inputs for phase-field models of oxides, intermetallic phases and Zn overlay. The numerical models will be calibrated and validated by experimental results. As we are approaching the limits of our understanding of how these interfaces are formed as a function of metallurgical process variables through conventional methods, cutting-edge characterizing techniques and cross-length scale modeling may advance our current knowledge to a new level.

The goal of this research is to calibrate a seven-element MEAM potential to study the interfacial microstructures and properties in galvanized low-alloy steels. Cutting-edge experimental techniques will guide multiscale modeling and simulations to better understand the interfacial reactions and their various effects on the interface properties,

and to develop physics-based models to predict the kinetics of interfacial interactions and structures during galvanizing of low-alloy steels under different manufacturing conditions.

4.2 Single Element MEAM Potentials

The atomistic potentials for Al and Zn followed the potential development procedure described in section (add section cross-reference). Table 4.1 lists the MEAM potential parameters for Al, Zn, and O with FCC, HCP, and 'dim' (dimer) as the reference structures, respectively, and are available in the NIST potentials repository.

Table 4.1 MEAM potential parameters for Al, Zn, and O. E_c and a_{lat} have units of eV and Å.

	E_c	a_{lat}	α	A_{sub}	$\beta^{(0)}$	$\beta^{(1)}$	$\beta^{(2)}$	$\beta^{(3)}$	$t^{(1)}$	$t^{(2)}$	$t^{(3)}$	C_{min}	C_{max}	Attrac	Repuls
Al	3.39	4.05	4.674	1.06	1.967	4.6	5.84	1	5.61	-2.35	8.4	2.746	0.79	0.117	0.125
Zn	1.3224	2.7814	7.06	0.7	1.8	1	5.3	7.11	22.471	-17.3	57	2.7	1.32	0.1	0.155
O	2.558	1.21	4.59	0	0.31	1	1	1	10.09	10.1	1.5	2.8	2.0	0	0

The MEAM potential for O was initially obtained from Gao *et al*. [124] but the functional form of the background electron density was modified to be consistent with the potentials developed in this study. A detailed description of the evaluated properties of Al and Zn are presented in the following subsections.

4.2.2 Aluminum MEAM Potential

The energy versus lattice spacing curves, elastic constants, vacancy formation energy, and self-interstitial formation energies for Al were evaluated using the MEAM potential and compared against the experimental observations or DFT calculations, when applicable. Table 4.2 details the results from the MEAM potential calibration in

comparison to experimental, DFT, and literature results, and Figure 4.1 illustrates the energy versus lattice distance curves for FCC, BCC, and HCP structures of Al. The MEAM potential accurately predicted FCC as the most stable crystalline structure and correctly captured the relative stability of supplemental BCC and HCP structures. An ideal c/a ratio of 1.633 was used for simulating the HCP structure. Additionally, the cohesive energy and lattice parameter of FCC Al were calibrated to match the experimental observations, as recorded in Table 4.2.

Table 4.2 Cohesive energy, lattice parameter, elastic constants, vacancy formation energy, and self-interstitial formation energies for FCC Al. The results obtained by the MEAM potential are in good agreement with the experimental observations (when available) or DFT results. Three distinct self-interstitial configurations were probed and the MEAM potential accurately predicted the relative stability of the point defects.

Aluminum						
Properties		MEAM	Exp.	DFT	Literature	% Diff.
Cohesive Energy (eV/atom)		3.39	3.39[a]	3.74	3.353[e]	0
Lattice Parameter (Å)		4.05	4.05[b]	4.04	4.05[e]	0
B (GPa)		79.4	79.4[c]	77.9	78.9[f]	0
C′ (GPa)		26.2	26.2[c]	8.0	26[f]	0
C_{44} (GPa)		31.6	31.6[c]	22.6	45.4[f]	0
Vacancy Formation (eV)		0.67	0.67[d]	0.656	0.68[g]	0
Interstitial Formation (eV)	100 Split	3.01	-	3.22	2.77[e]	6.5
	Tetra-hedral	3.60	-	3.74	3.32[e]	3.7
	Octa-hedral	3.48	-	3.44	3.26[e]	1.2

[a] [84]
[b] Reference 28 [125] as cited in [126]
[c] [127]
[d] [128]
[e] MEAM results by Jelinek *et al*. [78]
[f] MEAM results by Pascuet and Fernandez [129]
[g] MEAM value by Lee *et al*. [58]

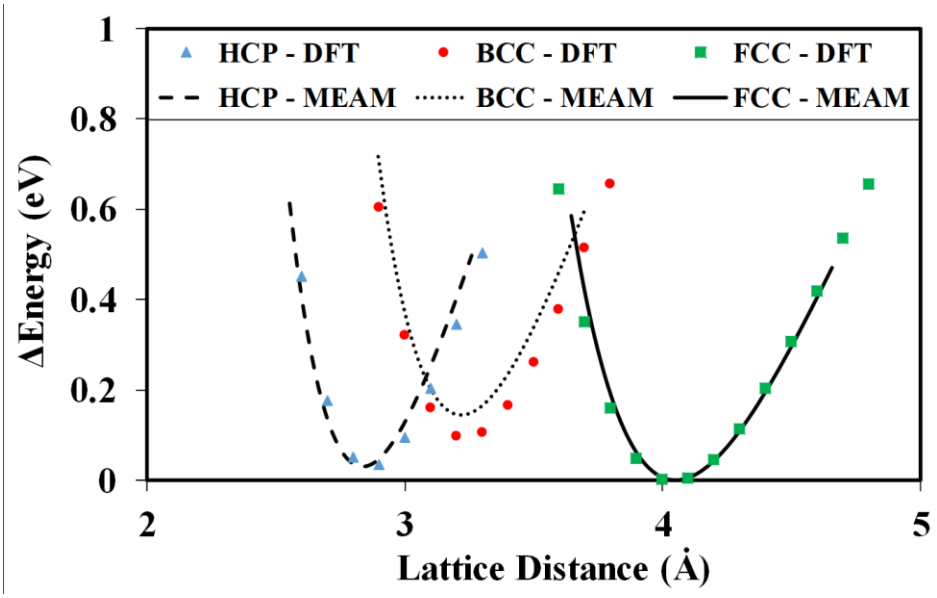

Figure 4.1 The relative energy versus lattice distance for FCC, HCP, and BCC crystalline lattices of Al evaluated by DFT and the MEAM potential. The relative stability of the three structures was accurately predicted by the MEAM potential.

Adding to the robustness of the interatomic potential, the elastic constants for FCC Al were calibrated to exactly reproduce the experimental values by construction, as listed in Table 4.2. Furthermore, point defect formation energies of vacancy and self-interstitial were evaluated for FCC Al. For *ab-initio* and MEAM potential calibration calculations of vacancy formation energy, the bulk dimensions used for FCC Al is 3 × 3 × 3 primitive cell and 4 × 4 × 4 primitive cell, respectively. As illustrated in Table 4.2, the calibrated Al MEAM potential replicated the experimental values of vacancy formation energy. The calculations for self-interstitial energies employed the same bulk size as vacancy formation energy and probed three distinct interstitial configurations of tetrahedral, octahedral, and [100] split. DFT results indicated that the [100] split was the

most stable configuration, and the MEAM potential correctly captured the relative stability of the self-interstitials with a maximum deviation of 6.5% from the DFT results.

4.2.3 Zinc MEAM potential

Zinc has a stable crystalline structure of HCP with a c/a packing ratio that is 1.136 times greater than the ideal packing ratio of 1.633 for HCP structures. Baskes [130] has proven that the MEAM formulation, in its current state, cannot simultaneously capture the large c/a ratio and ensure that HCP is the most stable lattice configuration. Furthermore, obtaining a c/a ratio greater than ideal appeared to be roughly correlated to the C_{33} elastic constant. This constraint poses a calibration challenge and resulted in a lack of published MEAM potential for Zn up till very recently in 2018. Jang *et al*. [63] prioritized capturing the relative stability of the HCP structure whereas Dickel [62] *et al*. sacrificed the relative stability to accurately capture the c/a ratio, lattice parameter, cohesive energy, and the C_{33} elastic constant. For the current study, we used the potential calibrated by Dickel *et al*. [62] as a starting point. The potential was recalibrated to be consistent with the use of ibar, the functional form used to compute the background electron density, as -5 in LAMMPS.

Table 4.3 The cohesive energy, lattice parameters, elastic constants, vacancy formation energy, and (0001) surface formation energy for HCP Zn. Results garnered by the MEAM potential are compared against experimental values.

Zinc						
Properties		MEAM	Exp.	DFT	Literature	% Diff.
Cohesive Energy (eV/atom)		1.35	1.35[a]	1.26	1.09[f], 1.35[g]	0
Lattice Parameter	a (Å)	2.665	2.665[b]	2.665	2.78[f], 2.668[g]	0
	c (Å)	4.944	4.945[b]	4.946	4.5[f], 4.947[g]	0
c/a ratio (relative to ideal)		1.136	1.136[b]	1.137	0.992[f], 1.134[g]	0
C_{11} (GPa)		170.5	177[c]	-	133.4[f], 151.6[g]	3.7
C_{12} (GPa)		52.6	34.8[c]	-	47[f], 46.7[g]	51
C_{13} (GPa)		61.8	52.8[c]	-	41.5[f], 56.5[g]	17
C_{33} (GPa)		61.4	68.5[c]	-	122.4[f], 67.8[g]	10
C_{44} (GPa)		49.7	45.9[c]	-	34.1[f], 45.2[g]	8.3
Vacancy Formation (eV)		1.44	0.5[d]	0.43	0.44[f], 1.52[g]	188
(0001) Surface Formation (mJ/m^2)		575	575[e]	-	448[f], 524[g]	0

[a] [84,131]
[b] [132]
[c] [133]
[d] [134]
[e] [135]
[f] MEAM values by Jang *et al*. [63]
[g] MEAM results by Dickel *et al.* [62]

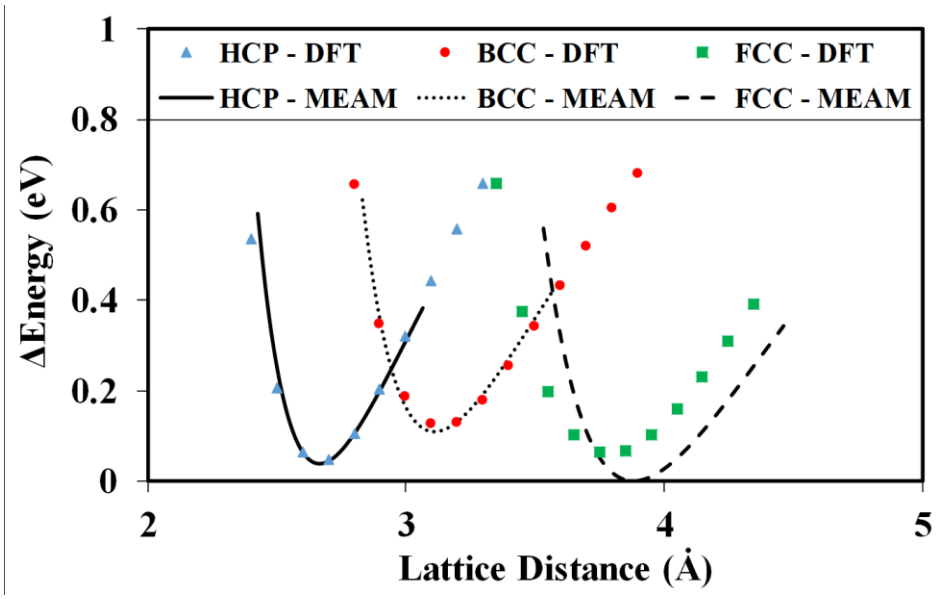

Figure 4.2 The relative energies of HCP, FCC, and BCC crystal structures of Zn are plotted against lattice distance for DFT and the MEAM potential. FCC Zn was calibrated as the most stable structure with HCP and BCC as secondary and ternary structures.

Table 4.3 details the cohesive energy, lattice parameters, elastic constants, vacancy formation energy, and surface formation energy calibrated by the MEAM potential in comparison to experimental, *ab initio*, and literature results. The cohesive energy and lattice parameters, a and c, were calibrated to replicate the experimental observation. In addition, the c/a ratio of HCP packing for final, relaxed structure was found to be independent of the initial c/a ratio. Figure 4.2 depicts the energy versus lattice spacing curves for HCP, FCC, and BCC structure of Zn. As mentioned above, the relative stability of HCP Zn was sacrificed, resulting in FCC as the most stable structure. Zn in the BCC configuration, however, exhibited the correct order of formation as being the least stable of the three crystalline structure. The elastic constants were found to reasonably agree with the experimental observation with a maximum discrepancy of 51%

occurring in capturing the C_{12} elastic constant. For the calculations involving vacancy formation energy, a bulk dimension of 4 × 2 × 2 orthogonal HCP cell and 8 × 4 × 4 orthogonal HCP cell were used for DFT and MEAM potential. Both the vacancy and surface formation energies were sensitive to the t_1 parameter and calibrating to the experimental vacancy formation energy resulted in a negative surface formation energy for the basal plane. Since Dickel *et al*. established that the Zn potential has a metastable HCP structure, the vacancy formation energy was omitted as a calibration target and we focused on capturing the surface formation energy of HCP Zn. As a result, the discrepancy in vacancy formation energy is 188% but the surface formation energy replicated the experimental observations.

4.3 Binary Element Interatomic Potential Development

As previously mentioned, the binary element MEAM potential calibration followed the methodology detailed in section 3.3. Table 4.4 and Table 4.5 list the binary parameters for the pairs involving the elements of Fe, Mn, Si, Al, Zn, C, and O. Since the binary parameters for the Fe, Mn, Si, and C are listed in the previous chapter, the binary parameters listed in Table 4.4 and Table 4.5 will omit interactions described before.

Table 4.4 MEAM potential parameters for the binary pairs (X – Y) of Fe, Mn, Si, Al, Zn, and C

Parameters	Element Pair (X – Y)								
	Fe – Al	Fe – Zn	Al – Zn	Mn – Al	Mn – Zn	Si – Al	Si – Zn	Al – C	Zn – C
lattice (X,Y)	L12	B1	L12	B1	B2	B2	B1	B1	B1
R_e (X,Y)	2.576	2.461	2.846	2.5	2.615	2.737	2.573	2.121	2.201
E_c (X,Y)	4.46	2.268	2.887	2.952	2.019	3.945	2.564	4.998	2.664
Alpha (X,Y)	5.55	6.0	4.7	4.0	6.0	4.6	5.2	4.8	5.0
C_{X-X-Y}^{max}	2.006	2.8	1.8	1.2	2.8	2.8	2.5	2.4	2.8
C_{X-X-Y}^{min}	1.422	2.0	0.4	0	2.0	2.0	0.1	1.6	0.6
C_{Y-Y-X}^{max}	2.998	2.8	1.2	3.0	2.95	2.8	2.8	2.35	1.7
C_{Y-Y-X}^{min}	1.318	2.0	0	1.7	0.1	2.0	1.6	0.05	0.8
C_{X-Y-X}^{max}	2.8	2.8	2.8	2.8	2.8	2.8	2.8	1.1	1.5
C_{X-Y-X}^{min}	2.0	2.0	0	2.0	2.0	2.0	2.0	0	0
C_{X-Y-Y}^{max}	2.8	2.8	2.8	2.0	1.1	2.8	2.95	2.8	2.8
C_{X-Y-Y}^{min}	0.2	2.0	2.0	0	0	2.0	2.0	2.0	2.0
attrac (X,Y)	0	0.03	0.2	0.2	0	0.1	0	0	0
repuls (X,Y)	0	0	0	0	0	0.2	0	0	0
rho0 (X)	1.0	1.0	0.8	0.6	0.6	1.4	1.4	0.8	0.512
rho0 (Y)	0.8	0.512	0.512	0.8	0.512	0.8	0.512	4.4	4.4

Table 4.5 MEAM potential parameters for the binary elemental pairs (X – Y) of Fe, Mn, Si, Al, Zn, and C with O.

	Element Pair (X – Y)					
Parameters	Fe – O	Mn – O	Si – O	Al – O	Zn – O	C – O
lattice (X,Y)	B1	B1	B1	B1	dia (B3)	B1
R_e (X,Y)	1.77864	2.223	2.2199	2.0385	2.0	1.9885
E_c (X,Y)	8.33	4.73	2.225	6.193	3.55	2.66
Alpha (X,Y)	9.7	4.6	5.4274	5.0	6.0	5.0
C^{max}_{X-X-Y}	2.8	1.6	1.164	1.2	2.8	1.2
C^{min}_{X-X-Y}	2.0	0.6	0.1	0	0	0
C^{max}_{Y-Y-X}	2.8	2.8	2.8	1.2	2.8	2.8
C^{min}_{Y-Y-X}	2.0	2.0	2.0	0	2.0	2.0
C^{max}_{X-Y-X}	2.8	2.8	2.8	2.8	2.8	2.8
C^{min}_{X-Y-X}	2.0	2.0	2.0	2.0	2.0	2.0
C^{max}_{X-Y-Y}	2.8	2.8	2.8	2.8	2.8	2.8
C^{min}_{X-Y-Y}	2.0	2.0	2.0	2.0	2.0	2.0
attrac (X,Y)	0	0	0	0	0	0
repuls (X,Y)	0	0	0	0	0	0
rho0 (X)	1.0	0.6	1.4	0.8	0.512	4.4
rho0 (Y)	7.0	7.0	7.0	7.0	7.0	7.0

4.3.2 Heat of Formation and Equilibrium Volumes

For all binary combinations, the heat of formation of at least four crystalline structures of B_1 (rock salt), B_2 (BCC equivalent), B_3 (DC equivalent), and L_{12} (FCC equivalent) were evaluated using DFT and MEAM. Table 4.6 and Table 4.7 record the heats of formation and Table 4.8 and Table 4.9 list the equilibrium volumes for the Fe, Mn, Si, Al, Zn, C, and O binary systems.

Table 4.6 The heats of formation of binary compounds of Fe, Mn, Si, C, Al, and Zn evaluated by the MEAM potential in comparison to the experimental or DFT results. The percent difference is calculated with respect to experiment when available, otherwise DFT.

Binary System	Alloy Phase	Heat of Formation, ΔH (eV/atom)			% Diff.*
		MEAM	Exp. (Lit. DFT)	DFT	
Fe – Al	B1	-0.13	-	0.37	135.1
	B2	-1.16	-0.423[a]	-0.34	174.2
	B3	0.87	-	1.19	26.9
	Fe_3Al_8	-0.32	(-0.353)[b]	-0.343	9.3
	$D0_3$	-0.33	-0.321[a]	-0.26	2.8
	L12 (Fe_3Al)	-0.38	-	-0.21	81.0
Fe – Zn	B1	0.55	-	0.55	0.0
	B2	0.12	-	0.11	9.1
	B3	2.00	-	1.29	55.0
	L12 (Fe_3Zn)	0.02	-	0.01	100.0
Al – Zn	B1	0.76	-	0.28	171.4
	B2	0.20	-	0.12	66.7
	B3	0.99	-	0.62	59.7
	L12 (Al_3Zn)	-0.01	-	0.03	133.3
Mn – Al	B1	0.20	-	0.40	50.0
	B2	-0.26	-	-0.05	420.0
	B3	1.26	-	1.26	0.0
	tP4	-0.29	(-0.255)[c]	-0.24	13.7
	$MnAl_6$	0.01	(-0.181)[c]	-0.17	105.5
	L12 (Mn_3Al)	0.08	-	-0.01	900.0
Mn – Zn	B1	0.42	-	0.55	23.6
	B2	0.12	-	0.06	100.0
	B3	1.17	-	1.16	0.9
	L12 (Mn_3Zn)	0.60	-	0.32	87.5
Si – Al	B1	0.15	-	0.28	46.4
	B2	0.07	-	0.26	73.1
	B3	1.36	-	0.41	231.7
	L12 (Si_3Al)	0.41	-	0.36	13.9

* Absolute value listed for % Difference

[a] [136]

[b] [137,138]

[c] [139]

Table 4.6 (continued)

Si – Zn	B1	0.43	-	0.42	2.4
	B2	0.54	-	0.43	25.6
	B3	1.68	-	0.64	162.5
	L12 (Si_3Zn)	0.60	-	0.46	30.4
Al – C	B1	0.37	-	0.42	11.9
	B2	0.45	-	1.25	64.0
	B3	0.45	-	0.56	19.6
	Al_4C_3	-0.15	-0.19[d]	-0.15	21.1
	L12 (Al_3C)	0.92	-	0.98	6.1
Zn – C	B1	1.64	-	1.58	3.8
	B2	1.83	-	1.85	1.1
	B3	2.40	-	1.62	48.1
	L12 (Zn_3C)	1.22	-	1.00	22.0

[d] [140]

Table 4.7 Enthalpies (heat) of formation of the binary oxide compounds for Mn, Si, Al, and Zn. Results obtained by the MEAM potential are compared with experimental observations or DFT values to compute percentage difference.

Binary System	Alloy Phase	Heat of Formation, ΔH (eV/atom)			
		MEAM	Exp.	DFT	% Diff.*
Mn – O	B1	-1.99	-1.99[a]	-1.25	0.0
	B2	-0.87	-	-0.27	222.2
	B3	-1.94	-	-0.86	125.6
	Mn_2O_3	-1.31	-1.98[a]	-1.63	33.8
	Mn_3O_4	-1.47	-2.05[a]	-1.64	28.3
	L12 (Fe_3O)	-1.35	-	0.67	301.5
Si – O	B1	1.37	-	-0.35	491.4
	B2	0.96	-	-0.02	4900.0
	B3	-2.62	-	-0.34	670.6
	α – Quartz	-3.157	-3.15[a], -3.2[b]	-2.79	0.2
	β – Quartz	-3.155	-3.14[c]	-2.78	0.5
	Tridymite	-3.153	-	-2.81	12.2
	L12 (Al_3O)	1.40	-	0.48	191.7
Al – O	B1	-3.22	-	-1.22	163.9
	B2	-3.81	-	-0.69	452.2
	B3	-3.16	-	-1.71	84.8
	Al_2O_3	-3.21	-3.47[a]	-3.03	7.5
	L12 (Al_3O)	-0.63	-	0.08	887.5
Zn – O	B1	-2.01	-	-1.31	53.4
	B2	-2.24	-	-0.74	202.7
	B3	-1.73	-	-1.45	19.3
	ZnO	-1.73	-1.81[a]	-1.38	4.4
	L12 (Zn_3O)	-0.65	-	0.03	2266.7

* Absolute value listed for % Difference

[a] [141]

[b] Experimental observations listed by Lee *et al*. [142]

[c] [143]

Table 4.8 The equilibrium volume for binary compounds of Fe, Mn, Si, C, Al, and Zn evaluated by the MEAM potential in comparison to the experimental or DFT results. The percent difference is calculated with respect to experiment when available, otherwise DFT

Binary System	Alloy Phase	Equilibrium Volume, V (Å^3)			
		MEAM	Exp. (Lit. DFT)	DFT	% Diff.*
Fe – Al	B1	117.2	-	118.4	1.0
	B2	23.8	24.5[a]	23.7	2.9
	B3	158.9	-	174.9	9.1
	Fe_3Al_8	636.1	(602.3)[b]	602.5	5.6
	$D0_3$	184.1	193.1[a]	188.1	4.7
	L12 (Fe_3Al)	48.5	-	48.6	0.2
Fe – Zn	B1	119.2	-	119.2	0.0
	B2	23.6	-	25.4	7.1
	B3	223.9	-	170	31.7
	L12 (Fe_3Zn)	49.3	-	48.7	1.2
Al – Zn	B1	168.3	-	150.1	12.1
	B2	34.9	-	32.7	6.7
	B3	351.5	-	201	74.9
	L12 (Al_3Zn)	65.2	-	65.2	0.0
Mn – Al	B1	125	-	125	0.0
	B2	32.8	-	25.8	27.1
	B3	259.3	-	194	33.7
	tP4	61.7	58.6[c]	53.8	5.3
	$MnAl_6$	483.7	435.6[d]	429	11.0
	L12 (Mn_3Al)	63.4	-	49	29.4
Mn – Zn	B1	137.4	-	130.6	5.2
	B2	27.5	-	27.5	0.0
	B3	333.8	-	195.8	70.5
	L12 (Mn_3Zn)	64.4	-	45.6	41.2
Si – Al	B1	149	-	142.3	4.7
	B2	31.6	-	31.6	0.0
	B3	220.8	-	189.1	16.8
	L12 (Si_3Al)	81.1	-	59.5	36.3

* Absolute value listed for % Difference

[a] [125]

[b] [137,138]

[c] [139]

[d] [144,145]

Table 4.8 (continued)

Si – Zn	B1	136.2	-	136.2	0.0
	B2	30.6	-	31.9	4.1
	B3	384	-	174.9	119.6
	L12 (Si_3Zn)	68.7	-	60.5	13.6
Al – C	B1	76.3	-	77.8	1.9
	B2	17.5	-	19.6	10.7
	B3	97.7	-	100.9	3.2
	Al_4C_3	253.2	277.7[e]	282.6	8.8
	L12 (Al_3C)	54.4	-	55.7	2.3
Zn – C	B1	88.2	-	85.2	3.5
	B2	18.8	-	21	10.5
	B3	251	-	103	143.7
	L12 (Zn_3C)	45.5	-	51.1	11.0

[e] [146]

Table 4.9 Equilibrium volume for the binary oxide compounds for Mn, Si, Al, and Zn. Results obtained by the MEAM potential are compared with experimental observations or DFT values to compute percentage difference.

Binary System	Alloy Phase	Equilibrium Volume, V (Å^3)			
		MEAM	Exp.	DFT	% Diff.*
Mn – O	B1	87.9	87.8[a]	87.88	0.1
	B2	18.7	-	16.45	13.7
	B3	130.8	-	82.43	58.7
	Mn_2O_3	1045.7	833.5[b]	857.3	25.5
	Mn_3O_4	393.1	314.2[c]	319.3	25.1
	L12 (Fe_3O)	44.4	-	40.64	9.3
Si – O	B1	87.5	-	98.42	11.1
	B2	16.7	-	22.12	24.5
	B3	84.9	-	115.79	26.7
	low – Quartz	131.5	130.6[d]	136	0.7
	high – Quartz	143.6	136.4[e]	141.2	5.3
	Tridymite	237.1	210.3[b]	240	12.7
	L12 (Al_3O)	221.4	-	52.44	322.2
Al – O	B1	67.8	-	89.73	24.4
	B2	13.9	-	21.23	34.5
	B3	97.6	-	93.31	4.6
	Al_2O_3	321.5	294.2[b]	303.8	9.3
	L12 (Al_3O)	49.2	-	61.10	19.5
Zn – O	B1	63.8	-	81.80	22.0
	B2	13.8	-	19.47	29.1
	B3	96.6	-	99.38	2.8
	ZnO	55.8	55[b]	59	1.5
	L12 (Zn_3O)	42.6	-	53.84	20.9

[a] Reference 31 as cited by [147]
[b] [141]
[c] [148]
[d] [149]
[e] [150]

Capturing the thermodynamics of Fe_3Al_8, inhibition layer, was a primary objective for calibration due to a desire to capture the interfacial energy of Fe and Fe_3Al_8.

Therefore, all the binary MEAM parameters were used as input variables to ensure that the heat of formation and equilibrium volume of Fe_3Al_8 was accurately captured. Results indicate that the heat of formation and equilibrium volume of Fe_3Al_8 are within 10% of literature results. As Table 4.6 indicates, all the calibrated binaries accurately reflected the relative order of formation of binary compounds dictated by the experiment or DFT results. Additionally, a majority of the binary compounds, are within reasonable agreement of the DFT results. A few binary structures, such as the L12 and B2 of Mn – Al binary, exhibited a large percent difference due the calculation being sensitive to a small DFT value. Additionally, the equilibrium volume for all the binaries in Table 4.8 are within 42 % of the experimental or DFT results. The B3 structures, none of which are the most stable structures, were the only outliers in Table 4.8.

The Mn – O interaction was another binary pair of importance due to the formation of internal and external Mn oxides. Initially, the interaction of the O potential from Gao *et al*. [124] was incompatible with Fe, Mn, Si, Al, Zn, and C, calibrated in the present study. Therefore, the parameters for the O single element potential, in addition to the binary parameters of Mn – O, were used as input variables to calibrate the Mn oxides. The O unary MEAM parameters, once calibrated for the Mn – O pair, was compatible with the remaining elements in the present study. Table 4.7 and Table 4.9 compare the enthalpies of formation and equilibrium volumes of Mn, Si, Al, and Zn oxides with the experimental (when available) or DFT observations. A maximum deviation of 34% and 26% was observed in the heat of formation and equilibrium volume, respectively, of the experimental oxides using the MEAM potential. Since the exploratory experiment in Section 2.3 revealed manganese oxides with B1 crystalline structure, the heat of

formation and equilibrium volume of the oxide was precisely calibrated. Although the experimental structure of Zn – O binary accurately reflected the enthalpy of formation and volume, the MEAM potential could not ensure that the structure was the most stable among the equal-part hypothetical structures of B1, B2, and B3. However, maintaining the relative order of stability for the Zn oxides was not a primary calibration target, and therefore, was not explored further in this study.

4.3.3 Elastic Constants for Binary Structures

The elastic constants were computed, as cataloged in Table 4.10, to verify mechanical stability of the experimentally observed binary structures. The potentials were calibrated to ensure that the bulk modulus calculated using the MEAM potential was close to the experimental results. A comparison of the elastic constants evaluated using the MEAM potential with experiment revealed a maximum percentage difference of 210%. For the binaries that do not form experimental compounds, the elastic constants of the hypothetical structures were found in reasonable agreement with the DFT calculations. The Si – Al elastic constant exhibited a large deviation that is attributed to a small value of the shear modulus, C_{44}, causing the calculation of percent difference to be sensitive to slight variations from the target.

Table 4.10 Elastic constants computed for binary compounds of Fe, Mn, Si, Al, Zn, C, and O. Results for the elastic moduli evaluated using MEAM are compared to experimental or DFT results.

Binary System	Alloy Phase	Elastic Constants (GPa) B MEAM	B Exp. (DFT)	C′ MEAM	C′ Exp. (DFT)	C_{44} MEAM	C_{44} Exp. (DFT)	% Diff.
Fe – Al	B2	235.1	152[a]	147.4	43[a]	186.9	127[a]	115
	D03	195.4	144[b]	45.2	20.2[b]	130.2	131.7[b]	53.5
	Fe_3Al_8	132	-	65.9	-	77.2	-	-
Fe – Zn	L12	130.8	(156.7)	37.2	(13)	88	(113)	74.9
Al – Zn	B2	23.4	(52.5)	9.7	(35.4)	-28.3	(-24.7)	47.5
Mn – Al	B2	66	(140)	142.6	(-24)	82.6	(80.5)	250
	$MnAl_6$	59	-	23.9	-	-45.7	-	-
Mn – Zn	B2	55	(107)	10.8	(-17.5)	34	(100)	92.1
Si – Al	B2	217	(81)	-70	(-70.6)	73.4	(-0.87)	2902
Si – Zn	B1	75	(203)	-168	(-34)	-53	(-56)	154
Al – C	Al_4C_3	159.3	(170)[c]	296.3	(146)[c]	111.3	(118)[c]	38
Zn – C	B1	112.9	(138.7)	224.5	(58)	399	(207)	132
Mn – O	B1	162	159[d]	307	61[d]	50.1	55.1[d]	138
	Mn_2O_3	103.4	-	98.9	-	145.8	-	-
	Mn_3O_4	95.7	137[e]	109.8	-	107.4	-	30.1
Si – O[x]	low-Quartz	55	37.9[f]	208	41.4[f]	216	58.2[f]	210
Al – O[y]	Al_2O_3	226	252[f]	232	184.5[f]	279	147.4[f]	41.8
Zn – O	ZnO	197	143.7[f]	92.6	49.9[f]	66.8[z]	42.5[f,z]	76.1

% Difference calculated by averaging the percentage difference of B, C′, and C_{44} w.r.t. experimental or literature results.

[a] [151]
[b] [152]
[c] [153]
[d] [154]
[e] Reference 17 as cited by Darul *et al*. [155]
[f] [141]
[x] C_{14} = 73 from MEAM; C_{14} = 73 from literature [141]
[y] C_{14} = -52.5 from MEAM; C_{14} = -23.4 from literature [141]
[z] Value listed for C_{55}

4.3.4 Substitutional and Interstitial Formation Energies

The substitutional point defect formation energies are evaluated for Fe, Mn, Si, C, Al, and Zn. For the DFT calculations, the bulk dimensions were 4 × 4 × 4 primitive cell, 3 × 3 × 3 primitive cell, 4 × 4 × 4 primitive cell, 4 × 4 × 4 primitive cell, 3 × 3 × 3 primitive cell, and 4 × 2 × 2 orthogonal HCP cell for BCC (Fe), FCC (Mn), DC (Si), DC (C), FCC (Al), and HCP (Zn). Similarly, MEAM incorporated bulk dimensions of 5 × 5 × 5 primitive cell, 4 × 4 × 4 primitive cell, 5 × 5 × 5 primitive cell, 5 × 5 × 5 primitive cell, 4 × 4 × 4 primitive cell, and 8 × 4 × 4 orthogonal HCP cell for Fe, Mn, Si, C, Al, and Zn.

Table 4.11 Substitutional point defect formation energies calculated for Fe, Mn, Si, C, Al, and Zn. Results obtained by the MEAM potential, presented without parentheses, are compared to DFT values are reported within parentheses.

	Substitutional 'Atom' Energy (eV)					
Host Atom	Fe	Mn	Si	C	Al	Zn
Fe		0.057[a] (0.057)[b]	-1.286 (-1.28)	1.02 (2.95)	-4.69 (-0.9)	0.14 (0.14)
Mn*	10.4 (0.25)		22.6 (-0.98)	2.03 (2.54)	-0.49 (-0.26)	4.43 (0.73)
Si	2.80 (1.92)	10.8 (2.67)		12.7 (1.4)	8.42 (0.93)	10.6 (1.77)
C	8.64 (6.03)	5.25 (7.26)	17.1 (4.0)		27.7 (7.39)	41.7 (9.6)
Al	-1.79 (-0.9)	-1.2 (0.3)	1.13 (1.05)	-2.86 (4.47)		0.81 (0.81)
Zn	0.66 (0.66)	0.82 (1.06)	0.78 (1.11)	4.40 (4.39)	0.76 (0.26)	

[a] Results produced by MEAM.
[b] DFT results in parenthesis.
* FCC used as bulk crystalline structure.

Table 4.11 compares the point defect formation energies of a single type-Y impurity atom in the bulk of type-X atoms evaluated by the MEAM potential in comparison to DFT results depicted within parentheses. Results indicated that a majority of the substitutional energies were in good agreement with the DFT results. Although the substitutional energy of Al in Fe bulk exhibited significant error, the point defect formation energy was not a primary calibration objective for the Fe – Al binary system. Similarly, Al and Zn in the bulks of Si and C exhibited large deviation from DFT target values.

Oxygen does not form complex oxide compounds with Fe during the galvanization process but rather diffuses within the steel bulk. Therefore, the solubility of O in Fe bulk is an important calibration objective. Since oxygen is similar in size to carbon, the interstitial formation energy of O in Fe bulk was evaluated. DFT predicted a lower interstitial formation energy of -0.77 eV versus a substitutional formation energy of 1.07 eV, indicating the affinity of oxygen to alloy as an interstitial rather than a substitution. The MEAM parameters of Fe – O accurately replicated the relative order of formation trend dictated by DFT. The interstitial formation energy was computed as -0.78 eV whereas the substitutional formation energy was 0.98 eV.

4.4 Preliminary Validation Testing

As established by the exploratory experiments conducted in Chapter 2, the primary interfaces that form during the galvanizing process are between Fe, inhibition layer, and Mn oxides. Therefore, evaluating the interfacial energies of the aforementioned interfaces is imperative to improve our understanding of the thermodynamics involved during the galvanizing process.

The interface between Fe and Fe_3Al_8 was studied using molecular dynamics in LAMMPS. To simulate the bulk structure with an interface, a large box, with dimensions of 235.137Å × 395.893Å × 83.105Å, was setup to contain Fe and Fe_3Al_8. The interface was in the X – Z plane and the dimensions were chosen such that the mismatch of bulk lattices of Fe and Fe_3Al_8 was less than 0.1 Å. The length in the z – direction was sufficiently large to ensure that the strain caused at the interface would not affect the structure in the center of each bulk layer. Initially, the structure was relaxed and then equilibrated using the NPT ensemble for 50 ps to achieve zero-pressure volume at 723K, which is also the approximate formation temperature of the inhibition layer in the Zn bath. A final equilibration was conducted using NVT ensemble for 50 ps. During the equilibration, the energy of the strained system was computed by averaging the total energy over 40 ps. At the same time, the energy of the reference states of Fe and Fe_3Al_8 was calculated. The average energies per atom for each type were evaluated in three regions of equal volume far from the interface, schematically illustrated in Figure 4.3. For the bulk representing pure Fe, the energy per atom was an average over the three regions. However, the energy per atom per compound of the Fe_3Al_8 layer, $E_{Fe_3Al_8}$, was computed by the following equation

$$E_{Fe_3Al_8} = [3 * E^*_{Fe} + 8 * E^*_{Al}]/11 \tag{4.1}$$

where E^*_{Fe} and E^*_{Al} denote the energy per atom of Fe and Al, respectively, in the bulk of Fe_3Al_8. Finally, the interfacial energy, E_{Intf}, was obtained from the following equation

$$E_{Intf} = \left[E_{Fe/Fe_3Al_8} - \left(E_{Fe} * N_{Fe} + E_{Fe_3Al_8} * N_{Fe_3Al_8}\right)\right]/2A \tag{4.2}$$

where E_{Fe/Fe_3Al_8} represents the total energy of the strained system with an interface between Fe and Fe_3Al_8, E_{Fe} is the energy per atom of the reference structure of Fe bulk,

A represents the area of the interface, and N_{Fe} and $N_{Fe_3Al_8}$ are the total number of atoms in the bulk of Fe and inhibition layer, respectively.

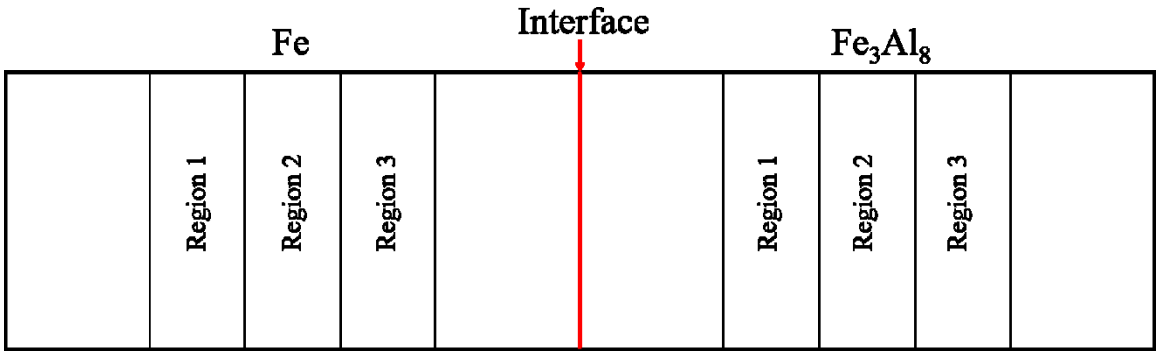

Figure 4.3 A schematic of the interface between two bulk structures (Fe and Fe_3Al_8).

The interfacial energy was computed as -3200 mJ/m^2 at 723 K for the interfaces of Fe (010) and Fe_3Al_8 (010). A negative sign denotes an exothermic or highly favorable interfacial interaction between the two phases. Figure 4.4 and Figure 4.5 illustrate a thin slice of the interface in the X – Y and Z – Y plane, respectively, with the initial and final (equilibrated) configurations. The interface, studied using OVITO [156] visualization software, appears with negligible degradation or phase change after the equilibration.

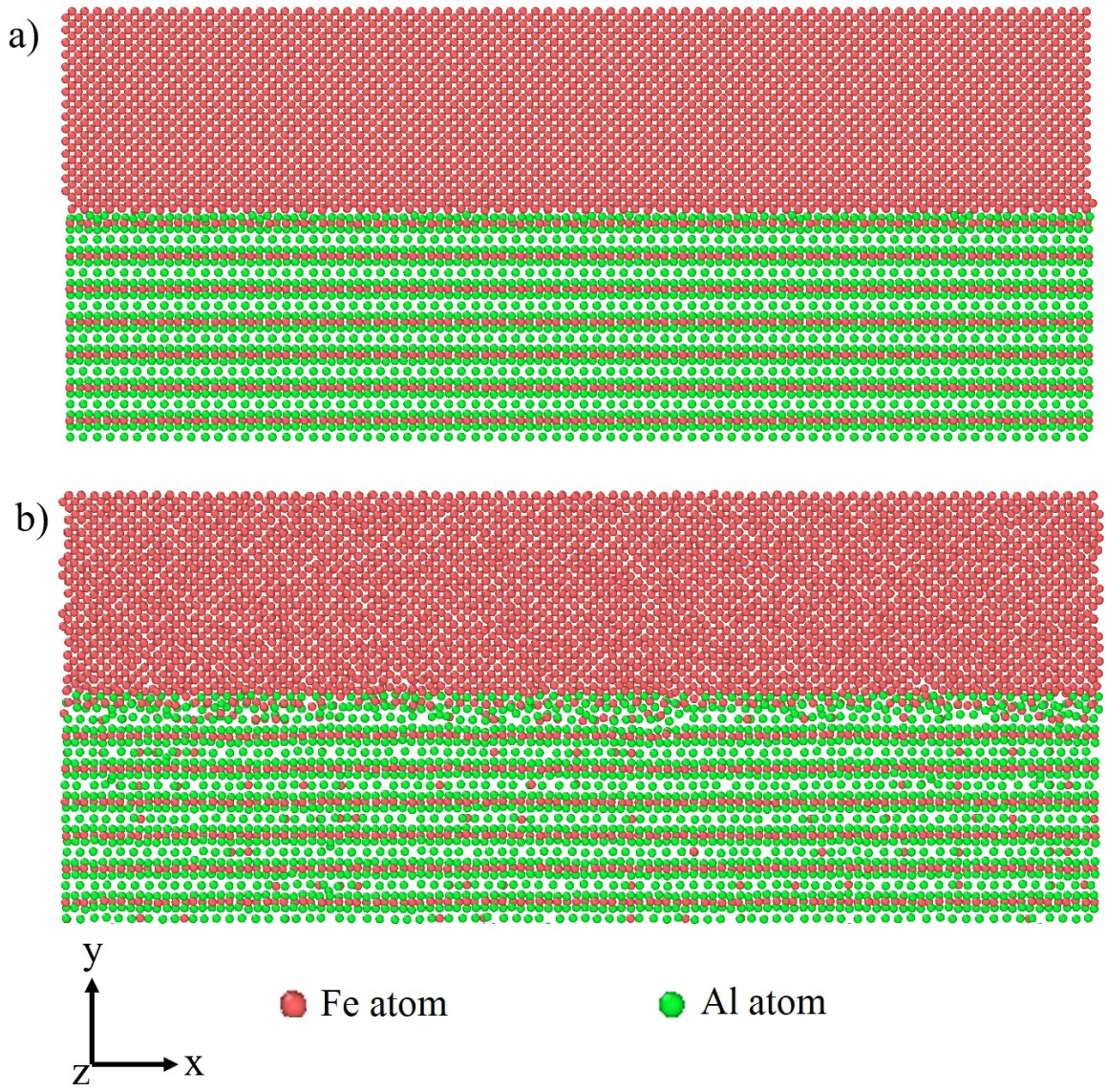

Figure 4.4 A thin slice of the Fe – Fe_3Al_8 interface in the X – Y plane with a) initial configuration and b) final configuration at 723K.

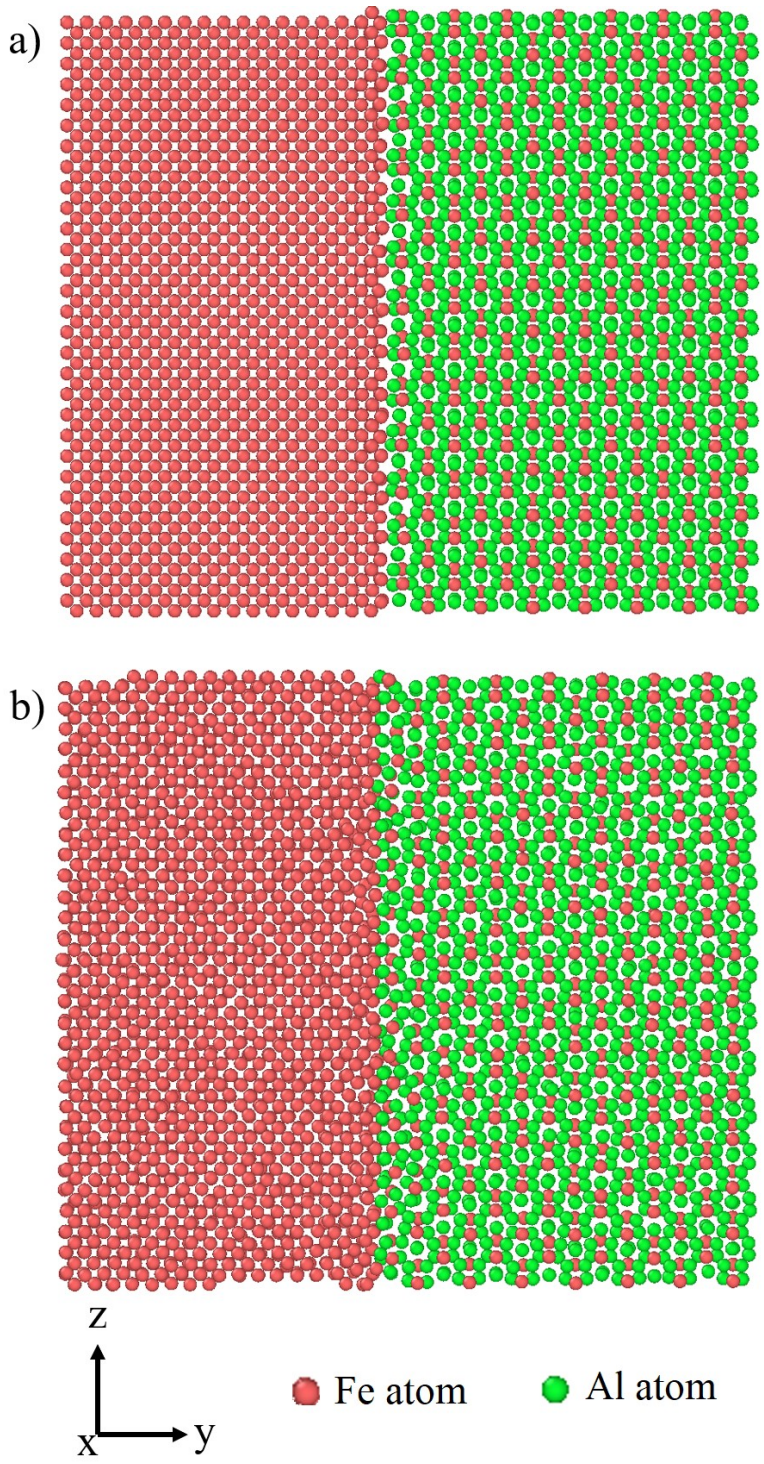

Figure 4.5 Screenshot of the a) initial and b) final configuration of the Fe – inhibition layer interface in the Y – Z plane at 723 K.

4.5 Conclusions

A seven-element MEAM potential, attempted for the first time, including Fe, Mn, Si, Al, Zn, C, and O was developed to encapsulate the inhibition layer and oxide formation during galvanization of low-alloy steels. Experimental and *ab-initio* calculations of cohesive energy, lattice parameters, elastic constants, vacancy formation energy, interstitial formation energy, and surface formation energies were used as single element MEAM potential calibration objectives. Similarly, the heat of formation, elastic constants, substitutional formation energy, and interstitial formation energy provided data to calibrate binary element pairs. Accurate representation of the Fe_3Al_8 inhibition layer and Mn oxides was imperative to comprehend their interaction of low-alloy steels. Preliminary validation testing reveals that the interfacial energies involved between the Fe – Fe_3Al_8 is thermodynamically favorable at approximately 723K.

4.6 Acknowledgements

This work was funded by the National Science Foundation (NSF) under contract number 1506878**.** The authors would also like to thank the Center for Advanced Vehicular Systems (CAVS) at Mississippi State University for supporting this work.

CHAPTER V

A SENSITIVITY AND UNCERTAINTY ANALYSIS OF A BINARY MODIFIED EMBEDDED ATOM METHOD (MEAM) POTENTIAL: FE-SI EXAMPLE

5.1 Introduction

Uncertainties are associated with all aspects of engineering. Experimental uncertainty can arise due to variation in setup, error in equipment and sensors, and disparity in environmental effects. Similarly, there are errors inherent to the application of a computational model to capture a complex, multi-dimensional physical phenomenon, owing to various mathematical approximations and simplifications. The accuracy of an experiment is only as good as the uncertainty associated with the results, particularly when these results are used to further inform a predictive model to capture material response at subsequent length or time scales. If the relevant uncertainty is not captured and propagated, then the computational errors amassed during each intermediate upscaling step may be amplified to negatively impact that the fidelity of the model.

In addition to experimental errors, computational modeling can have its own sources of uncertainties. Beyond the errors customarily associated with truncation and discretization, this study accounts for uncertainties incorporated due to bounds that must be enforced upon certain calibration parameters for the model to be physically admissible. Intuitively, the bounds of uncertainty should widen during length scale

propagation. However, the interplay of phenomena at adjacent length scales may lead to the uncertainty at a lower scale being entirely smeared out at the higher length scales. Such an outcome may be encountered if a certain parameter shows a high sensitivity on the results at a lower length scale, with the parameter sensitivity diminishing as the results are propagated forward. This is especially true if the phenomena controlled by the parameter do not have a strong bearing on the overall downscaling requirement of the multiscale modeling approach.

Experimental observations provide the primary calibration objectives. Computational methods are validated if they lie within the bounds of experimental uncertainty and verified if the computational method is in agreement with other models. The semi-empirical MEAM potential, used in the present study, has been employed extensively to calibrate and model atomistic length scale phenomenon. Hughes *et al*. [157] studied the parameter sensitivities and uncertainties associated with a single element calibration of Al. Tschopp *et al*. [158] explored the sensitivity and uncertainty of saturated hydrocarbons based on the recently developed Modified Embedded Atom Method with Bond Order (MEAM – BO) [100] formulation. While sensitivity and uncertainty can be investigated through various methods, this study employs a one-factor-at-a-time (OFAT) perturbation method to carry over uncertainty distributions in equilibrium parameters, elastic constants, and dilute solution energies of an Fe-Si binary system.

5.2 Sensitivity and Uncertainty Methodology

The relative sensitivity analysis, S_{R,N_j}, of the MEAM parameters was conducted using a one-factor-at-a-time perturbation methodology and is described by the following equation

$$S_{R,N_j} = \frac{a_{j,0}}{R_0}\left[\frac{R(a_{j,0}+\Delta\alpha_j)-R(a_{j,0}-\Delta\alpha_j)}{2\Delta\alpha_j}\right] \quad (5.1)$$

where $a_{j,0}$ indicates the value of an input parameter, R_0 represents the result based on the input parameters $a_{j,0}$, $\Delta\alpha_j$ is the perturbation size of the input parameter, and $R(a_{j,0} \pm \Delta\alpha_j)$ specifies the output response to perturbations of the input variables. The units of S_{R,N_j} are in %/%, where S_{R,N_j} of 5 translates to a change in the input variable, $a_{j,0}$, by 1% results in a change of the response variable, R_0, by 5%. The current study will present the magnitude of S_{R,N_j}.

Total uncertainties, U_f, and uncertainty percent contributions, *UPCs*, due to input parameter are computed as follows:

$$\frac{\delta f}{\delta\alpha_j} = \frac{R(a_{j,0}+\alpha_j)-R(a_{j,0}-\alpha_j)}{2\Delta\alpha_j} \quad (5.2)$$

where the model sensitivity, $\frac{\delta f}{\delta\alpha_j}$, denotes the relative change in response variable, R, with respect to the input variable α_j. Ignoring the covariance terms, the total propagated uncertainty, U_f, is then simply represented by the square root of the sum of the square of model sensitivities for all input variables.

$$U_f^2 = \sum_{j=1}^{n}\left(\frac{\delta f}{\delta\alpha_j}\right)^2\left(U_{\alpha_j}\right)^2 \quad (5.3)$$

where U_{α_j} is the uncertainty associated with an input parameter, which was estimated to be within 95% of the normal distribution confidence intervals. The uncertainty contributed due to each input parameter, *UPC*, is evaluated by normalizing the model sensitivity due to each parameter by the total propagated uncertainty as follows

$$UPC = \frac{\left(\frac{\delta f}{\delta \alpha_j}\right)^2 \left(U_{\alpha_j}\right)^2}{U_f^2} * 100 \tag{5.4}$$

5.3 Results and Discussion

In the current study, fourteen input binary parameters were analyzed and a perturbation size of 1% about the base parameter was employed for all given parameters. The perturbation size was chosen such that a nearly perfect linear correlation coefficient was obtained. In addition, since relative sensitivity requires a nonzero input parameter, the value of MEAM parameter 'attrac' was modified from the original value of 0 to 0.01. The sensitivities and uncertainties were garnered for twenty different material properties of the Fe – Si binary system: six heats of formation of B1, B2, B3, B20, L12, and D03 binary structures; six equilibrium volumes of B1, B2, B3, B20, L12, and D03 binary structures; six elastic constants of B20 and D03 experimentally observed binary structures; two dilute solution energies. Lastly, two types were used to describe parameters contributing to the sensitivities and uncertainties for the material properties: primary and secondary. The primary parameters yielded the most to the sensitivities or uncertainties while secondary parameters caused relatively small changes from the ideal output.

5.3.1 Binary Heat of Formation

Figure 5.1a and Figure 5.1b illustrates the sensitivity and uncertainty, respectively, for the six binary compounds. The reference structure used for the Fe – Si binary was B1 and based on equilibrium pair-potential defined by the Rose equation (Appendix Equation B.24), the cohesive energy, E_c, is the only parameter that can change the energy of the reference structure. As a result, E_c is the only sensitivity parameter and completely contributed to the uncertainty in the results for B1 heat of formation. For the remaining five binary heats of formation, the equilibrium distance, R_e, and E_c were the primary sensitivity parameters whereas the exponential decay factor, alpha, and relative background electron density, rho0, were the secondary sensitivity parameters. In terms of uncertainty contribution, the parameters did not exhibit the same trend as sensitivity analysis. R_e was the primary parameter while E_c and rho0 were the secondary parameters contributing to uncertainty for B2, B3, L12, and D03. B20 was the only other binary structure, other than B1 reference structure, whose uncertainty was primarily produced by E_c while R_e and rho0 were secondary uncertainty percent contribution parameters. Although alpha was a secondary sensitivity parameter for a majority of the binary structures, the parameter had negligible contribution to uncertainty. B3 was the only binary structure that was slightly sensitive to repuls, the cubic repulsive term in the universal equation of state. Consequently, repuls was used as an input parameter to ensure that B3 was not the most stable structure among equal-part stoichiometric binary structures. The total MEAM uncertainty, U_f, in heat of formation for the six binary structures is listed in Table 5.1.

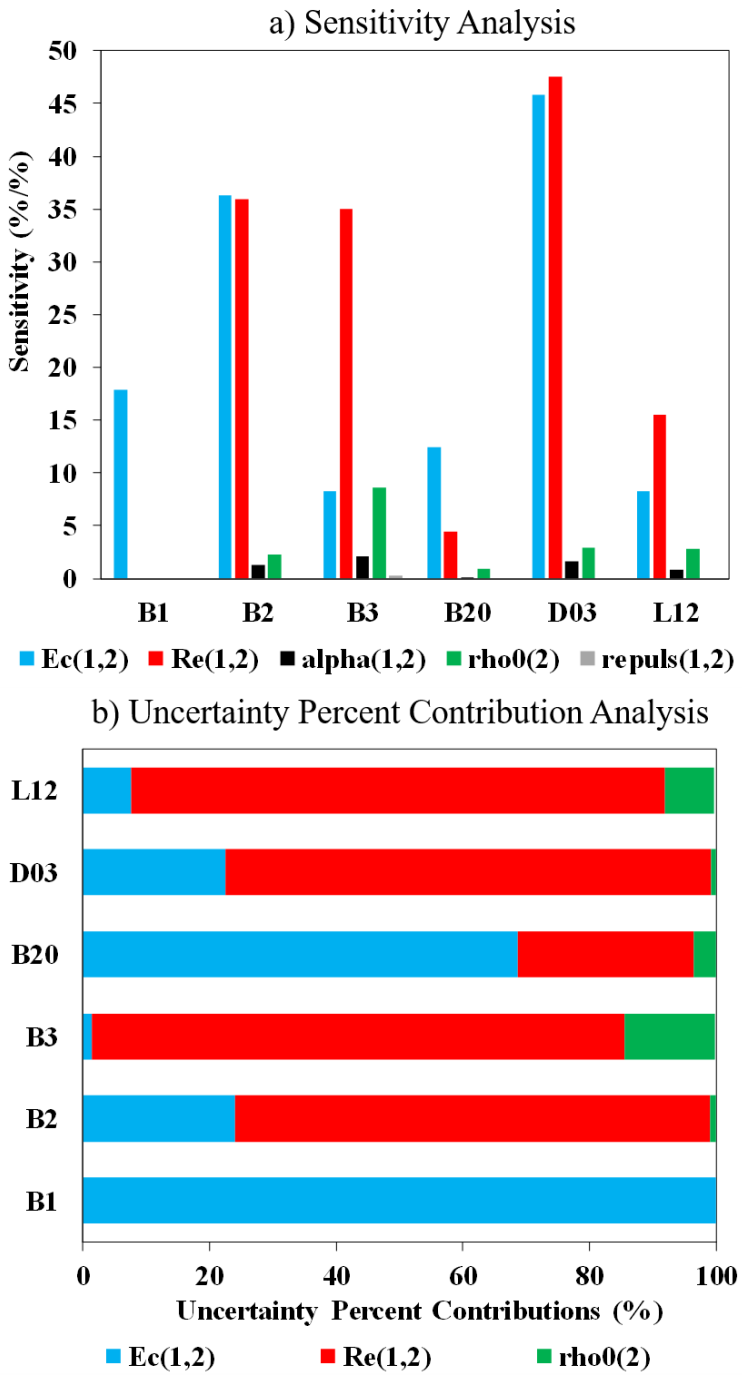

Figure 5.1 a) Sensitivity analysis and b) uncertainty percent contributions evaluated for the heat of formation of B1, B2, B3, B20, L12, and D03 structures of Fe – Si binary.

The energy of the binary structures is highly sensitive to E_c and R_e, and contribute the most towards the total uncertainty. Rho0 and alpha are secondary sensitivity parameters whereas only Rho0 contributes to any significant uncertainty in results.

Table 5.1 Total uncertainty in the heat of formation of binary Fe – Si compounds computed using the MEAM potential.

Properties	Exp. (DFT)	MEAM	% Difference	MEAM Uncertainty
B1 (eV/atom)	(0.25)	0.24	4	± 0.05
B2 (eV/atom)	(-0.48)	-0.16	67	± 0.13
B3 (eV/atom)	(0.71)	-0.31	143	± 0.25
B20 (eV/atom)	-0.41	-0.40	2.4	± 0.07
D03 (eV/atom)	-0.21	0.06	274	± 0.07
L12 (eV/atom)	(-0.27)	0.47	129	± 0.17

5.3.2 Equilibrium Volume

The results for sensitivity and uncertainty percent contribution analysis of the binary equilibrium volumes are depicted by Figure 5.2a and Figure 5.2b, respectively. Dictated by the universal equation of state and behaving in a similar fashion as the aforementioned section, the equilibrium distance, R_e, was the only parameter that affected the equilibrium volume of the reference structure B1. However, in stark contrast to the previous section, R_e was the only primary sensitivity parameter and attributed the most to uncertainty for all binary structures. The calibration parameters of E_c, alpha, rho0, and repuls were secondary parameters that impacted sensitivity whereas alpha, rho0, and attract were secondary parameters that contributed to uncertainty. Table 5.2 presents the overall uncertainty in equilibrium volumes for the six binary structures obtained using the calibrated MEAM potential.

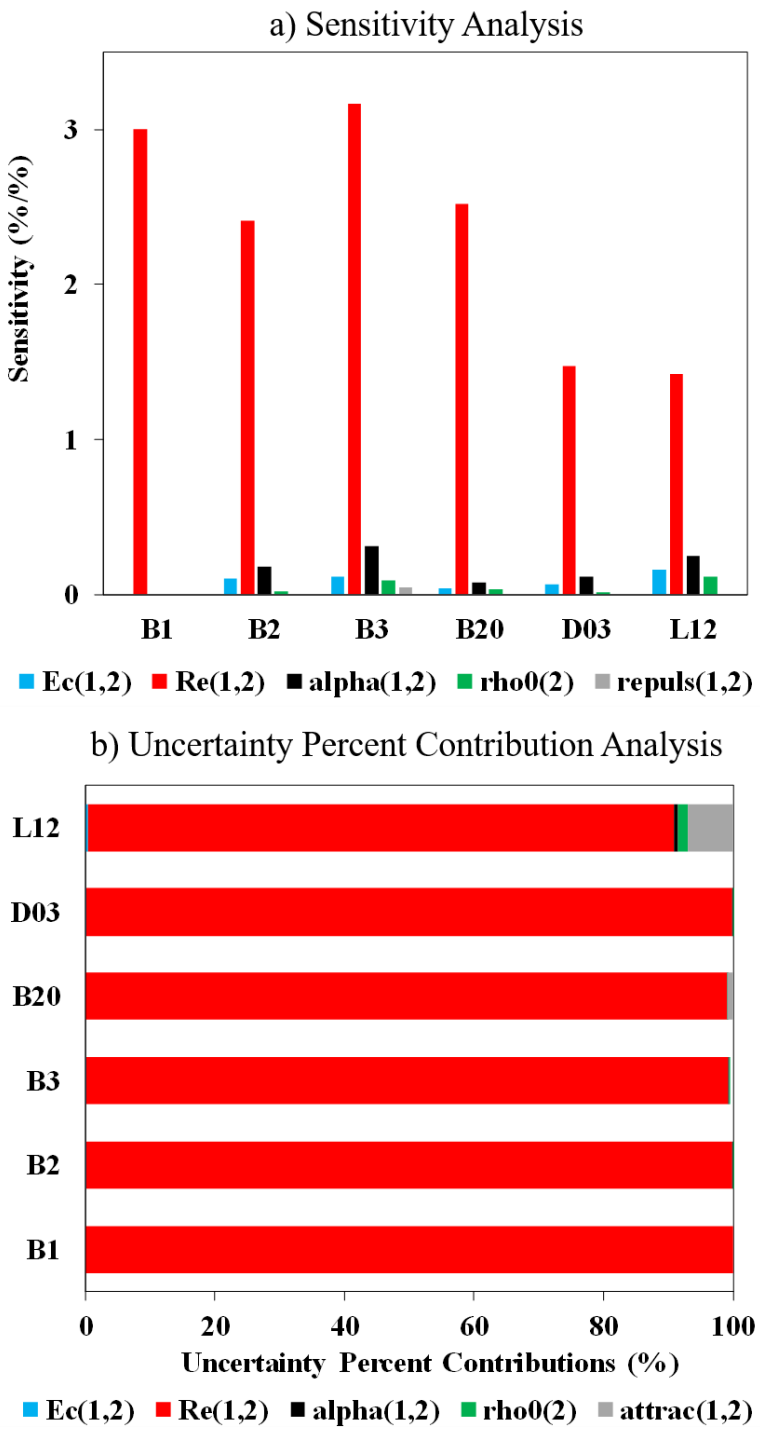

Figure 5.2 Analysis of a) sensitivity and b) uncertainty contributions for the equilibrium volumes of B1, B2, B3, B20, L12, and D03 structures.

The equilibrium volumes of all binary parameters are highly sensitive to R_e and yield the most uncertainty whereas E_c, alpha, and rho0 are secondary sensitivity and uncertainty parameters.

Table 5.2 Total uncertainty in equilibrium volume of binary Fe – Si compounds using the calibrated MEAM potential.

Properties	Exp. (DFT)	MEAM	% Difference	MEAM Uncertainty
B1 ($Å^3$)	(104.5)	106.5	1.9	± 6.7
B2 ($Å^3$)	(21.1)	22.8	8.0	± 1.2
B3 ($Å^3$)	(140.6)	137.4	2.3	± 9.2
B20 ($Å^3$)	89.9	90.1	0.2	± 4.8
D03 ($Å^3$)	180.3	1832	1.6	± 5.7
L12 ($Å^3$)	(45.9)	47	2.4	± 1.5

5.3.3 Elastic Constants

The elastic constants for B20 were affected by the most number of calibration parameters, as visualized in Figure 5.3a. Although the bulk modulus is directly related to alpha input parameter, the primary sensitivity and uncertainty contribution parameter for a majority of the bulk moduli was the equilibrium distance, R_e, with the exception of shear modulus, C_{44}, of B20 binary structure. However, alpha was a secondary sensitivity parameter for all elastic constants. In addition, E_c, rho0, and screening parameters, C_{min}-(1,1,2) and C_{max}(1,1,2) were secondary sensitivity parameters for elastic constants for B20. The uncertainty contributions exhibited a slightly different trend. The screening term, C_{max}(1,1,2) was a primary uncertainty percent contribution parameter for shear modulus, C_{44}, of B20 binary structure. For the remaining elastic constants, R_e produced the most uncertainty in results while rho0, C_{min}(1,1,2), C_{max}(1,1,2), and attract yielded less uncertainty. Table 5.3 details the maximum uncertainty in the elastic constants of

B20 and D03 experimentally observed binary structures. The bulk modulus for both structures exhibited maximum uncertainty in comparison to the shear moduli.

Table 5.3 Estimated uncertainty in elastic moduli of B20 and D03 experimentally observed structures based on the MEAM potential.

Properties (GPa)	Exp. (DFT)	MEAM	% Difference	MEAM Uncertainty
B20 (B)	110	78.7	28.5	± 69.5
B20 (C′)	(150)	22.3	85.1	± 14.1
B20 (C_{44})	(180)	57.7	67.9	± 7.0
D03 (B)	168	266.2	58.5	± 35.9
D03 (C′)	38	103.4	171.1	± 8.0
D03 (C_{44})	137	124.7	9.0	± 14.0

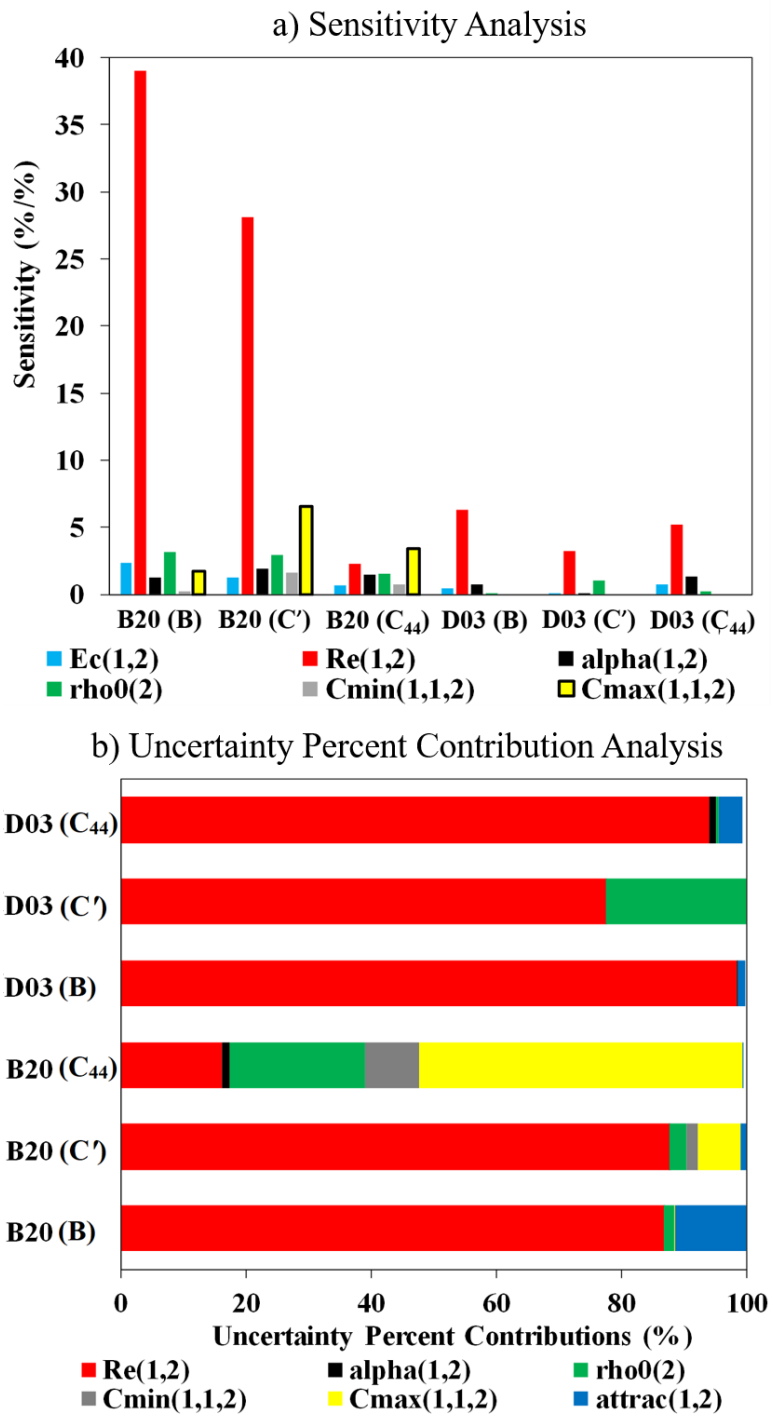

Figure 5.3 a) Sensitivity and b) Uncertainty percent contribution analysis for the elastic constants of B20 and D03 experimentally observed binary structures.

R_e is a primary sensitivity and uncertainty parameter with E_c, rho0, alpha, $C_{min}(1,1,2)$, and C_{max} (1,1,2) as secondary sensitivity and uncertainty parameters.

5.3.4 Dilute Solution Energies (Substitutional Formation Energies)

Figure 5.4a and Figure 5.4b portray the sensitivities and uncertainties, respectively, contributed by MEAM parameters on the substitutional formation energies. The primary sensitivity parameter for Si in Fe bulk was the cohesive energy of the pair potential, E_c, whereas the equilibrium distance, R_e, and relative background density were secondary sensitivity parameters. The dilute solution energy of Fe in Si bulk exhibited a slightly different trend where R_e was the primary sensitivity parameter, and E_c and rho0 were revealed as secondary sensitivity parameters. If accurately capturing the binary compounds is an objective, then rho0 becomes the key parameter to accurately calibrate the dilute solution energy of Si in Fe, which is another primary calibration target. In terms of contribution to uncertainty, the parameters replicated the trend observed for sensitivity analysis. Lastly, both dilute solution energies exhibited minor sensitivity to the alpha parameter but dispensed negligible effect on the uncertainty analysis. Table 5.4 presents the total uncertainty in the results for substitutional formation energies obtained using the MEAM potential.

Table 5.4 Computed total uncertainties in the MEAM potential calibration of substitutional formation energies

Properties	DFT (eV)	MEAM (eV)	% Difference	MEAM Uncertainty (eV)
Si in Fe bulk	-1.286	-1.286	0	± 0.165
Fe in Si bulk	1.92	2.80	45.8	± 0.346

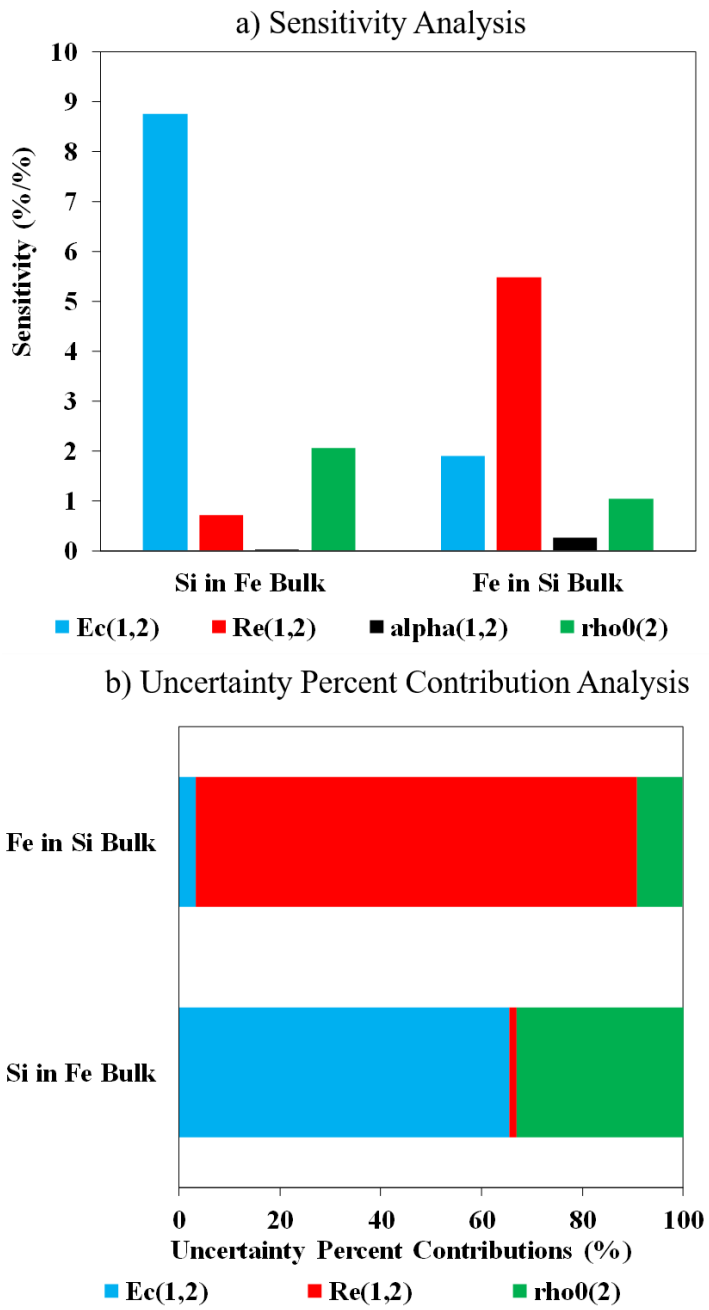

Figure 5.4 Analysis performed on substitutional formation energies of Si in Fe bulk and Fe in Si bulk to evaluate the a) sensitivity and b) uncertainty percent contributions.

The formation energy of Si in Fe bulk is highly sensitive to E_c with rho0 and R_e as secondary sensitivity parameters. However, R_e is the primary sensitivity parameter for Fe in Si bulk with E_c and rho0 as secondary parameters resulting in high sensitivity. Uncertainty percent contribution analysis replicates the trends observed in sensitivity analysis.

5.4 Conclusions

The sensitivity and uncertainty analysis were conducted to ascertain the effect of fourteen binary input parameters of the MEAM potential on twenty calibrated binary material properties. Results indicated that for the heats of formation, the primary parameters associated with sensitivity and uncertainty were the cohesive energy, E_c, and equilibrium distance, R_e, with the exception of reference structure. However, the equilibrium volumes of the binary structures dictated an intuitive trend where the equilibrium distance, R_e, had the highest impact on sensitivity and uncertainty. The sensitivity and uncertainty analysis on elastic moduli also exhibited unexpected results. Although the bulk modulus of the pair potential is directly related to the alpha parameter in the Rose equation, the equilibrium distance, R_e, was the parameter that produced the highest uncertainty and yielded most to the uncertainty in results. Finally, analysis of the dilute solution energies revealed that the equilibrium energy of the reference structure, E_c, was the primary sensitivity and uncertainty parameter for Si in Fe bulk but in the event of multiple calibration objectives, rho0 can provide the necessary drive to calibrate the substitutional formation energy.

CHAPTER VI

CONCLUSIONS

A dual-phase steel, galvanized in a Zn bath with 0.2 weight percent Al, was provided by POSCO to be studied at the nanoscale and explore the interfacial structures. Focused ion beam was used to fabricate an electron transparent specimen and transmission electron microscope was used to resolve atomic features in galvanized steels. The surface and subsurface of the steel was populated with a continuous external oxide layer and dispersed internal oxides, respectively. External oxides, having an average thickness of 20 nm, were comprised of Mn with exact stoichiometric ratio of MnO. A continuous, fully developed Fe_2Al_5/Fe_3Al_8 inhibition layer, with an average thickness of 96 nm, was present on top of the Mn oxides. The formation of the inhibition layer can be attributed Fe diffusing through the porous MnO film and short-circuit diffusion paths in oxide grains or aluminothermic reduction of Mn oxides. The interfacial structures observed on steel protected by a Zn coating provided a blueprint for multiscale modeling and design of galvanized steel alloys.

A seven-element MEAM potential involving Fe, Mn, Si, Al, Zn, C, and O was developed to simulate low-alloy steels, inhibition layer, and oxide formation during galvanization of low-alloy steels using a hierarchical multiscale modeling paradigm. The first step entails calibrating the single element potentials using experimental observations and *ab-initio* calculations, as primary and secondary calibration targets, respectively.

Calibration data included cohesive energy, lattice parameters, elastic constants, and point defect formation energies of vacancies and interstitials. Binary element calibration ensues the single element calibration where heats of formation, elastic constants, substitutional formation energies and interstitial formation energies were binary calibration targets. Finally, ternary interactions of Fe, Mn, Si, and C were considered using substitutional and interstitial binding energies that were compared to DFT calculations.

Validation testing was conducted to ascertain the applicability of the newly developed MEAM potential to garner thermodynamic, kinetic, and mechanical data. Atomistic simulations of heat capacity, thermal expansion, diffusion coefficients, and generalized stacking fault energy of low-alloy steels demonstrated good agreement with experiment and literature results. Furthermore, solid-solution strengthening mechanisms contributed by alloying elements of Mn, Si, and C were successfully verified, which extended the applicability of the calibrated MEAM potential to capture multiple aspects of low-alloy steels. Lastly, preliminary validation testing was conducted to determine the interfacial energies of Fe with Fe_3Al_8 and MnO. Results indicated that the interface between Fe – Fe_3Al_8 is thermodynamically favorable whereas the interaction between Fe – MnO is unfavorable.

Obtaining the sensitivity and uncertainty of the calibrated results was imperative. Therefore, the effect of 14 binary calibration input parameters on 20 calibration targets of the Fe – Si binary were calculated using a One-Factor-at-a-Time (OFAT) perturbation method. A majority of heat of formation of the binary compounds were primarily sensitive to equilibrium distance and cohesive energy, with the exception of the reference structure's enthalpy of formation. The equilibrium volume of the binary compounds

demonstrated a natural trend where the equilibrium distance parameter was the primary sensitivity and uncertainty parameter. The elastic constants of the experimental compounds exposed that alpha, a MEAM parameter directly related to the bulk modulus, was a secondary sensitivity and uncertainty parameter. The equilibrium distance yielded the highest sensitivity and uncertainty for the elastic moduli. Lastly, the primarily sensitivity and uncertainty parameter responsible for dilute solution energy of Si in Fe bulk and Fe in Si bulk was the cohesive energy and equilibrium distance, respectively. However, the relative background electron density parameter, rho0, was a robust secondary calibration parameter for the substitutional formation energy.

CHAPTER VII

FUTURE WORK

The next step entails conducting simulations to validate the seven-element MEAM potential. In addition, thermodynamic and kinetic properties need to be evaluated that can be upscaled to the phase-field model. A detailed description of the process is as follows:

1. Determine the binding energies of two like atoms at 1NN and 2NN locations in Fe:
    a. Use DFT to obtain the formation energies.
    b. Replicate the calculations using MEAM potential and compare against DFT results.
2. Evaluate the vacancy migration energy for Fe using MEAM and use the results to recalculate the diffusivity of Fe.
3. Determine the free energies (Gibb's free energy) for vacancy in Fe.
4. Evaluate the 1NN and 2NN ternary binding energies of
    a. Mn and Si substitutionals with O interstitial.
    b. C interstitial with O interstitial.
5. Obtain diffusivities of Mn – Si – C in Fe bulk.
6. Calculate the diffusivity of O in Fe and steel with composition of interest.

7. Obtain stress-strain curves for alloying element additions in steel to demonstrate strengthening.
8. Evaluate the interfacial energies between steel, oxides, inhibition layer, and Zn coating. In addition, introduce misorientation between interfaces to determine which interfacial orientation is the most thermodynamically favorable.
9. Perform a segregation analysis of
    a. Alloying element to the interface and how the interfacial energies change.
    b. O in steel alloy with a free surface to determine whether O tends to move to the surface.
    c. O and alloy components in the steel alloy with a free surface to determine if a surface oxide forms.
    d. Mn, Si, C, and O (independently) to the grain boundaries
    e. O in the vicinity of a dislocation core.
    f. (co-segregation analysis of) all alloying elements to grain boundaries and dislocation cores.

REFERENCES

[1] B. Mintz, Hot dip galvanising of transformation induced plasticity and other intercritically annealed steels, International Materials Reviews. 46 (2001) 169–197. doi:10.1179/095066001771048754.

[2] R. Bode, M. Meurer, T.W. Schaumann, W. Warnecke, Selection and use of coated advanced high-strength steels for automotive applications, Rev. Met. Paris. 101 (2004) 551–558. doi:10.1051/metal:2004123.

[3] X.G. Zhang, Corrosion and electrochemistry of zinc, Springer Science & Business Media, 2013.

[4] S. Prabhudev, S. Swaminathan, M. Rohwerder, Effect of oxides on the reaction kinetics during hot-dip galvanizing of high strength steels, Corrosion Science. 53 (2011) 2413–2418. doi:10.1016/j.corsci.2011.03.027.

[5] H. Liu, F. Li, W. Shi, R. Liu, L. Li, Characterization of hot-dip galvanized coating on dual phase steels, Surface and Coatings Technology. 205 (2011) 3535–3539. doi:10.1016/j.surfcoat.2010.12.028.

[6] H. Liu, Y. He, S. Swaminathan, M. Rohwerder, L. Li, Effect of dew point on the surface selective oxidation and subsurface microstructure of TRIP-aided steel, Surface and Coatings Technology. 206 (2011) 1237–1243. doi:10.1016/j.surfcoat.2011.08.038.

[7] H. Liu, F. Li, W. Shi, S. Swaminathan, Y. He, M. Rohwerder, L. Li, Challenges in hot-dip galvanizing of high strength dual phase steel: Surface selective oxidation and mechanical property degradation, Surface and Coatings Technology. 206 (2012) 3428–3436. doi:10.1016/j.surfcoat.2012.02.001.

[8] R. Khondker, A. Mertens, J.R. McDermid, Effect of annealing atmosphere on the galvanizing behavior of a dual-phase steel, Materials Science and Engineering: A. 463 (2007) 157–165. doi:10.1016/j.msea.2006.09.116.

[9] I. Cvijović, I. Parezanović, M. Spiegel, Influence of H2–N2 atmosphere composition and annealing duration on the selective surface oxidation of low-carbon steels, Corrosion Science. 48 (2006) 980–993. doi:10.1016/j.corsci.2005.02.022.

[10] G.M. Song, T. Vystavel, N. van der Pers, J.T.M. De Hosson, W.G. Sloof, Relation between microstructure and adhesion of hot dip galvanized zinc coatings on dual phase steel, Acta Materialia. 60 (2012) 2973–2981. doi:10.1016/j.actamat.2012.02.003.

[11] I. Parezanovic, M. Spiegel, Influence of dew point on the selective oxidation during annealing of cold rolled DP and Ti-IF steels, J. Corros. Sci. Engg. 6 (2003).

[12] I. Aslam, B. Li, R.L. Martens, J.R. Goodwin, H.J. Rhee, F. Goodwin, Transmission electron microscopy characterization of the interfacial structure of a galvanized dual-phase steel, Materials Characterization. 120 (2016) 63–68. doi:10.1016/j.matchar.2016.08.014.

[13] S. Alibeigi, R. Kavitha, R.J. Meguerian, J.R. McDermid, Reactive wetting of high Mn steels during continuous hot-dip galvanizing, Acta Materialia. 59 (2011) 3537–3549. doi:10.1016/j.actamat.2011.02.027.

[14] T. Kato, K. Nunome, K. Kaneko, H. Saka, Formation of the ζ phase at an interface between an Fe substrate and a molten 0.2 mass% Al–Zn during galvannealing, Acta Materialia. 48 (2000) 2257–2262. doi:10.1016/S1359-6454(00)00037-9.

[15] A.R. Marder, The metallurgy of zinc-coated steel, Progress in Materials Science. 45 (2000) 191–271. doi:10.1016/S0079-6425(98)00006-1.

[16] M. Blumenau, M. Norden, F. Friedel, K. Peters, Reactive wetting during hot-dip galvanizing of high manganese alloyed steel, Surface and Coatings Technology. 205 (2011) 3319–3327. doi:10.1016/j.surfcoat.2010.11.053.

[17] K.-K. Wang, C.-W. Hsu, L. Chang, D. Gan, K.-C. Yang, Role of Al in Zn bath on the formation of the inhibition layer during hot-dip galvanizing for a 1.2Si–1.5Mn transformation-induced plasticity steel, Applied Surface Science. 285 (2013) 458–468. doi:10.1016/j.apsusc.2013.08.077.

[18] Y. Adachi, K. Kamei, Tem study of diffusional α-Fe/Zn interface (nano-scale-characterization of galvannealed steel), Acta Metallurgica et Materialia. 43 (1995) 3189–3197. doi:10.1016/0956-7151(95)00012-K.

[19] K. Kuroda, M. Takahashi, T. Kato, H. Saka, S. Tsuji, Application of focused ion beam milling to cross-sectional TEM specimen preparation of industrial materials including heterointerfaces, Thin Solid Films. 319 (1998) 92–96. doi:10.1016/S0040-6090(97)01093-6.

[20] T. Kato, M.H. Hong, K. Nunome, K. Sasaki, K. Kuroda, H. Saka, Cross-sectional TEM observation of multilayer structure of a galvannealed steel, Thin Solid Films. 319 (1998) 132–139. doi:10.1016/S0040-6090(97)01108-5.

[21] L.A. Giannuzzi, J.L. Drown, S.R. Brown, R.B. Irwin, F.A. Stevie, Applications of the FIB lift-out technique for TEM specimen preparation, Microscopy Research and Technique. 41 (n.d.) 285–290. doi:10.1002/(SICI)1097-0029(19980515)41:4<285::AID-JEMT1>3.0.CO;2-Q.

[22] M.S. Kim, J.H. Kwak, J.S. Kim, Y.H. Liu, N. Gao, N.-Y. Tang, Galvanizability of Advanced High-Strength Steels 1180TRIP and 1180CP, Metall and Mat Trans A. 40 (2009) 1903–1910. doi:10.1007/s11661-009-9880-7.

[23] E.M. Bellhouse, J.R. McDermid, Analysis of the Fe–Zn interface of galvanized high Al–low Si TRIP steels, Materials Science and Engineering: A. 491 (2008) 39–46. doi:10.1016/j.msea.2007.12.033.

[24] R. Kavitha, J.R. McDermid, On the in-situ aluminothermic reduction of manganese oxides in continuous galvanizing baths, Surface and Coatings Technology. 212 (2012) 152–158. doi:10.1016/j.surfcoat.2012.09.038.

[25] K.-K. Wang, C.-W. Hsu, L. Chang, D. Gan, T.-R. Chen, K.-C. Yang, Study of Selective Oxidation Behavior of a 1.2Si-1.5Mn TRIP Steel during Intercritical Annealing, J. Electrochem. Soc. 159 (2012) C561–C570. doi:10.1149/2.050212jes.

[26] L. Cho, S.J. Lee, M.S. Kim, Y.H. Kim, B.C.D. Cooman, Influence of Gas Atmosphere Dew Point on the Selective Oxidation and the Reactive Wetting During Hot Dip Galvanizing of CMnSi TRIP Steel, Metall and Mat Trans A. 44 (2013) 362–371. doi:10.1007/s11661-012-1392-1.

[27] Y.F. Gong, H.S. Kim, B.C.D. Cooman, Formation of Surface and Subsurface Oxides during Ferritic, Intercritical and Austenitic Annealing of CMnSi TRIP Steel, ISIJ Int. 48 (2008) 1745–1751. doi:10.2355/isijinternational.48.1745.

[28] Y.F. Gong, H.S. Kim, B.C.D. Cooman, Internal Oxidation during Intercritical Annealing of CMnSi TRIP Steel, ISIJ Int. 49 (2009) 557–563. doi:10.2355/isijinternational.49.557.

[29] I. Hertveldt, B.C.D. Cooman, S. Claessens, Influence of annealing conditions on the galvanizability and galvannealing properties of TiNb interstitial-free steels, strengthened with phosphorous and manganese, Metall and Mat Trans A. 31 (2000) 1225–1232. doi:10.1007/s11661-000-0118-y.

[30] G.M. Song, W.G. Sloof, T. Vystavl, H. De, Interface microstructure and adhesion of zinc coatings on TRIP steels, Materials Science Forum. 539–543 (2007) 1104–1109.

[31] S. Frenznick, S. Swaminathan, M. Stratmann, M. Rohwerder, A novel approach to determine high temperature wettability and interfacial reactions in liquid metal/solid interface, J Mater Sci. 45 (2010) 2106–2111. doi:10.1007/s10853-009-4147-7.

[32] R. Sagl, A. Jarosik, D. Stifter, G. Angeli, The role of surface oxides on annealed high-strength steels in hot-dip galvanizing, Corrosion Science. 70 (2013) 268–275. doi:10.1016/j.corsci.2013.01.039.

[33] E.M. Bellhouse, A.I.M. Mertens, J.R. McDermid, Development of the surface structure of TRIP steels prior to hot-dip galvanizing, Materials Science and Engineering: A. 463 (2007) 147–156. doi:10.1016/j.msea.2006.09.117.

[34] Z.G. Hu, P. Zhu, J. Meng, Fatigue properties of transformation-induced plasticity and dual-phase steels for auto-body lightweight: Experiment, modeling and application, Materials & Design. 31 (2010) 2884–2890. doi:10.1016/j.matdes.2009.12.034.

[35] J.V. Slycken, P. Verleysen, J. Degrieck, L. Samek, B.C. de Cooman, High-strain-rate behavior of low-alloy multiphase aluminum- and silicon-based transformation-induced plasticity steels, Metall and Mat Trans A. 37 (2006) 1527–1539. doi:10.1007/s11661-006-0097-8.

[36] R.O. Rocha, T.M.F. Melo, E.V. Pereloma, D.B. Santos, Microstructural evolution at the initial stages of continuous annealing of cold rolled dual-phase steel, Materials Science and Engineering: A. 391 (2005) 296–304. doi:10.1016/j.msea.2004.08.081.

[37] M. Sarwar, R. Priestner, Influence of ferrite-martensite microstructural morphology on tensile properties of dual-phase steel, JOURNAL OF MATERIALS SCIENCE. 31 (1996) 2091–2095. doi:10.1007/BF00356631.

[38] D. Bhattacharya, Developments in advanced high strength steels, in: The Joint International Conference of HSLA Steels, 2005: pp. 70–73.

[39] J. Coryell, J. Campbell, V. Savic, J. Bradley, S. Mishra, S. Tiwari, L.H. Jr, Tensile Deformation of Quenched and Partitioned Steel – A Third Generation High Strength Steel, in: Supplemental Proceedings, Wiley-Blackwell, 2012: pp. 555–562. doi:10.1002/9781118357002.ch70.

[40] S. Pisarik, D.V. Aken, K. Limmer, J. Medvedeva, Developing a Third-Generation Advanced High-Strength Steel with Two-Stage Trip Behavior, AISTech - Iron and Steel Technology Conference Proceedings. (2014) 3013–3023.

[41] G. Zheng, X. Li, Y. Chang, C. Wang, H. Dong, A Comparative Study on Formability of the Third-Generation Automotive Medium-Mn Steel and 22MnB5 Steel, J. of Materi Eng and Perform. 27 (2018) 530–540. doi:10.1007/s11665-018-3183-3.

[42] Y. Chang, S. Han, X. Li, C. Wang, G. Zheng, H. Dong, Effect of shearing clearance on formability of sheared edge of the third-generation automotive medium-Mn steel with metastable austenite, Journal of Materials Processing Technology. 259 (2018) 216–227. doi:10.1016/j.jmatprotec.2018.04.038.

[43] D.K. Matlock, J.G. Speer, Processing Opportunities for New Advanced High-Strength Sheet Steels, Materials and Manufacturing Processes. 25 (2010) 7–13. doi:10.1080/10426910903158272.

[44] L. Wang, J.G. Speer, Quenching and Partitioning Steel Heat Treatment, Metallogr. Microstruct. Anal. 2 (2013) 268–281. doi:10.1007/s13632-013-0082-8.

[45] M.F. Horstemeyer, Integrated computational materials engineering (ICME) for metals: using multiscale modeling to invigorate engineering design with science, WILEY [u.a.], Hoboken, NJ, 2012.

[46] V. Savic, L. Hector, H. Singh, M. Paramasuwom, U. Basu, A. Basudhar, N. Stander, Integrated Computational Materials Engineering Approach to Development of a Lightweight Third Generation Advanced High-Strength Steel (3GAHSS) Vehicle Body Structure, in: 2018. doi:10.4271/2018-01-1026.

[47] M.S. Daw, M.I. Baskes, Semiempirical, Quantum Mechanical Calculation of Hydrogen Embrittlement in Metals, Phys. Rev. Lett. 50 (1983) 1285–1288. doi:10.1103/PhysRevLett.50.1285.

[48] M.S. Daw, M.I. Baskes, Embedded-atom method: Derivation and application to impurities, surfaces, and other defects in metals, Phys. Rev. B. 29 (1984) 6443–6453. doi:10.1103/PhysRevB.29.6443.

[49] M.I. Baskes, Application of the Embedded-Atom Method to Covalent Materials: A Semiempirical Potential for Silicon, Phys. Rev. Lett. 59 (1987) 2666–2669. doi:10.1103/PhysRevLett.59.2666.

[50] M.S. Daw, Model of metallic cohesion: The embedded-atom method, Phys. Rev. B. 39 (1989) 7441–7452. doi:10.1103/PhysRevB.39.7441.

[51] M.I. Baskes, Modified embedded-atom potentials for cubic materials and impurities, Physical Review B. 46 (1992) 2727–2742. doi:10.1103/PhysRevB.46.2727.

[52] M.I. Baskes, J.E. Angelo, C.L. Bisson, Atomistic calculations of composite interfaces, Modelling Simul. Mater. Sci. Eng. 2 (1994) 505. doi:10.1088/0965-0393/2/3A/006.

[53] K. Gall, M.F. Horstemeyer, M. Van Schilfgaarde, M.I. Baskes, Atomistic simulations on the tensile debonding of an aluminum–silicon interface, Journal of the Mechanics and Physics of Solids. 48 (2000) 2183–2212. doi:10.1016/S0022-5096(99)00086-1.

[54] B.-J. Lee, M.I. Baskes, Second nearest-neighbor modified embedded-atom-method potential, Physical Review B. 62 (2000) 8564–8567. doi:10.1103/PhysRevB.62.8564.

[55] B.-J. Lee, M.I. Baskes, H. Kim, Y. Koo Cho, Second nearest-neighbor modified embedded atom method potentials for bcc transition metals, Phys. Rev. B. 64 (2001) 184102. doi:10.1103/PhysRevB.64.184102.

[56] E. Asadi, M. Asle Zaeem, S. Nouranian, M.I. Baskes, Quantitative modeling of the equilibration of two-phase solid-liquid Fe by atomistic simulations on diffusive time scales, Phys. Rev. B. 91 (2015) 024105. doi:10.1103/PhysRevB.91.024105.

[57] E. Asadi, M.A. Zaeem, M.I. Baskes, Phase-Field Crystal Model for Fe Connected to MEAM Molecular Dynamics Simulations, JOM. 66 (2014) 429–436. doi:10.1007/s11837-013-0845-3.

[58] B.-J. Lee, J.-H. Shim, M.I. Baskes, Semiempirical atomic potentials for the fcc metals Cu, Ag, Au, Ni, Pd, Pt, Al, and Pb based on first and second nearest-neighbor modified embedded atom method, Phys. Rev. B. 68 (2003) 144112. doi:10.1103/PhysRevB.68.144112.

[59] E. Asadi, M. Asle Zaeem, S. Nouranian, M.I. Baskes, Two-phase solid–liquid coexistence of Ni, Cu, and Al by molecular dynamics simulations using the modified embedded-atom method, Acta Materialia. 86 (2015) 169–181. doi:10.1016/j.actamat.2014.12.010.

[60] Y.-M. Kim, B.-J. Lee, M.I. Baskes, Modified embedded-atom method interatomic potentials for Ti and Zr, Phys. Rev. B. 74 (2006) 014101. doi:10.1103/PhysRevB.74.014101.

[61] Y.-M. Kim, N.J. Kim, B.-J. Lee, Atomistic Modeling of pure Mg and Mg–Al systems, Calphad. 33 (2009) 650–657. doi:10.1016/j.calphad.2009.07.004.

[62] D.E. Dickel, M.I. Baskes, I. Aslam, C.D. Barrett, New interatomic potential for Mg–Al–Zn alloys with specific application to dilute Mg-based alloys, Modelling and Simulation in Materials Science and Engineering. 26 (2018) 045010. doi:10.1088/1361-651X/aabaad.

[63] H.-S. Jang, K.-M. Kim, B.-J. Lee, Modified embedded-atom method interatomic potentials for pure Zn and Mg-Zn binary system, Calphad. 60 (2018) 200–207. doi:10.1016/j.calphad.2018.01.003.

[64] E. Asadi, M. Asle Zaeem, The anisotropy of hexagonal close-packed and liquid interface free energy using molecular dynamics simulations based on modified embedded-atom method, Acta Materialia. 107 (2016) 337–344. doi:10.1016/j.actamat.2016.01.043.

[65] Y.-M. Kim, Y.-H. Shin, B.-J. Lee, Modified embedded-atom method interatomic potentials for pure Mn and the Fe–Mn system, Acta Materialia. 57 (2009) 474–482. doi:10.1016/j.actamat.2008.09.031.

[66] B.-J. Lee, J.W. Lee, A modified embedded atom method interatomic potential for carbon, Calphad. 29 (2005) 7–16. doi:10.1016/j.calphad.2005.02.003.

[67] B.-J. Lee, A modified embedded atom method interatomic potential for silicon, Calphad. 31 (2007) 95–104. doi:10.1016/j.calphad.2006.10.002.

[68] E.H. Kim, Y.-H. Shin, B.-J. Lee, A modified embedded-atom method interatomic potential for Germanium, Calphad. 32 (2008) 34–42. doi:10.1016/j.calphad.2007.12.003.

[69] B.-J. Lee, J.-W. Jang, A modified embedded-atom method interatomic potential for the Fe–H system, Acta Materialia. 55 (2007) 6779–6788. doi:10.1016/j.actamat.2007.08.041.

[70] B.-J. Lee, T.-H. Lee, S.-J. Kim, A modified embedded-atom method interatomic potential for the Fe–N system: A comparative study with the Fe–C system, Acta Materialia. 54 (2006) 4597–4607. doi:10.1016/j.actamat.2006.06.003.

[71] T.S. Gates, G.M. Odegard, S.J.V. Frankland, T.C. Clancy, Computational materials: Multi-scale modeling and simulation of nanostructured materials, Composites Science and Technology. 65 (2005) 2416–2434. doi:10.1016/j.compscitech.2005.06.009.

[72] B.-J. Lee, A modified embedded-atom method interatomic potential for the Fe–C system, Acta Materialia. 54 (2006) 701–711. doi:10.1016/j.actamat.2005.09.034.

[73] C. Wu, B.-J. Lee, X. Su, Modified embedded-atom interatomic potential for Fe-Ni, Cr-Ni and Fe-Cr-Ni systems, Calphad. 57 (2017) 98–106. doi:10.1016/j.calphad.2017.03.007.

[74] P. Liu, X. Han, D. Sun, Q. Wang, Development and application of a ternary Ti-Al-N interatomic potential for Ti2AlN/TiAl composite, Journal of Alloys and Compounds. 745 (2018) 63–74. doi:10.1016/j.jallcom.2018.02.168.

[75] H.-K. Kim, W.-S. Jung, B.-J. Lee, Modified embedded-atom method interatomic potentials for the Fe–Ti–C and Fe–Ti–N ternary systems, Acta Materialia. 57 (2009) 3140–3147. doi:10.1016/j.actamat.2009.03.019.

[76] C.-L. Kuo, P. Clancy, Development of atomistic MEAM potentials for the silicon–oxygen–gold ternary system, Modelling Simul. Mater. Sci. Eng. 13 (2005) 1309. doi:10.1088/0965-0393/13/8/008.

[77] C.A. Becker, F. Tavazza, Z.T. Trautt, R.A. Buarque de Macedo, Considerations for choosing and using force fields and interatomic potentials in materials science and engineering, Current Opinion in Solid State and Materials Science. 17 (2013) 277–283. doi:10.1016/j.cossms.2013.10.001.

[78] B. Jelinek, S. Groh, M.F. Horstemeyer, J. Houze, S.G. Kim, G.J. Wagner, A. Moitra, M.I. Baskes, Modified embedded atom method potential for Al, Si, Mg, Cu, and Fe alloys, Physical Review B. 85 (2012). doi:10.1103/PhysRevB.85.245102.

[79] M.F. Horstemeyer, Integrated Computational Materials Engineering (ICME) for Metals: Using Multiscale Modeling to Invigorate Engineering Design with Science, Wiley.Com. (n.d.).

[80] J.P. Perdew, K. Burke, M. Ernzerhof, Generalized Gradient Approximation Made Simple, Physical Review Letters. 77 (1996) 3865–3868. doi:10.1103/PhysRevLett.77.3865.

[81] H.J. Monkhorst, J.D. Pack, Special points for Brillouin-zone integrations, (n.d.) 5.

[82] C.D. Barrett, R.L. Carino, The MEAM parameter calibration tool: an explicit methodology for hierarchical bridging between ab initio and atomistic scales, Integr Mater Manuf Innov. 5 (2016) 9. doi:10.1186/s40192-016-0051-6.

[83] R.L. Carino, M.F. Horstemeyer, Case Studies in Using MATLAB to Build Model Calibration Tools for Multiscale Modeling, in: J. Valdman (Ed.), Applications from Engineering with MATLAB Concepts, InTech, 2016. doi:10.5772/62348.

[84] C. Kittel, Introduction to Solid State Physics, 8th Edition, John Wiley & Sons, 2004.

[85] C.S. Barrett, T.B. Massalski, Structure of metals: crystallographic methods, principles and data, 3rd rev. ed, Pergamon, Oxford ; New York, 1980.

[86] S. Fahy, S.G. Louie, High-pressure structural and electronic properties of carbon, Phys. Rev. B. 36 (1987) 3373–3385. doi:10.1103/PhysRevB.36.3373.

[87] L. Brewer, Cohesive energies of the elements, California Univ., Berkeley (USA). Lawrence Berkeley Lab., 1975. doi:10.2172/7187973.

[88] H.-E. Schaefer, K. Maier, M. Weller, D. Herlach, A. Seeger, J. Diehl, Vacancy formation in iron investigated by positron annihilation in thermal equilibrium, Scripta Metallurgica. 11 (1977) 803–809. doi:10.1016/0036-9748(77)90079-5.

[89] S. Dannefaer, P. Mascher, D. Kerr, Monovacancy Formation Enthalpy in Silicon, Physical Review Letters. 56 (1986) 2195–2198. doi:10.1103/PhysRevLett.56.2195.

[90] M. Timonova, B.-J. Lee, B.J. Thijsse, Sputter erosion of Si(001) using a new silicon MEAM potential and different thermostats, Nuclear Instruments and Methods in Physics Research Section B: Beam Interactions with Materials and Atoms. 255 (2007) 195–201. doi:10.1016/j.nimb.2006.11.023.

[91] S. Ryu, C.R. Weinberger, M.I. Baskes, W. Cai, Improved modified embedded-atom method potentials for gold and silicon, Modelling and Simulation in Materials Science and Engineering. 17 (2009) 075008. doi:10.1088/0965-0393/17/7/075008.

[92] P. Torelli, F. Sirotti, P. Ballone, Surface alloying and mixing at the Mn/Fe(001) interface: Real-time photoelectron spectroscopy and modified embedded atom simulations, Physical Review B. 68 (2003). doi:10.1103/PhysRevB.68.205413.

[93] F.R. de Boer, Cohesion in metals: transition metal alloys, North-Holland ; Sole distributors for the U.S.A. and Canada, Elsevier Scientific Pub. Co., Amsterdam ; New York : New York, N.Y., U.S.A., 1988. https://catalog.hathitrust.org/Record/001551517 (accessed May 16, 2018).

[94] M. Rosen, Elastic Moduli and Ultrasonic Attenuation of Polycrystalline α-Mn from 4.2-300°K, Phys. Rev. 165 (1968) 357–359. doi:10.1103/PhysRev.165.357.

[95] K. Takemura, O. Shimomura, K. Hase, T. Kikegawa, The high-pressure equation of state of α-Mn to 42 GPa, J. Phys. F: Met. Phys. 18 (1988) 197. doi:10.1088/0305-4608/18/2/004.

[96] N. Mōri, M. Takahashi, G. Oomi, Magnetic contribution to the bulk modulus of 3d-transition metal alloys, Journal of Magnetism and Magnetic Materials. 31–34 (1983) 135–136. doi:10.1016/0304-8853(83)90187-7.

[97] H. Fujihisa, K. Takemura, Stability and the equation of state of alpha-manganese under ultrahigh pressure, Phys. Rev. B. 52 (1995) 13257–13260. doi:10.1103/PhysRevB.52.13257.

[98] A. Dargys, J. Kundrotas, Handbook on physical properties of Ge, Si, GaAs and InP, Science and Encyclopedia Publ, Vilnius, 1994.

[99] M.H. Grimsditch, A.K. Ramdas, Brillouin scattering in diamond, Phys. Rev. B. 11 (1975) 3139–3148. doi:10.1103/PhysRevB.11.3139.

[100] S. Mun, A.L. Bowman, S. Nouranian, S.R. Gwaltney, M.I. Baskes, M.F. Horstemeyer, Interatomic Potential for Hydrocarbons on the Basis of the Modified Embedded-Atom Method with Bond Order (MEAM-BO), J. Phys. Chem. A. 121 (2017) 1502–1524. doi:10.1021/acs.jpca.6b11343.

[101] E.G. Moroni, W. Wolf, J. Hafner, R. Podloucky, Cohesive, structural, and electronic properties of Fe-Si compounds, Phys. Rev. B. 59 (1999) 12860–12871. doi:10.1103/PhysRevB.59.12860.

[102] S.V. Meschel, O.J. Kleppa, Standard enthalpies of formation of some 3d transition metal carbides by high temperature reaction calorimetry, Journal of Alloys and Compounds. 257 (1997) 227–233. doi:10.1016/S0925-8388(97)00023-6.

[103] D. Djurovic, B. Hallstedt, J. von Appen, R. Dronskowski, Thermodynamic assessment of the Mn–C system, Calphad. 34 (2010) 279–285. doi:10.1016/j.calphad.2010.05.002.

[104] P. Paufler, P. Villars, L. D. Calvert. Pearson's handbook of crystallographic data for intermetallic phases. American Society for Metals. Metals Park. Ohio. 1986. Vols. 1–3. 3258 pp, US $ 495.00 ISBN 0-87170-217-7, Crystal Research and Technology. 22 (n.d.) 1436–1436. doi:10.1002/crat.2170221117.

[105] I.G. Wood, L. Vočadlo, K.S. Knight, D.P. Dobson, W.G. Marshall, G.D. Price, J. Brodholt, Thermal expansion and crystal structure of cementite, Fe_3C, between 4 and 600 K determined by time-of-flight neutron powder diffraction, Journal of Applied Crystallography. 37 (2004) 82–90. doi:10.1107/S0021889803024695.

[106] J. Bouchaud, Etude structurale des carbures de manganese, in: Annales de Chimie, 1967: pp. 353–366.

[107] P. Karen, H. Fjellvåg, A. Kjekshus, A.F. Andresen, On the phase relations and structural and magnetic properties of the stable manganese carbides Mn23C6, Mn5C2 and Mn7C3, Acta Chemica Scandinavica. 45 (1991) 549–557.

[108] G.P. Zinoveva, L.P. Andreeva, P.V. Geld, Elastic constants and dynamics of crystal lattice in monosilicides with B20 structure, Physica Status Solidi (A). 23 (n.d.) 711–718. doi:10.1002/pssa.2210230244.

[109] R. Caracas, R. Wentzcovitch, Equation of state and elasticity of FeSi, Geophysical Research Letters. 31 (n.d.). doi:10.1029/2004GL020601.

[110] G. Randltt, Lattice dynamics and related diffusion properties of intermetallics: I. Fe3Si, (n.d.) 18.

[111] C. Jiang, S.G. Srinivasan, A. Caro, S.A. Maloy, Structural, elastic, and electronic properties of Fe3C from first principles, Journal of Applied Physics. 103 (2008) 043502. doi:10.1063/1.2884529.

[112] X. Chong, Y. Jiang, R. Zhou, J. Feng, First principles study the stability, mechanical and electronic properties of manganese carbides, Computational Materials Science. 87 (2014) 19–25. doi:10.1016/j.commatsci.2014.01.054.

[113] Dwight E. Gray (Ed.), American Institute of Physics Handbook, McGraw-Hill Book Company Inc., 1957.

[114] ASM International, J.R. Davis, ASM International, eds., Properties and selection: irons, steels and high-performance alloys, [10. ed.], 6. print, ASM International, Materials Park, Ohio, 2001.

[115] V.T. Witusiewicz, F. Sommer, E.J. Mittemeijer, Enthalpy of formation and heat capacity of Fe-Mn alloys, Metall and Materi Trans B. 34 (2003) 209–223. doi:10.1007/s11663-003-0008-y.

[116] J.M. Haile, Molecular Dynamics Simulation: Elementary Methods, 1st ed., John Wiley & Sons, Inc., New York, NY, USA, 1992.

[117] J.J. Burton, Vacancy-Formation Entropy in Cubic Metals, Phys. Rev. B. 5 (1972) 2948–2957. doi:10.1103/PhysRevB.5.2948.

[118] B. Zhang, Calculation of self-diffusion coefficients in iron, AIP Advances. 4 (2014) 017128. doi:10.1063/1.4863462.

[119] J. Mackowiak, N.R. Short, Metallurgy of galvanized coatings, International Metals Reviews. 24 (1979) 1–19. doi:10.1179/imtr.1979.24.1.1.

[120] M. Guttmann, Y. Lepretre, A. Aubry, M.-J. Roch, T. Moreau, P. Drillet, J.M. Mataigne, H. Baudin, Mechanisms of the galvanizing reaction. Influence of titanium and phosphorus contents in steel and of its surface microstructure after annealing, Galvatech'95. The Use and Manufacture of Zinc and Zinc Alloy Coated Sheet Steel Products Into the 21 St Century. (1995) 295–307.

[121] P.J. Brown, The structure of the δ-phase in the transition metal–zinc alloy systems, Acta Crystallographica. 15 (1962) 608–612. doi:10.1107/S0365110X62001528.

[122] H. Baker, A.S.M. Handbook, Vol. 3: Phase Diagrams, ASM International, New York. (1992) 2–317.

[123] C.E. Jordan, A.R. Marder, Fe-Zn phase formation in interstitial-free steels hot-dip galvanized at 450°C: Part II 0.20 wt% Al-Zn baths, Journal of Materials Science. 32 (1997) 5603–5610. doi:10.1023/A:1018632709739.

[124] H. Gao, A. Otero-de-la-Roza, S.M. Aouadi, E.R. Johnson, A. Martini, An empirical model for silver tantalate, Modelling Simul. Mater. Sci. Eng. 21 (2013) 055002. doi:10.1088/0965-0393/21/5/055002.

[125] W.B. Pearson, A Handbook of Lattice Spacings and Structures of Metals and Alloys, Elsevier, 1958. doi:10.1016/C2013-0-08243-6.

[126] R.O. Simmons, R.W. Balluffi, Measurements of Equilibrium Vacancy Concentrations in Aluminum, Phys. Rev. 117 (1960) 52–61. doi:10.1103/PhysRev.117.52.

[127] G.N. Kamm, H.V. Bohm, Magnetoacoustic Measurements of the Fermi Surface of Aluminum, Phys. Rev. 131 (1963) 111–120. doi:10.1103/PhysRev.131.111.

[128] T. Hehenkamp, Absolute vacancy concentrations in noble metals and some of their alloys, Journal of Physics and Chemistry of Solids. 55 (1994) 907–915. doi:10.1016/0022-3697(94)90110-4.

[129] M.I. Pascuet, J.R. Fernández, Atomic interaction of the MEAM type for the study of intermetallics in the Al–U alloy, Journal of Nuclear Materials. 467 (2015) 229–239. doi:10.1016/j.jnucmat.2015.09.030.

[130] M.I. Baskes, Commentary on 'modified embedded atom method potentials for hcp metals' M I Baskes and R A Johnson (1994) *Modelling Simul. Mater. Sci. Eng.* —the early basis for modeling hcp materials using MEAM, Modelling and Simulation in Materials Science and Engineering. 25 (2017) 071002. doi:10.1088/1361-651X/aa817e.

[131] E. Kaxiras, Atomic and Electronic Structure of Solids, Cambridge University Press, Cambridge, 2003. doi:10.1017/CBO9780511755545.

[132] W.B. Pearson, Handbook of Lattice Spacings and Structures of Metals and Alloys, Vol. 2, Oxford, Pergamon, 1967.

[133] C.W. Garland, R. Dalven, Elastic Constants of Zinc from 4.2°K to 77.6°K, Phys. Rev. 111 (1958) 1232–1234. doi:10.1103/PhysRev.111.1232.

[134] H.M. Gilder, G.N. Wallmark, Thermal-Expansion Measurements of Vacancy Formation Parameters in Zinc Single Crystals, Phys. Rev. 182 (1969) 771–777. doi:10.1103/PhysRev.182.771.

[135] A.H. Maitland, G.A. Chadwick, The cleavage surface energy of zinc, The Philosophical Magazine: A Journal of Theoretical Experimental and Applied Physics. 19 (1969) 645–651. doi:10.1080/14786436908216323.

[136] P.D. Desai, Thermodynamic Properties of Selected Binary Aluminum Alloy Systems, Journal of Physical and Chemical Reference Data. 16 (1987) 109–124. doi:10.1063/1.555788.

[137] M. Mihalkovič, M. Widom, Structure and stability of Al_2Fe and Al_5Fe_2: First-principles total energy and phonon calculations, Phys. Rev. B. 85 (2012) 014113. doi:10.1103/PhysRevB.85.014113.

[138] M. Mihalkovic, M. Widom, Alloy Database, (n.d.). http://alloy.phys.cmu.edu/published/AlFe/ (accessed July 16, 2018).

[139] ALLOY INDEX, (n.d.). http://alloy.phys.cmu.edu/cgi-bin/mkp.csh (accessed July 16, 2018).

[140] S.V. Meschel, O.J. Kleppa, Standard enthalpies of formation of AlB12 and Al4C3 by high temperature direct synthesis calorimetry, Journal of Alloys and Compounds. 227 (1995) 93–96. doi:10.1016/0925-8388(95)01649-X.

[141] CRC Handbook of Chemistry and Physics, 99th Edition, CRC Press. (2018). https://www.crcpress.com/CRC-Handbook-of-Chemistry-and-Physics-99th-Edition/Rumble/p/book/9781138561632 (accessed July 15, 2018).

[142] E. Lee, K.-R. Lee, M.I. Baskes, B.-J. Lee, A modified embedded-atom method interatomic potential for ionic systems: 2NNMEAM + Qeq, Phys. Rev. B. 93 (2016) 144110. doi:10.1103/PhysRevB.93.144110.

[143] T.J.B. Holland, R. Powell, An enlarged and updated internally consistent thermodynamic dataset with uncertainties and correlations: the system K2O–Na2O–CaO–MgO–MnO–FeO–Fe2O3–Al2O3–TiO2–SiO2–C–H2–O2, Journal of Metamorphic Geology. 8 (n.d.) 89–124. doi:10.1111/j.1525-1314.1990.tb00458.x.

[144] A. Kontio, P. Coppens, New study of the structure of MnAl6, Acta Crystallographica Section B. 37 (n.d.) 433–435. doi:10.1107/S0567740881003191.

[145] K. Schubert, M. Kluge, Notizen: Über den Bindungszustand bei Fe2 Al5 und MnAl6, Zeitschrift Für Naturforschung A. 8 (2014) 755–756. doi:10.1515/zna-1953-1113.

[146] T.M. Gesing, W. Jeitschko, The Crystal Structure and Chemical Properties of U2Al3C4 and Structure Refinement of Al4C3, Zeitschrift Für Naturforschung B. 50 (2014) 196–200. doi:10.1515/znb-1995-0206.

[147] M.D. Towler, N.L. Allan, N.M. Harrison, V.R. Saunders, W.C. Mackrodt, E. Aprà, Ab initio study of MnO and NiO, Phys. Rev. B. 50 (1994) 5041–5054. doi:10.1103/PhysRevB.50.5041.

[148] J. Pike, J. Hanson, L. Zhang, S.-W. Chan, Synthesis and Redox Behavior of Nanocrystalline Hausmannite (Mn3O4), Chem. Mater. 19 (2007) 5609–5616. doi:10.1021/cm071704b.

[149] L. Levien, C.T. Prewitt, D.J. Weidner, Structure and elastic properties of quartz at pressure, American Mineralogist. 65 (1980) 920–930.

[150] A.F. Wright, M.S. Lehmann, The structure of quartz at 25 and 590°C determined by neutron diffraction, Journal of Solid State Chemistry. 36 (1981) 371–380. doi:10.1016/0022-4596(81)90449-7.

[151] M.H. Yoo, T. Takasugi, S. Hanada, O. Izumi, Slip Modes in B2-Type Intermetallic Alloys, Materials Transactions, JIM. 31 (1990) 435–442.

[152] T.M. Press, Single Crystal Elastic Constants and Calculated Aggregate Properties, Second Edition, The MIT Press. (n.d.). https://mitpress.mit.edu/books/single-crystal-elastic-constants-and-calculated-aggregate-properties-second-edition (accessed July 15, 2018).

[153] T. Liao, J. Wang, Y. Zhou, Atomistic deformation modes and intrinsic brittleness of Al_4SiC_4: A first-principles investigation, Phys. Rev. B. 74 (2006) 174112. doi:10.1103/PhysRevB.74.174112.

[154] Y. Sumino, M. Kumazawa, O. Nishizawa, W. Pluschkell, THE ELASTIC CONSTANTS OF SINGLE CRYSTAL Fe1-xO, MnO AND CoO, AND THE ELASTICITY OF STOICHIOMETRIC MAGNESIOWÜSTITE, J,Phys,Earth. 28 (1980) 475–495. doi:10.4294/jpe1952.28.475.

[155] H. Lv, M. Yao, Q. Li, Z. Li, B. Liu, R. Liu, S. Lu, D. Li, J. Mao, X. Ji, J. Liu, Z. Chen, B. Zou, T. Cui, B. Liu, Effect of Grain Size on Pressure-Induced Structural Transition in Mn3O4, J. Phys. Chem. C. 116 (2012) 2165–2171. doi:10.1021/jp2067028.

[156] A. Stukowski, Visualization and analysis of atomistic simulation data with OVITO–the Open Visualization Tool, Modelling Simul. Mater. Sci. Eng. 18 (2010) 015012. doi:10.1088/0965-0393/18/1/015012.

[157] J.M. Hughes, M.F. Horstemeyer, R. Carino, N. Sukhija, W.B. Lawrimore, S. Kim, M.I. Baskes, Hierarchical Bridging Between Ab Initio and Atomistic Level Computations: Sensitivity and Uncertainty Analysis for the Modified Embedded-Atom Method (MEAM) Potential (Part B), JOM. 67 (2015) 148–153. doi:10.1007/s11837-014-1205-7.

[158] M.A. Tschopp, B. Chris Rinderspacher, S. Nouranian, M.I. Baskes, S.R. Gwaltney, M.F. Horstemeyer, Quantifying Parameter Sensitivity and Uncertainty for Interatomic Potential Design: Application to Saturated Hydrocarbons, ASME J. Risk Uncertainty Part B. 4 (2017) 011004-011004–17. doi:10.1115/1.4037455.

APPENDIX A

PLOTS FOR HEAT OF FORMATION OF BINARY COMPOUNDS

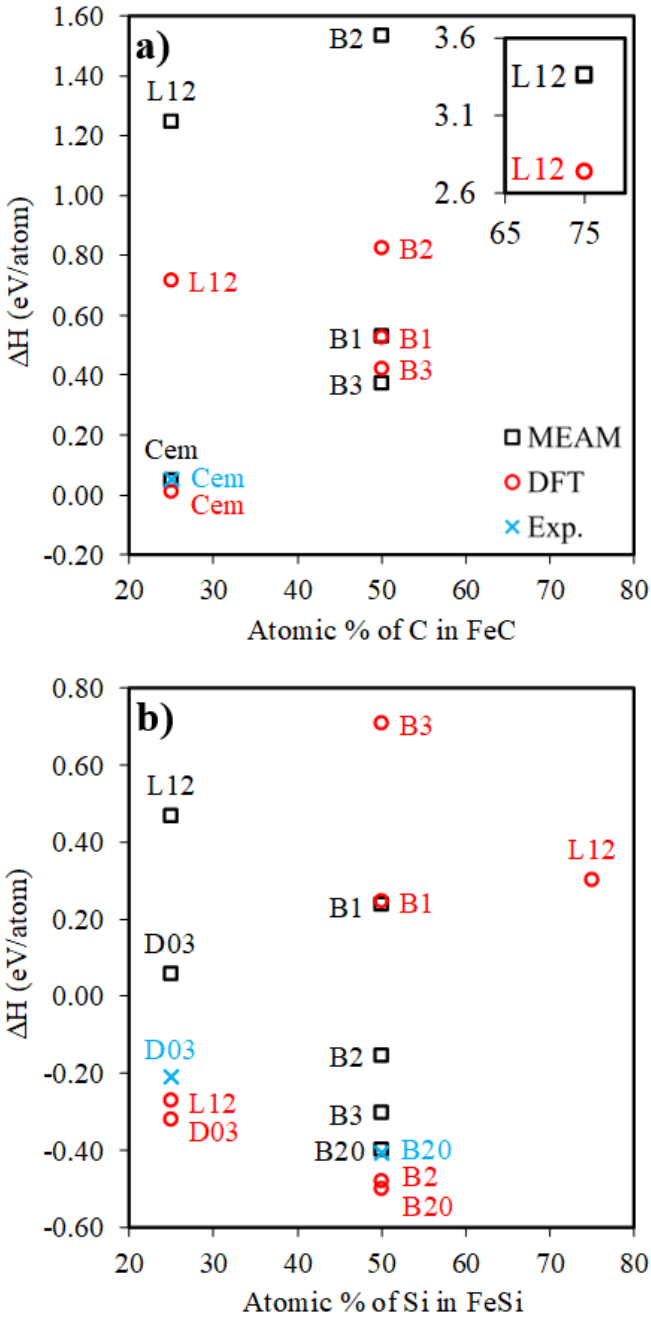

Figure A.1 Heat of formation for the binary compounds of a) Fe–C and b) Fe–Si plotted as a function of atomic percentage of an alloying element. The experimental structure for Fe–C is cementite.

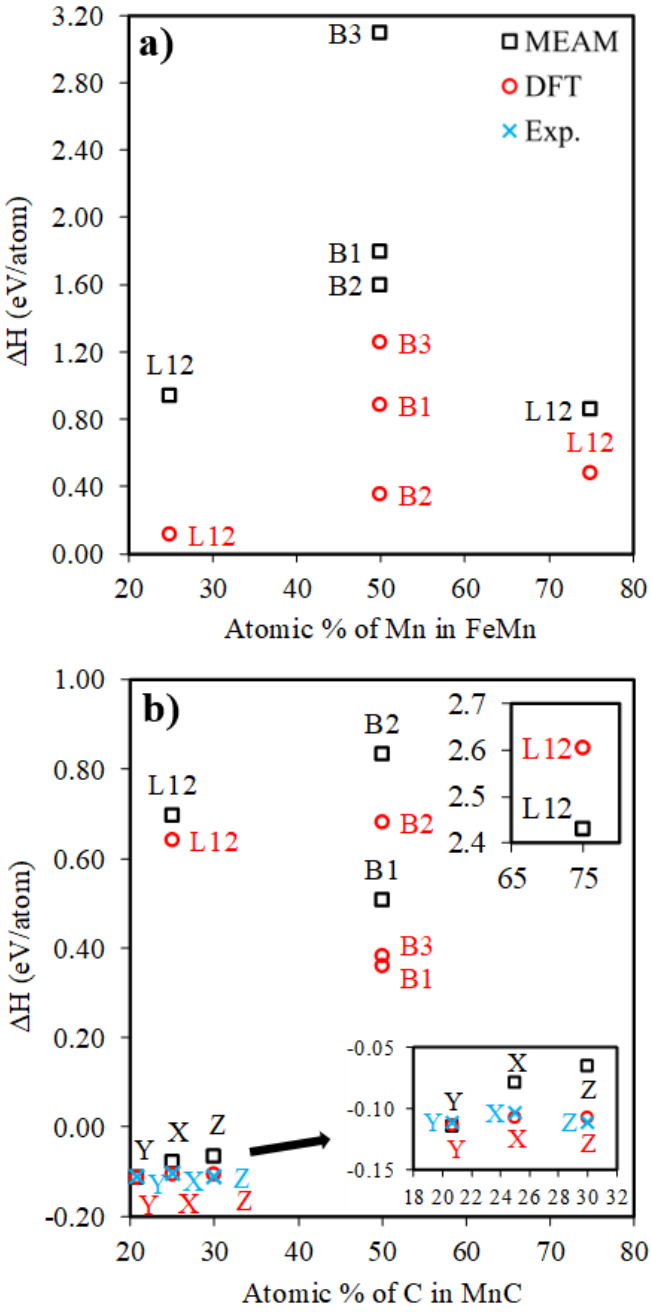

Figure A.2 Heat of formation for the binary compounds of a) Fe–Mn and b) Mn–C plotted as a function of atomic percentage of an alloying element. Compounds X, Y, and Z denote $Mn_{12}C_4$, $Mn_{23}C_6$, and Mn_7C_3, respectively.

APPENDIX B

MEAM FORMULATION

B.1 MEAM theory

The total energy E of a system of atoms in MEAM is approximated as the sum of the atomic energies

$$E = \sum_i E_i \tag{B.1}$$

The energy of atom I consists of the embedding energy and the pair potential terms:

$$E_i = F_i(\bar{\rho}_i) + \frac{1}{2}\sum_{j \neq i} \phi_{ij}(r_{ij}) \tag{B.2}$$

F is the embedding function, $\bar{\rho}_i$ is the background electron density at the site of the atom i, and $\phi_{ij}(r_{ij})$ is the pair potential between atoms i and j separated by a distance r_{ij}. The embedding energy $F_i(\bar{\rho}_i)$ represents the energy cost to insert atom i at a site where the background electron density is $\bar{\rho}_i$. The embedding energy is given in the form

$$F_i(\bar{\rho}_i) = \begin{cases} A_i E_i^0 \bar{\rho}_i \ln(\bar{\rho}_i) & \text{if } \bar{\rho}_i \geq 0 \\ -A_i E_i^0 \bar{\rho}_i & \text{if } \bar{\rho}_i < 0 \end{cases} \tag{B.3}$$

where the sublimation energy E_i^0 and parameter A_i depend on the element type of atom i. The background electron density E_i^0 is given by

$$\bar{\rho}_i = \frac{\rho_i^{(0)}}{\rho_i^0} G(\Gamma_i) \tag{B.4}$$

where

$$\Gamma_i = \sum_{k=1}^{3} \left(\frac{\rho_i^{(k)}}{\rho_i^{(0)}} \right)^2 \tag{B.5}$$

and

$$G(\Gamma) = \begin{cases} \sqrt{1+\Gamma} & \text{if } \Gamma \geq -1 \\ -\sqrt{|1+\Gamma|} & \text{if } \Gamma < -1 \end{cases} \tag{B.6}$$

The zeroth and higher order densities $\rho_i^{(0)}$, $\rho_i^{(1)}$, $\rho_i^{(2)}$, and $\rho_i^{(3)}$ are given in Equations B.9 – B.12 . The composition-dependent electron density scaling $\rho_i^{(0)}$ is given by

$$\rho_i^0 = \rho_{i0} Z_{i0} G(\Gamma_i^{\mathrm{ref}}) \tag{B.7}$$

where ρ_{i0} is an element-dependent density scaling, Z_{i0} is the first nearest-neighbor coordination of the reference system, and Γ_i^{ref} is given by

$$\Gamma_i^{\mathrm{ref}} = \frac{1}{Z_{i0}^2} \sum_{k=1}^{3} t_i^{(k)} s_i^{(k)} \tag{B.8}$$

where $s_i^{(k)}$ is the shape factor that depends on the refence structure of the atom *i*. Shape factors for various structures are specified in the work of Baskes [51]. The partial electron densities are given by

$$\rho_i^{(0)} = \sum_{j \neq i} \rho_j^{a(0)}(r_{ij}) S_{ij} \tag{B.9}$$

$$\left(\rho_i^{(1)}\right)^2 = \sum_{\alpha} \left[\sum_{j \neq i} \rho_j^{a(1)} \frac{r_{ij\alpha}}{r_{ij}} S_{ij}\right]^2 \tag{B.10}$$

$$\left(\rho_i^{(2)}\right)^2 = \sum_{\alpha,\beta} \left[\sum_{j \neq i} \rho_j^{a(2)} \frac{r_{ij\alpha} r_{ij\beta}}{r_{ij}^2} S_{ij}\right]^2 - \frac{1}{3}\left[\sum_{j \neq i} \rho_j^{a(2)}(r_{ij}) S_{ij}\right]^2 \tag{B.11}$$

$$\left(\rho_i^{(3)}\right)^2 = \sum_{\alpha,\beta,\gamma} \left[\sum_{j \neq i} \rho_j^{a(3)} \frac{r_{ij\alpha} r_{ij\beta} r_{ij\gamma}}{r_{ij}^3} S_{ij}\right]^2 - \frac{3}{5} \sum_{\alpha} \left[\sum_{j \neq i} \rho_j^{a(3)} \frac{r_{ij\alpha}}{r_{ij}} S_{ij}\right]^2 \tag{B.12}$$

where $r_{ij\alpha}$ is the α component of the displacement vector from atom *i* to atom *j*. S_{ij} is the screening function between atoms *i* and *j* and is defined in Equations B19 – B23. The atomic electron densities are computed as

$$\rho_i^{a(k)}(r_{ij}) = \rho_{i0} \exp\left[-\beta_i^{(k)}\left(\frac{r_{ij}}{r_i^0} - 1\right)\right] \tag{B.13}$$

where r_i^0 is the nearest neighbor distance in the single-element reference structure and $\beta_i^{(k)}$is an element-dependent parameter. Finally, the average weighting factors are given by

$$t_i^{(k)} = \frac{\sum_{j\neq i} t_{0,j}^{(k)} \rho_j^{a(0)} S_{ij}}{\sum_{j\neq i} \left(t_{0,j}^{(k)}\right)^2 \rho_j^{a(0)} S_{ij}} \tag{B.14}$$

where $t_{0,j}^{(k)}$ is an element-dependent parameter.

The pair potential is given by

$$\phi_{ij}(r_{ij}) = \bar{\phi}_{ij}(r_{ij}) S_{ij} \tag{B.15}$$

$$\phi_{ij}(r_{ij}) = \frac{1}{Z_{ij}}\left[2E_{ij}^u(r_{ij}) - F_i\left(\frac{Z_{ij}}{Z_i}\rho_i^{a(0)}(r_{ij})\right) - F_j\left(\frac{Z_{ij}}{Z_j}\rho_j^{a(0)}(r_{ij})\right)\right] \tag{B.16}$$

$$E_{ij}^u(r_{ij}) = -E_{ij}\left(1 + a_{ij}^*(r_{ij})\right)e^{-a_{ij}^*(r_{ij})} \tag{B.17}$$

$$a_{ij}^* = \alpha_{ij}\left(\frac{r_{ij}}{r_{ij}^0} - 1\right) \tag{B.18}$$

where E_{ij}, α_{ij}, and r_{ij}^0 are element-dependent parameters and Z_{ij} depends upon the structure of the reference system. The background densities $\hat{\rho}_i(r_{ij})$ in Equation B.16 are the densities for the reference structure computed with the interatomic spacing r_{ij}.

The screening function S_{ij} is designed so that $S_{ij} = 1$ if atoms *i* and *j* are unscreened and within the cutoff radius r_c and $S_{ij} = 0$ if they are completely screened or outside the cutoff radius. It varies smoothly between 0 and 1 for partial screening. The total screening function is the product of a radial cutoff function and three body terms involving all other atoms in the system:

$$S_{ij} = \bar{S}_{ij} f_c\left(\frac{r_c - r_{ij}}{\Delta r}\right) \tag{B.19}$$

$$\bar{S}_{ij} = \prod_{k \neq i,j} S_{ikj} \tag{B.20}$$

$$S_{ikj} = f_c\left(\frac{C_{ikj} - C_{min,ikj}}{C_{max,ikj} - C_{min,ikj}}\right) \tag{B.21}$$

$$C_{ikj} = 1 + 2\frac{r_{ij}^2 r_{ik}^2 + r_{ij}^2 r_{jk}^2 - r_{ij}^4}{r_{ij}^4 - \left(r_{ik}^2 - r_{jk}^2\right)^2} \tag{B.22}$$

$$f_c(x) = \begin{cases} 1 & x \geq 1 \\ [1 - (1-x)^4]^2 & 0 < x < 1 \\ 0 & x \leq 0 \end{cases} \tag{B.23}$$

Note that C_{min} and C_{max} can be defined separately for each $i - j - k$ triplet, based on their element types. The parameter Δr controls the distance over which the radial cutoff is smoothed from 1 to 0 near $r = r_c$.

B.2 Equilibrium lattice parameter and bulk modulus

MEAM postulates the Rose universal equation of state

$$E_R(a^*) = -E_c\left(1 + a^* + \delta\frac{\alpha a^{*3}}{\alpha + a^*}\right)e^{-a^*} \tag{B.24}$$

for the reference structure of each single element and for each element pair. The a^*, scaled distance from the equilibrium nearest neighbor position r_0, is

$$a^* = \alpha(r/r_0 - 1) \tag{B.25}$$

Two δ parameters may be specified for each element/pair: δ_r for negative, and δ_a for positive a^*. Then

$$\delta = \begin{cases} \delta_r & \text{for } a^* < 0 \\ \delta_a & \text{for } a^* \geq 0 \end{cases} \tag{B.26}$$

The MEAM potential parameter α is related to the equilibrium atomic volume Ω_0, the bulk modulus B_0, and the cohesive energy of the reference structure E_c as follows

$$\alpha = \sqrt{\frac{9B_0\Omega_0}{E_c}} \tag{B.27}$$